



Júlio Rafael Henriques Rocha **Dispositivos eletromecânicos avançados para uso em engenharia de tecidos: aplicações em tecidos duros**

Advanced electromechanical devices for use in tissue engineering: applications in hard tissues



Júlio Rafael Henriques Rocha **Advanced electromechanical devices for use in tissue engineering: applications in hard tissues**

Dissertação apresentada à Universidade de Aveiro para cumprimento dos requisitos necessários à obtenção do grau de Mestre em Materiais e Dispositivos Biomédicos, realizada sob a orientação científica da Prof. Doutora Paula Maria Lousada Silveirinha Vilarinho, Professora associada do Departamento de Engenharia de Materiais e Cerâmica da Universidade de Aveiro; Doutor Maxim Ivanov, Investigador do Departamento de Engenharia de Materiais e Cerâmica da Universidade de Aveiro e da Prof Doutora Ana Colette Maurício de Departamento de Clínicas Veterinárias do Instituto de Ciências Biomédicas Abel Salazar da Universidade do Porto.

o júri

Presidente

Prof. Doutor João André da Costa Tedim
professor auxiliar da Universidade de Aveiro

Arguente principal

Prof. Doutora Maria Ascensão Ferreira Silva Lopes
professora associada da Universidade do Porto

Orientadora

Prof. Doutora Paula Maria Lousada Silveirinha Vilarinho
professora associada da Universidade de Aveiro

Agradecimentos

Agradeço à Prof. Dra. Paula Vilarinho e ao Dr. Maxim Ivanov por todo o apoio, orientação e conhecimento científico que me transmitiram ao longo deste trabalho.

À Prof. Dra. Maria Helena por todas as sugestões e disponibilidade ceder equipamento laboratorial.

À Adriana por todo o conhecimento que me transmitiu e por todo o trabalho que desenvolveu previamente e sem o qual este trabalho não seria possível.

Aos meus colegas do Electroceramic Group por toda a disponibilidade e acolhimento no grupo, quero agradecer em especial à Camila, Manuel, Rui e Tomás.

A toda a equipa do DEMaC e Eng^a. Celeste, pelo apoio técnico prestado durante este trabalho.

Aos meus pais por todos os valores que me transmitiram e todas as oportunidades que me proporcionaram.

Ao meu irmão, Ricardo, pelos momentos de diversão e descontração.

Á minha namorada, Filipa, por me ter acompanhado durante toda esta etapa e pela motivação.

Ao meu amigo e colega, Hélder, por todo o apoio e espírito de entreatajuda durante todo o meu percurso académico.

palavras-chave

PLLA, Piezoelectricidade, Aço inoxidável, Biomateriais, Implante Ósseo, Cristalinidade

resumo

O aumento da esperança média de vida vem associado a uma maior incidência de doenças e lesões ósseas. Isto pode ser tornar uma séria ameaça à qualidade de vida da população do Mundo, especialmente para a população mais envelhecida, estes problemas vão criar uma maior necessidade de implantes ósseos. Na maior parte dos casos os implantes usados são implantes metálicos e enquanto estes apresentam excelentes propriedades mecânicas, muitas vezes apresentam uma resposta biológica insuficiente. A resposta biológica destes implantes pode ser melhorada modificando-os com biomateriais. O poli (L-ácido láctico) (PLLA) é um polímero aprovado pela US Food and Drug Administration (FDA) para usos médicos, e é também biocompatível e biodegradável, além disso apresenta também uma propriedade interessante a piezoelectricidade. Esta propriedade é encontrada naturalmente no osso e pensa-se que desempenhe um papel importante na regeneração óssea. A resposta piezoelétrica do PLLA é altamente dependente do seu grau de cristalinidade. Neste trabalho filmes de PLLA vão ser utilizados como um revestimento para substratos de aço inoxidável, onde as influências de diferentes parâmetros na cristalização do filme vão ser estudados, estas variáveis incluem tratamento do substrato, temperatura de cristalização, métodos de cristalização, taxa de arrefecimento e a concentração da solução de PLLA utilizada para preparar os filmes. As diferentes amostras vão ser caracterizadas durante as diferentes fases do processo de forma a ter uma melhor compreensão de como os diferentes parâmetros o estão a afetar. A compreensão do efeito dos diferentes parâmetros nos filmes permitirá o ajuste das propriedades do filme de PLLA e consequentemente do implante ósseo de acordo com as necessidades de situações específicas. Finalmente os filmes serão caracterizados em relação à sua resposta biológica através de testes *in-vitro* e *in-vivo*. Os resultados obtidos mostram que o tratamento UV dos substratos é superior ao tratamento térmico, visto que estas amostras não apresentam formação de óxido de cromo e apresentam uma maior cristalinidade. A adesão dos filmes é altamente influenciada pela sua cristalização e pela silanização do substrato. As amostras produzidas neste trabalho são bioativas visto que houve formação de apatite nos testes SBF.

keywords

PLLA, Piezoelectricity, Stainless steel, Biomaterials, Bone implants, Crystallinity

abstract

The increase in life expectancy comes associated with an increased incidence of bone disease and lesions. This can become a serious threat to the quality of life of the world's population, especially for older people, these problems will cause an increase in the need for bone implants. In most cases metallic implants are used and while these excel at mechanical properties, they often have lacking biological responses. The biological response of these implants can be improved by modifying them utilizing biomaterials. Poly (L-lactic acid) (PLLA) is a polymer that is US Food and Drug Administration (FDA) approved for medical uses, biocompatible and biodegradable, presenting an interesting property, piezoelectricity. This property is naturally found in the bone and is believed to play an important role in its regeneration. The piezoelectric response of PLLA is highly dependent on its crystallinity. In this work PLLA films will be used to coat stainless steel substrates, and the influence of different parameters on the film crystallization process will be studied. These variables include substrate treatment, crystallization temperature, crystallization methods, cooling rate and concentration of the PLLA solution used to produce the film. The different samples will be characterized at the different stages of the process, to have a better understanding on how the different parameters are affecting it. The understanding of the effect of the different parameters on the PLLA films would allow to tailor the properties of the PLLA film and consequently the bone implant according to the needs of a specific situation. Ultimately the films will be characterized in relation to its biological response via *in-vitro* and *in-vivo* tests. The obtained results showed that UV treatment of the substrate is superior to thermal treatment, since these samples showed no formation of chromium oxide and presented higher crystallinity. The adhesion of the films is highly influenced by its crystallization and the silanization of the substrate. The samples produced in this work are bioactive, since there was the formation of apatite in the SBF tests.

Contents

List of Figures	iii
List of Tables.....	vi
Abbreviations	viii
Chapter 1 - Context and objectives.....	2
1.1. Context.....	3
1.2. Objective.....	5
Chapter 2 – State of the Art.....	7
2.1. Bone	8
2.2. Bone Implants	10
2.2.1. Ceramic Implants	11
2.2.2. Metallic Alloy Implants	12
2.2.2.1. Stainless steel.....	13
2.2.2.2. Titanium-based alloys.....	14
2.2.2.3. Chromium Cobalt Alloys.....	15
2.3. Hard Tissue Engineering.....	15
2.4. Biopiezoelectricity	16
2.5. Poly (L-Lactic Acid)	20
2.5.1. Poly (L-Lactic Acid) Crystallinity	22
2.6. Polymer-Metal Interface	25
Chapter 3 – Materials and Methods.....	28
3.1. Materials	30
3.2. Methods	31
3.2.1. Preparation of Stainless Steel.....	31
3.2.2. Surface Functionalization	31
3.2.2.1. Thermal treatment.....	32
3.2.2.2. UV irradiation.....	33
3.2.3. Silanization process	33
3.3. PLLA solution preparation.....	34
3.4. PLLA film deposition	36
3.5. PLLA film crystallization	37
3.6. PLLA film polarization.....	38
3.7. Characterization methods.....	40
3.7.1. Fourier Transform Infrared Spectroscopy.....	40
3.7.2. Optical microscopy	41
3.7.3. Scanning Electron Microscopy	41
3.7.4. Atomic Force Microscopy	41
3.7.5. Contact Angle	44
3.7.6. Differential Scanning Calorimetry.....	46
3.7.7. X-Ray Diffraction	46
3.7.8. Substrate characterization	48
3.8. Film characterization	48
3.9. Simulated Body Fluid Tests.....	48
3.10. Adhesion tests	49
3.11. Celular tests.....	52
3.12. In Vivo tests	52
Chapter 4 – Results and Discussion	53
4.1. Characterization of 316L SS substrates after pre-treatment.....	54
4.2. Characterization of 316L SS substrates after silanization.....	62
4.3. Characterization of PLLA films through Differential Scanning Calorimetry.....	69
4.4. Crystallization of PLLA films.....	70
4.5. PLLA films adhesion	88
4.6. Polarization of PLLA films by Corona discharge	93
4.7. Simulated Body Fluid tests	96

Chapter 5 Conclusion and Future Works.....	100
5.1. Conclusion.....	101
5.2. Future Works	103
References	104
Annex	111
Annex A	112

List of Figures

Figure 1. The hierarchical structure of the bone in it can be observed the trabecular (spongy) and compact bone, as well as the blood vessels to provide diffusion of nutrients and growth factor, which are important for the proper functioning of the bone.	9
Figure 2 - The bone remodeling process that is the process through which the bone renews itself by using osteoclasts to absorb old bone and osteoblasts start depositing new ECM	10
Figure 3. The schematic representation of the piezoelectric effect, in which it is possible to observe the direct effect where mechanical strain generates an electrical output, and the inverse piezoelectric effect where an electrical field generates mechanical strain on the material	17
Figure 4. Schematic representation of the dipoles reorientation when subjected to mechanical stress, this reorientation will generate charges on the surface of the material	18
Figure 5. Representation of the axis system used to describe the piezoelectric constant where 1,2 and 3 correspond to the x, y and z axis respectively and 4,5 and 6 representing shear around the x, y and z axis respectively.....	19
Figure 6. Possible enantiomer for lactic acid and lactide.....	21
Figure 7. Proposed model to the α and β forms of PLLA.....	23
Figure 8. Maltese cross pattern observed in a spherulite viewed under polarized light using a optical microscope.	24
Figure 9. Schematic representation of the work done during this thesis.	30
Figure 10. Schematic representation of the silanization process.	32
Figure 11. Thermal schedule used in the thermal treatment of the 316L SS substrates.	33
Figure 12. Setup of the equipment used in preparation of the PLLA solution.	35
Figure 13. Schematic representation of the spin coating process. i) Fluid deposition; ii). Substrate acceleration; iii) Fluid outflow; iv) Evaporation phase; v) Final film. Based on [99].....	37
Figure 14. Thermal schedules used in the crystallization of PLLA: 120° C for 60 minutes (i) and 180° C for 3 minutes followed by 45 minutes at 120° C	38
Figure 15. Pictures of the exterior of the lab made corona polling device that was used to polarize the samples (left) and of its interior (right).	40
Figure 16. Representation of the AFM technique[23].	42
Figure 17. Expansion and contraction of the sample electric domains. Polarization (P) of the piezoelectric domain is (a) parallel and (b) anti-parallel to the applied electric field (E).....	43
Figure 18. Schematic representation of the three phase-system and the contact angle.....	45
Figure 19. Schematic representation of the cross-hatch tape test process	50
Figure 20. Picture of Pristine 316L SS (left), thermally treated 316L SS (middle) and UV treated 316L SS (right).....	54
Figure 21. FTIR spectrum of a pristine 316L SS substrate (black line) and 316L SS substrates after thermal (red line) and UV treatment (blue line).	55
Figure 22. SEM micrographs of pristine 316L SS and UV treated 316L SS with different ampliations	57
Figure 23. AFM topography, electrostatic forces and work function scans acquired on 316L SS before and after treatments, including thermal, UV, UV/Ozone and UV/Nitrogen.	59
Figure 24. Images of the contact angle on pristine 316L SS (a), thermally treated 316L SS (b) and UV treated 316L SS (c) captured during the measuring process. It is possible to observe different contact angles according to the different treatments.	61
Figure 25. FTIR spectrum of silanized 316L SS substrates. The 316L SS substrates were subjected to different treatments before silanization, which include thermal (red line) and UV treatment (blue line). It is possible to observe the vibrational modes corresponding to the silanes in both the spectra.	62
Figure 26. SEM micrographs of silanized thermally treated 316L SS with different ampliations. These micrographs were obtained using an electron acceleration field of 4.0 kV. In the micrographs it is possible to observe the appearance of small spheric structure which are thought to be the silanes.	66
Figure 27. SEM micrographs of silanized thermally treated 316L SS (a) and silanized UV treated 316L SS (b) subjected to EDS analysis. The red represents silicon and the green represent iron.....	66
Figure 28. AFM topography and work function scans acquired on 316L SS after thermal or UV pre-treatment followed by silanization.	67
Figure 29. Images of the contact angle on thermally treated and silanized 316L SS and UV treated and silanized 316L SS captured during the measuring process. Even though the samples were subjected to different treatments the contact angle values seem about the same.....	68

Figure 30. XRD pattern of a sample with the crystalline α form of PLLA present (left) and XRD pattern of a sample with amorphous PLLA (right).....	71
Figure 31. Crystallinity degree of the different samples crystallized in Linkam stage in function of the cooling rate. These samples were subjected to either UV treatment without silanization or Thermal treatment followed by silanization crystallized with a heating rate of 5°C/min with various cooling rates (0.5, 2.5, 5, 10, 20). The samples were prepared using two different concentration of PLLA solution 2.5 wt.% (A) and 5.0 wt.% (B).	73
Figure 32. Crystallinity degree of the different samples crystallized in Linkam stage and heating plate in function of the cooling rate. These samples were subjected to either UV treatment without silanization or Thermal treatment followed by silanization crystallized with a heating rate of 5°C/min and a cooling rate of 5°C/min. UV- UV treatment; TT – Thermal Treatment; TP- Crystallized on thermal plate; L- Crystallized on Linkam stage.	74
Figure 33. Thermally treated and UV treated substrates with PLLA films crystallized at 180°C for 3 minutes followed by 45 minutes at 120°C under different parameters, with cooling rates of 2.5,5 and 10°C/min observed on the stereo microscope.	75
Figure 34. Thermally treated and UV treated substrates with PLLA films crystallized at 180°C for 3 minutes followed by 45 minutes at 120°C under different parameters observed on the stereo microscope. It is possible to see in figure 24 that the film completely peeled of the substrate due to poor adhesion.	76
Figure 35. Thermally treated and UV treated substrates with PLLA films crystallized at 120°C for 60 minutes under different parameters observed on the stereo microscope.	77
Figure 36 - SEM micrographs with different magnifications of the thermally treated and silanized samples crystallized in the Linkam stage for 3 minutes at 180°C followed by 45 minutes at 120°C with different magnifications, using cooling rates of 2.5,5.0 and 10°C/min.	78
Figure 37. SEM micrographs of the UV treated samples crystallized in the Linkam stage for 3 minutes at 180°C followed by 45 minutes at 120°C with different magnifications, using cooling rates of 2.5,5.0 and 10°C/min.....	79
Figure 38. - SEM micrographs of the thermally treated and silanized samples crystallized in the Linkam stage for 3 minutes at 180°C followed by 45 minutes at 120°C with different magnifications, using cooling rates of 0.5 and 20°C/min	81
Figure 39. SEM micrographs of the UV treated samples crystallized in the Linkam stage for 3 minutes at 180°C followed by 45 minutes at 120°C with different magnifications, using cooling rates of 0.5 and 20°C/min.....	82
Figure 40. SEM micrographs of the thermally treated and silanized samples and UV treated samples crystallized in the thermal plate for 3 minutes at 180°C followed by 45 minutes at 120°C with different magnifications, using a cooling rate of 5. °C/min.....	84
Figure 41. SEM micrographs of the thermally treated and silanized samples crystallized in the Linkam stage for 60 minutes at 120°C with different magnifications, using cooling rates of 5. °C/min	85
Figure 42. SEM micrographs of the thermally treated and silanized samples crystallized in the Linkam stage for for 60 minutes at 120°C with different magnifications, using cooling rates of 5. °C/min.....	86
Figure 43. AFM topography, work function scans and piezoelectric response acquired on 316L SS pre-treatment (UV and Thermal) followed by silanization and crystallization on the heating plate using a heating rate of 5°C/min and a cooling rate of 5°C/min.....	87
Figure 44 Images of substrates subjected to Thermal and UV treatment followed by silanization and a Pristine 316L SS with PLLA films after being subjected to the cross-hatch tape test, the samples were analysed with a stereo microscope with an ampliation of 8x (left), optical microscope with an ampliation of 20x (middle) and optical microscope with polarized light (right).	89
Figure 45. Stereo microscope images of 316L SS substrates with deposited PLLA films and crystallized. The samples were subjected to different pre-treatments: Thermal with silanization, UV with silanization and UV without-silanization. The cross hatch tape test was then performed after 0, 2, 7 or 14 days, in order to evaluate the evolution of the film adhesion with the time.	91
Figure 46. Crystalline PLLA films deposited on thermally treated and silanized 316L SS substrates that were polarized with electrical fields of different voltages. The samples were then observed under the stereo microscope and optical microscope with polarized light.....	94
Figure 47. Crystalline PLLA films deposited on thermally treated and silanized 316L SS substrates that were polarized with electrical fields of different voltages. The samples were then observed in SEM under different magnifications.	95
Figure 48. SEM micrographs with different magnifications of 316LSS substrates subjected to thermal treatment and silanized, without PLLA(TTS) and with PLLA crystallized at 180°C for 3 minutes followed by	

45 minutes at 120°C (180) and crystallized at 120°C for 60 minutes (120); Pristine 316L SS (Pristine) and thermally treated 316L SS with no silanization (Thermal no Sil) after 14 days of immersion in SBF.	98
Figure 49. SEM micrographs with different magnifications of 316LSS substrates subjected to thermal treatment and silanized, without PLLA(top) and with PLLA crystallized at 180°C for 3 minutes followed by 45 minutes at 120°C (middle) and crystallized at 120°C for 60 minutes (bottom), after 28 days of immersion in SBF.....	99

List of Tables

Table 1- Mechanical properties of the most commonly used alloys in bone implants	13
Table 2 - Composition of 316L SS (all compositions are presents in wt. %)	14
Table 3. Classification of tape test results according to standard ASTM D3359.....	51
Table 4 FTIR peak assignment for 316L SS before and after thermal or UV treatment.....	56
Table 5. Work function of the 316L SS substrates after the different treatments as determined by AFM.	60
Table 6. Contact angle values obtained for the 316L SS substrates subjected to the different treatments.	61
Table 7.. FTIR peak assignment for 316L SS subjected to Thermal or UV treatment and posteriorly silanized.....	63
Table 8. Contact angle values obtained for the 316L SS substrates subjected to the different treatments.	68
Table 9. Transition temperatures for amorphous PLLA films prepared with solutions with various concentrations (2.5 and 5.0 wt%) determined by DSC using diffrent cooling rates (2 ,5 and 10 °C/min).	69
Table 10 List of different cooling rates used on the crystallization of PLLA films.....	71
Table 11. pH and mass values of the samples before and after immersion in SBF.	112

Abbreviations

316L SS - 316L Stainless Steel
AC - Alternating current
AFM – Atomic Force Microscope
APTES - (3-Aminopropyl)triethoxysilane
DC – Direct current
DSC – Differential scanning calorimetry
ECM – Extra Cellular Matrix
EDS – Energy Dispersive Spectroscopy
FDA – U.S. Food and Drug Administration
FTIR – Fourier-transform Infrared Spectroscopy
KPFM – Kelvin Probe Force Microscopy
PDLA – Poly (D-Lactic Acid)
PDLLA - Poly (D,L-Lactic Acid)
PEO – Polyethylene Oxide
PFM – Piezoelectric Force Microscopy
PHB – Poly (3-hydroxybutirate)
PHBV - Poly (3-hydroxybutirate-co-3-hydroxyvalerate)
PLA – Polylactic acid
PLLA – Poly(L-lactic acid)
PVDF – Polyvinylidene Fluoride
SBF – Simulated Body Fluid
SEM – Scanning Electron Microscopy
TrFE - Trifluoroethylene
VDF – Vinylidene Fluoride
VDF-TrFE - Vinylidene Fluoride-co- Trifluoroethylene
XRD – X-Ray Diffraction
hDPSCs – Human Dental Pulp Stem Cells
wt.% - Weight Percentage
 μ CT – Micro Computed Tomography

Chapter 1 - Context and objectives

Chapter 1 – CONTEXT AND OBJECTIVES

1.1.Context

With the increase of life expectancy and aging of the population bone health conditions and bone diseases prevention are getting more and more important. These can become a serious threat to the quality of life of the worlds' population, especially in older people[1]. In most cases, if the injury to the bone is small the bone will be able to regenerate itself. However in the cases of extensive bone trauma and some diseases like osteoporosis, the bone's regeneration ability is not enough, and there is the need for intensive therapy or a bone implant [2]. During the last decade, there was an increase in the number of surgeries for hard tissue repairment and regeneration with costs of billions of dollars annually worldwide[2,3].

Bone implants play a crucial role in the patient rehabilitation and the most commonly used option is a metallic implant[2,4], with the majority of the implants being metal alloys such as stainless steel, titanium alloys, and cobalt-chromium alloys. While metals have remarkable mechanical properties, load-bearing, and fatigue resistance, they often lack in biocompatibility and bioactivity[4]. A bioengineering research branch called tissue engineering aims to solve this problem by studying the natural properties of the bone and the bone tissue regeneration processes in order to modify or create materials mimicking those properties and processes[5].

There are several approaches that propose to improve the bone cells adhesion to the artificial implants, such as surface modifications or coating using polymers or ceramics. Coating of the metal alloy using a piezoelectric material presents advantages due to electrical cues produced that can potentially be utilized to improve cell adhesion and bone regeneration[1,6]. The electrical cues mentioned before occur naturally in the bone, thanks to one crucial property, its piezoelectricity. This property was reported for the first time in 1957 by Fukada et al.[6] and consists of the ability of bone to generate an electric field when an external force is applied causing deformation[7]. These generated electrical signals are believed to be biological signals that play an important role in bone tissue regeneration and remodeling[8]. Piezoelectric properties can be conferred to metallic implants by using a piezoelectric material such as PLLA to coat the implant.

Poly (L-lactic acid) (PLLA) is a semi-crystalline polymer that shows piezoelectric properties [6,9]. The origin of the piezoelectric activity of PLLA originates from its C=O dipoles that rotate when shear stress is applied causing electrical polarization[10]. These dipoles are present in the crystalline regions of PLLA, regions which are highly oriented[11,12]. This causes the piezoelectric response of PLLA to be directly dependent on degree of crystallinity of the PLLA.[11,12] The latter means that the processing conditions of PLLA can affect the final piezoelectric activity of the functional film and its effectiveness on bone tissue regeneration. PLLA is a also polymer which is approved by the US Food and Drug Administration (FDA) for medical uses,[13] that assumes biocompatibility and biodegradability. All these properties make PLLA a strong candidate to use in a polymeric coating for bone implants[14].

One of the main requirements for the success of the implant is that its coating must present a strong bond to the metallic part of the implant. However due to the considerable differences in physicochemical and mechanical properties between polymers and metals in general, including those of thermal expansions coefficient, cohesive energy, and wettability[15–17], the task of adhesion becomes very difficult[18, 19]. From the literature review, it is known that modifications to the interface between the metal and polymer may change the adhesion properties [15,16,20,21] . This task can be achieved by modifying the surface of metal substrate, to increasing surface tension and roughness or by changing the surface chemistry[18].

Previously, work on this project “Advanced BioMEMs for tissue engineering: applications in hard tissue (BioMEMs)”, POCI-01-0145-FEDER-032095 includes: The study of the silanization reaction as a method to improve the adhesion of poly (L-lactic acid) (PLLA) films to 316 L SS substrates and to achieve physicochemical stable PLLA coatings. The results revealed that the functionalization of the metal substrate with silanes is effective and efficient in the adhesion of PLLA films to 316 L SS. Depending on film thickness, polymer concentration solution and degree of crystallization of the polymeric film, differences on the degree of adhesion were demonstrated[22,23]. The most suitable results in terms of adhesion was then reproduced for *in vitro* tests. The Presto Blue TM viability assay showed that the PLLA film increased the cell viability on the substrates. Osteogenic differentiation assay showed that PLLA film enhanced the innate osteogenic potential of the cells and the osteogenic differentiation. The SEM

images allowed seeing the presence of the normal morphology of fibroblast cells and its layer formation on PLLA film[23,24].

1.2.Objective

The purpose of this master thesis is to study possible ways of improving adhesion between the class of metals represented in this work by medical stainless steel 316L (316L SS) and the class of polymers represented by the PLLA film. More precisely, in this thesis the influence of the metal surface treatment and the degree of crystallinity of PLLA on functional properties of the modified final SS316L/PLLA implant were studied.

This thesis is divided into four main chapters: state of the art, materials and methodologies, results and discussion, and conclusions. In state of the art, a brief review of the studies and results already obtained in this field and an explanation of some practical concepts for a thorough understanding of thesis work is presented. Afterward, the methodology used to obtain all the reported results is described and explained, along with the techniques used. The following chapter presents the results in detail, followed by an extensive discussion, where the samples are compared to each other and to other work. By the end, the main conclusions and some future work proposals are presented.

Chapter 2 – State of the Art

Chapter 2 – STATE OF THE ART

2.1. Bone

The skeleton as an organ is essential as it provides support for the body, tendons, and muscles, consequently allowing its movement. It protects organs contained in the thoracic and cranial cavities and serves as a mineral reservoir which can release those minerals when needed, helping maintain homeostasis in the body[25].

At a microscopic level, the bone composition can be divided into two main components, the bone cells (osteoblasts, osteoclasts, and osteocytes) and the extracellular matrix (ECM). The ECM is made of an organic matrix (60 %) which is mainly composed of crosslinked collagen type I fibrils (90 %) and has mineral binding non-collagenous proteins (10 %), and of an inorganic matrix (40 %) which is mainly composed of hydroxyapatite[26-28]. At a histological level, the bone can be divided into two types of bone: cortical bone and cancellous bone, as shown in **Figure 1**. Cortical bone is highly mineralized (80-90 % mineralization) and is often in the outer part of the bone, this type of bone is dense and hard, and its primary function is to provide resistance to torsion, bending, and compressive forces. Trabecular bone presents a mineralization of 15-20 % and has a high porosity which allows for a highly vascularized architecture and high surface area. For these reasons, the trabecular bone's main function is to provide diffusion of nutrients and growth factors[27,29].

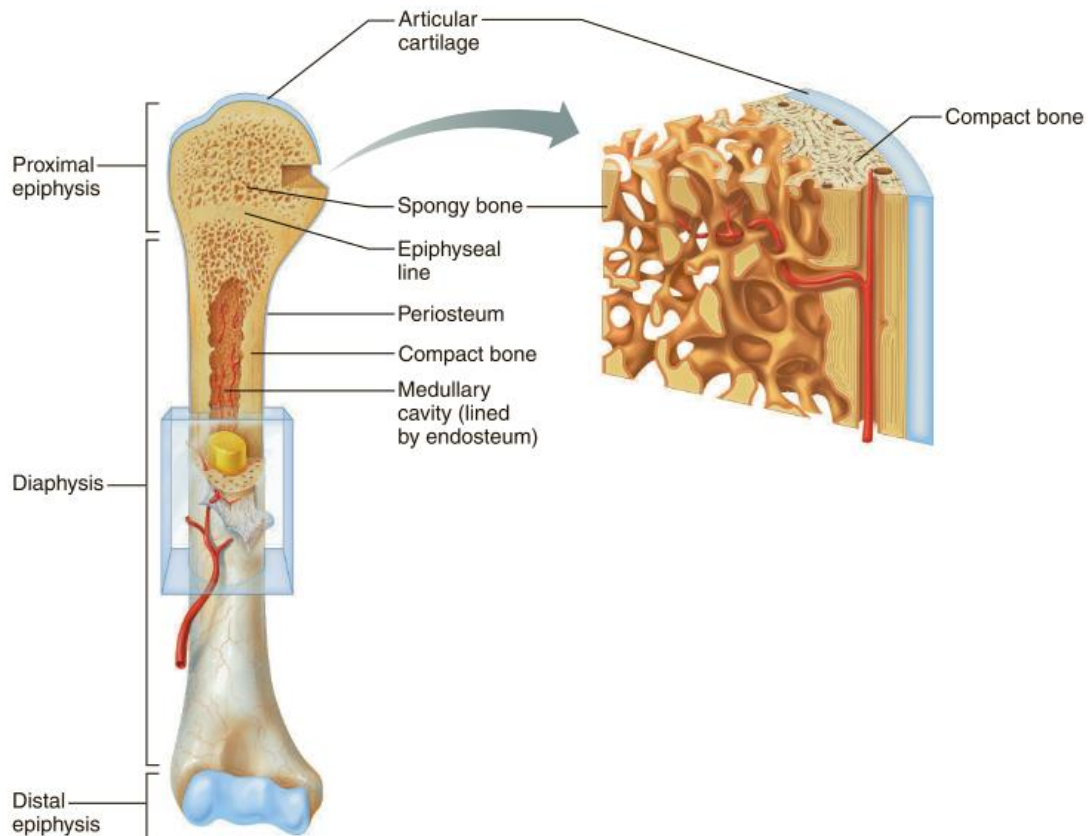


Figure 1. The hierarchical structure of the bone in it can be observed the trabecular (spongy) and compact bone, as well as the blood vessels to provide diffusion of nutrients and growth factor, which are important for the proper functioning of the bone[30].

The bone is a dynamic tissue and is being constantly renewed to maintain proper function, structural integrity, and mineral homeostasis. This happens through the process of bone remodeling (**Figure 2**), which is a highly coordinated process that may last 4-5 months. This process is divided into 5 phases: activation, resorption, reversal, formation, and quiescence. In the first phase, activation, a signal will be generated in response to a stimulus which can be a mechanical strain on the bone that may cause damage and subsequently trigger osteocytes to generate a remodeling signal. In the second phase, resorption, osteoblasts respond to the signal generated in the activation phase by recruiting osteoclast precursors, which will undergo osteoclastogenesis, when the osteoclasts are fully differentiated, they will absorb the ECM. In the third phase, reversal, the osteoclasts will disappear, and mononuclear cells will remove what is left over from the resorption preparing the surface for bone formation. In the formation phase, osteoblasts are recruited and start to deposit a new extracellular matrix in the area where the old bone was absorbed. The last

phase, termination, happens when all the resorbed bone has been replaced and mineralized, and termination signals are emitted[31-33].

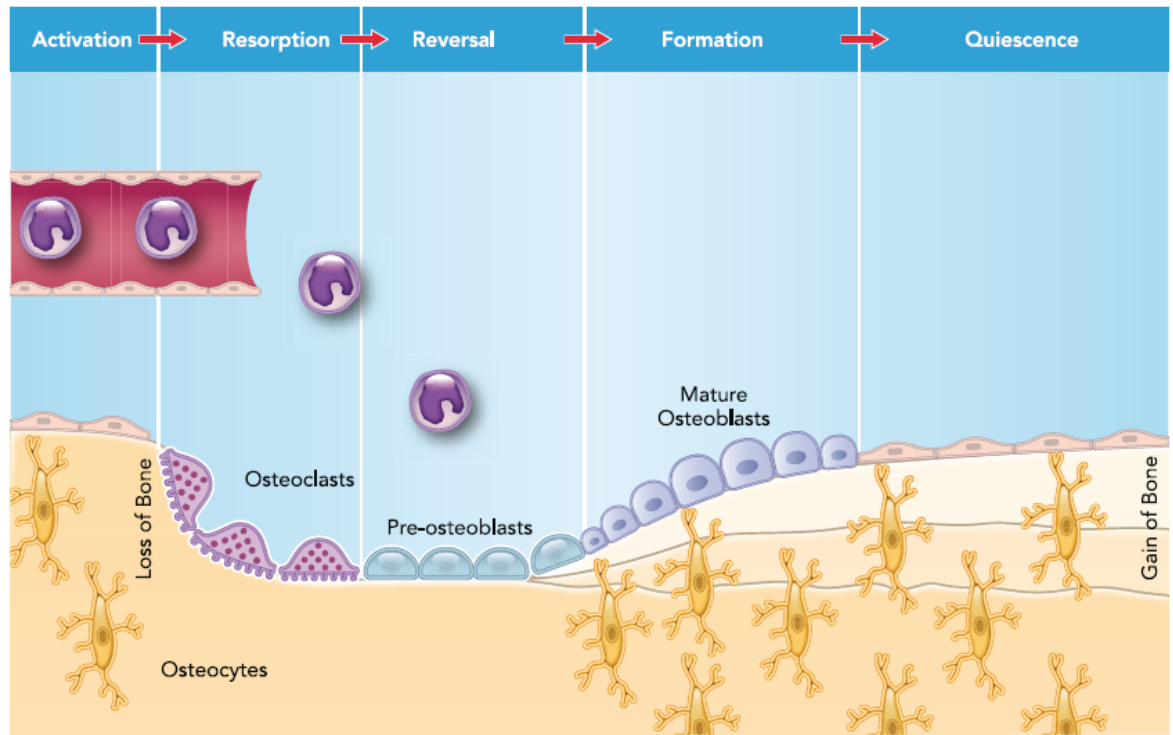


Figure 2 - The bone remodeling process that is the process through which the bone renews itself by using osteoclasts to absorb old bone and osteoblasts start depositing new ECM [33]

2.2. Bone Implants

Even though the bone has regeneration capacity, it cannot regenerate itself in case of significant defects. Moreover, the increase in life expectancy is accompanied by the aging of the population which will cause an increase in the prevalence of bone disease and conditions. These all cause an increased need for surgeries to the bone since it will not be able to repair itself. [1-3].

Ideally in these cases an autologous bone graft, where bone is harvested from one site in the patient and implanted in another site in the same patient. However, due to problems such as limited bone availability and donor site morbidity this approach is not viable in most cases[2,34]. There is also the possibility for allografts where the bone graft comes from a donor. However, that method has several limitations caused by the possibility of rejection and the transmission of diseases. In some cases, there is also the possibility of a xenograft that uses an animal donor as the source of the bone graft[31]. However this method has all

of the disadvantages associated with an allograft with a higher rejection chance and the risk of transmission of zoonotic diseases[2,34].

With all those associated risks and limitations when using a natural source for the bone implants, the transplantation is often not possible or undesirable. For this reason, synthetic bone grafts are often used.

When the used material causes no adverse reaction, it can be considered biocompatible. Biocompatible materials can then be bioinert in case they don't interact with the surrounding tissues or bioactive in which case they will cause a response within the body to improve its integration. The material can also undergo degradation or dissolution after being implanted thus is classified as biodegradable. Ideally, biodegradable implants should bear all the load when implanted, and as bone starts to form, the load should start to gradually be supported by the bone until all the implant has degraded and the newly formed bone bears all the load, ultimately the degradation rate of the implant should match that of the bone formation. The most commonly used materials for load-bearing implants are ceramics and metals[35].

2.2.1. Ceramic Implants

Ceramics as a biomaterial show good biocompatibility and a low toxicity due to being more chemically inert than metals, thus preventing the leaching of toxic ions. Even though ceramics have good resistance to compression and shear strain, they have the disadvantage of presenting poor tensile toughness and fracture toughness that can be problematic when using ceramics as load-bearing implants[35,36].

Ceramic implants can be bioinert, such as alumina and zirconia, which were previously used in total hip replacement and nowadays are used in knee replacements and as the femoral head in total hip replacements while using metal for the rest of the implant in order to decrease friction[36,37]. There are also some bioactive ceramics, such as calcium phosphates. The most prominent calcium phosphates are hydroxyapatite (HAP) and tricalcium phosphate; with hydroxyapatite being the main constituent of the bone mineral component. Calcium phosphates present great bioactivity and can be biodegradable. It is possible to tune these properties by changing the calcium to phosphate ratio, which can be achieved by changing the quantity of raw materials or by heat treatment. The solubility can also be changed by doping the material with cations or by changing the crystallinity. Calcium

phosphates by themselves are almost never used for load-bearing applications and for that reason their mechanical properties are not very important[35,37].

Ceramics can also be used for bone implants in the form of bioactive glass which are composed of silica (SiO_2), calcium oxide (CaO), sodium oxide (Na_2O), and phosphorus pentoxide (P_2O_5). The first bioactive glass, 45S5 Bioglass, was developed by Larry Hench in the late 1960s to try and overcome the lack of tissue integration when using metallic implants. Bioactive glasses have great bioactivity and can bind to the bone by forming a layer of carbonated hydroxyapatite, leading to biological fixation. Bioactive glasses have a higher solubility than other ceramics, which comes from the fact that when in contact with water the SiO_2 in bioactive glass will react forming $\text{Si}(\text{OH})_4$, which after polycondensation will form an Si-O-Si bond and form a silica gel. The breakdown of the silica network will also cause the release of calcium, sodium, and phosphate ions which will form an amorphous hydroxy carbonate apatite together with the silica gel, which will then crystalize. The main application of bioactive glasses is as a filler for small bone defects.[35,37]

2.2.2. Metallic Alloy Implants

Metallic alloy implants are the more prevalent solution in cases where there is the need for implants. Some of the most commonly used alloys include stainless steel 316L, cobalt-chromium alloy, and titanium alloys. While metal alloy implants present great mechanical properties, load-bearing, and fatigue resistance, they lack in biocompatibility and bioactivity and can be prone to corrosion which can lead to the release of metallic ions that may become toxic[4].

Metallic materials started being used in medical implants in the 19th century, where initially they were used in bone repair, like fractures and bone fixation. Since then, the uses of metallic materials have evolved, and now they are widely used, from small temporary devices, like pins and screws to permanent devices, like joint implants. It is estimated that nowadays metallic biomaterials account for 70 to 80 % of all the implants made.[38,39]

Despite there being a large number of different available metals and the capacity to process them, not all the metals can be used as biomaterials. When considering a metallic material to use in an implant, there are five criteria that ideally should be met: 1) good biocompatibility and non-toxicity; 2) high resistance to corrosion; 3) adequate mechanical properties; 4) wear resistance and 5) osseointegration [38,39].

When considering the mechanical properties of the metal or alloy to be used, the main mechanical properties to consider are the Young's Modulus, tensile strength, and toughness. The mechanical properties of the chosen material should be similar to those of the bone in order to provide supporting functions, and while many metals provide adequate properties to bear loads and undergo plastic deformation, they have Young's modulus considerably higher than that of the bone. This difference can cause an uneven distribution of the load, causing the implant to bear most of the load which, consequently, may cause the bone to suffer atrophy. This phenomenon is called stress shielding effect [38,39]. The corrosion of the implant is also an important factor to consider since the physicochemical environment of the body can cause metals to corrode, which can lead to the release of metal ions that in large quantities are toxic. Ideally, the corrosion resistance of the implant should allow it to remain in the body for at least 30 years under normal conditions.[38,39]

Nowadays, there are three major types of metal alloys being used in bone tissue engineering and implants: medical stainless steel alloy (SS316 L), titanium-based alloys, and cobalt-chromium alloys ³⁶. The different alloys have different mechanical properties as shown in **Table 1** and excel at different aspects. SS316L shows a higher ductility and cyclic twist strength [38,39]. Titanium-based alloys present the best biocompatibility, corrosion resistance and specific strength [38,39]. The cobalt-chromium alloys show the greatest wear resistance.[38,39] The main focus of this thesis are SS316L alloys. While in some cases the properties of the alloy may be satisfactory to its purpose, many times there is a need to alter certain surface-related properties which can be done through surface modifications or the use of a coating[40].

Table 1- Mechanical properties of the most commonly used alloys in bone implants [40].

Material	Young's Modulus (GPa)	Ultimate tensile strength (MPa)	Fracture toughness (MPa·m ^{-1/2})
316L stainless steel	200	540-1000	100
Ti alloys	102-125	900	80
CoCrMo alloys	240	900-1540	100

2.2.2.1. Stainless steel

Chapter 2 – STATE OF THE ART

Stainless steel is the name given to iron-based alloys that contain a high percentage of chromium and certain amounts of nickel[41]. Stainless steels can be divided into groups based on their microstructure: martensitic, ferritic, austenitic, or duplex (both austenitic and ferritic)[41]. In implants the only type used is austenitic stainless steel since it shows good corrosion resistance and mechanical strength[39]. The main austenitic stainless steel used is 316L SS[42]. 316L SS composition is presented in **Table 2**.

Table 2 - Composition of 316L SS (all compositions are presents in wt. %) [42].

Cr	Ni	Mo	Mn	Si	P	N	C	Fe
16-18	10-14	2-3	2.0 max	0.75 max	0.45 max	0.1 max	0.03 max	60 min

Chromium helps prevent the rusting and corrosion of the stainless steel since it has a great affinity for oxygen which allows for the formation of an adhesive chromium oxide film that protects the stainless steel. Despite nickel being highly toxic, a small amount helps prevent corrosion by forming protective oxide films and stabilize the formation of the austenitic phase in iron[41]. Even though some elements in the alloy help prevent corrosion, it is often not enough in prosthesis application and for that reason the 316L SS implants still suffer from corrosion considering long-term uses.[39]

2.2.2.2. Titanium-based alloys

Titanium by itself presents several advantages compared to the other used alloys such as lower density, low Young's modulus, corrosion resistance, and superior biocompatibility[41]. The lower density of titanium means that compared with a prosthesis of the same size made of stainless steel or Chromium-cobalt alloy it would weigh significantly less, allowing for a more effortless movement. The lower Young's modulus would help avoiding the stress shielding effect. Titanium capacity to resist corrosion comes from its ability to form an adherent oxide layer which can regenerate inside the body if damaged [39]. Titanium is also the only metal alloy that can bind directly with the bone.[39,42]

Since titanium already presents good biological properties, alloying is used as a way to improve its mechanical properties while trying not to change the Young's modulus. The Ti-6Al-4V alloy is commonly used, however, the aluminum in the alloy can create toxicity

problems[39,42]. Another problem with using titanium alloy over stainless steel is its very high price when compared to that of SS316L[43].

2.2.2.3. Chromium Cobalt Alloys

Chromium-cobalt (Cr-Co) alloys show a superior corrosion resistance when compared to stainless steel due to its high chromium content, which will form a passive oxide layer to protect the implant. Cr-Co alloys have comparable mechanical properties to those of stainless steel, Mo and Ni also contribute to the corrosion resistance and tungsten contributes to the solid solution strengthening but can also decrease the corrosion resistance and corrosion fatigue of the alloy³⁹. These cause some compositions of the alloy to only be suitable for short-term implantation.

Chromium-cobalt alloys can also cause toxicity problems since the high levels of cobalt can cause serious health problems, and in metal-on-metal implants, the created debris will release cobalt and chromium into the blood[44]. This alloy is difficult to machine, so the choice of the production method will be an exchange between cost and properties, with forged, cold worked, or hot isostatic press alloys having significantly better mechanical properties over casted alloys[41]. In general, these alloys have higher fatigue resistance than stainless steel but suffer from drawbacks such as toxicity, stress shielding (Cobalt-chromium alloys have a Young's modulus of 220-230 GPa while the bone has 20-30 GPa), and being more expensive than stainless steel[39,42].

2.3. Hard Tissue Engineering

Tissue engineering is a multidisciplinary approach that applies principles of engineering, material sciences, and cell biology to develop new materials or improve existing ones to further use to replace damaged tissue or organs[45,46]. Tissue engineering creates new approaches to treat injuries and diseases that overcome some problems of the currently available treatments such as infection, immune rejection, chronic donor-site pain and morbidity[45,46].

Initially, tissue engineering developed biomaterials that tried to match the properties of the target tissue while having minimal toxic effects. Those are called first-generation biomaterials. In the second generation, the focus shifted to produce bioactive materials that could achieve a controlled reaction to stimulate regeneration, another advance in the second

generation of biomaterials was the development of resorbable biomaterials, which showed controlled degradation. Nowadays, we are in the third generation of functional or smart biomaterials, which are able to have a stimulating effect on cells or tissues by responding to internal or external stimulus[3,47].

When considering biomaterials for use in bone tissue engineering, preferably the material should be able to replicate the mechanical and biological properties of the bone while providing an adequate structure for the bone to grow in. The implant should also provide an adequate surface and the proper degradation kinetics so that the scaffold degrades as the bone grows. Preferably the material should also be osteoinductive (ability to promote the differentiation of progenitor osteoblastic cells), osteoconductive (ability to support bone growth and encourage the ingrowth of the surrounding bone), and capable of osseointegration (ability to integrate with the surrounding bone) [48-50]. Considering the metal alloy prosthesis, the surface modification is crucial to provide these properties to improve the implant material as well as ensure a better tissue-implant interaction with the other option being the use a functional biocoating[51].

2.4. Biopiezoelectricity

The suffix piezo in piezoelectric come from the Greek work “piezo” which implies putting pressure to generate electricity. The piezoelectric effect manifests itself in two ways: 1) direct piezoelectric effect, in which the piezoelectric material generates an electrical output in response to external mechanical stress, being that the intensity of the generated electrical signal is directly proportional to the intensity of the mechanical stress applied; 2) converse piezoelectrical effects in which the piezoelectric material is subjected to an external electrical field and will get strained[52]. A representation of the piezoelectric effect is shown in **Figure 3**.

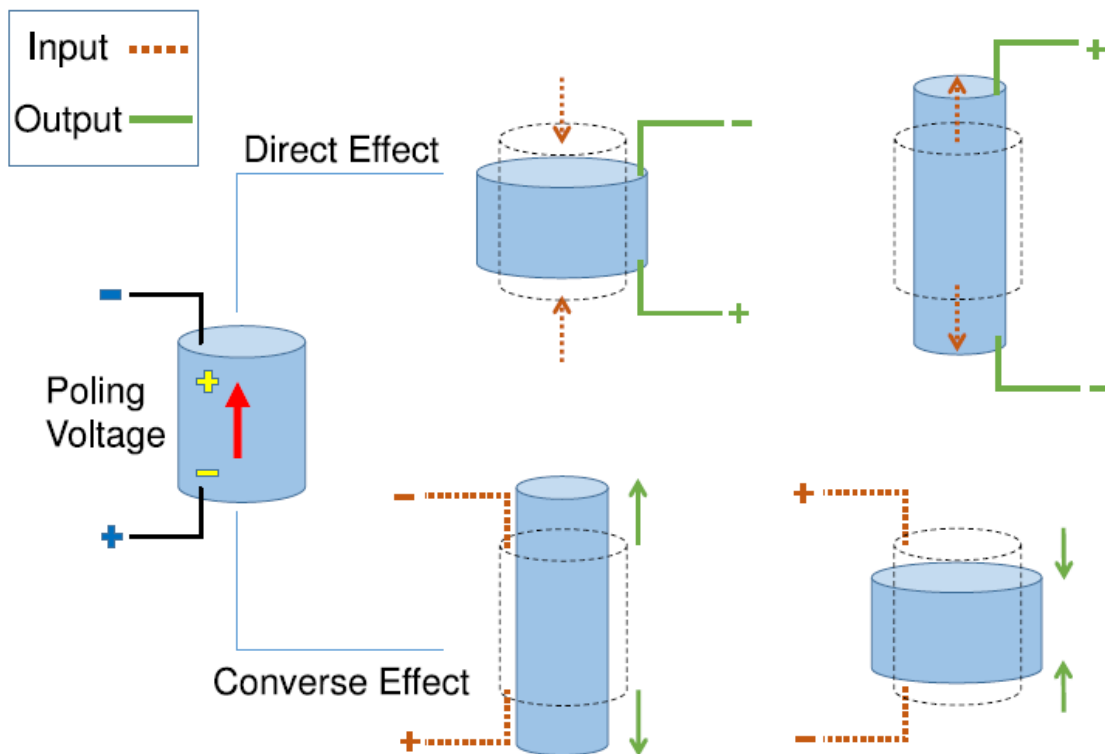


Figure 3. The schematic representation of the piezoelectric effect, in which it is possible to observe the direct effect where mechanical strain generates an electrical output, and the inverse piezoelectric effect where an electrical field generates mechanical strain on the material [53].

The piezoelectric effect occurs because at a molecular level, the negative and positive charges of each molecule within the material coincide [54]. This will cause the material to be electrically neutral. However, by applying an external force to the material, it is possible to deform the internal reticular causing the separation of positive and negative charges of the molecule, thus creating dipoles. The opposing facing charges of the dipoles will cancel each other causing fixed charges to appear on the material edges and resulting in polarization (**Figure 4**)[54].

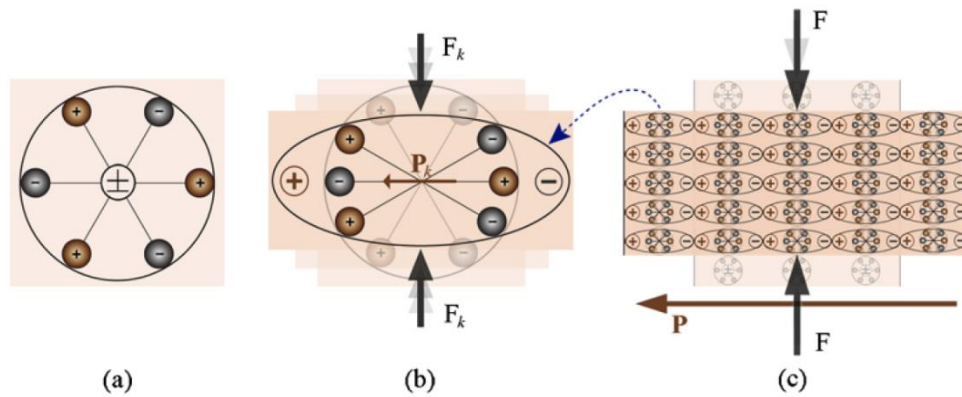


Figure 4. Schematic representation of the dipoles reorientation when subjected to mechanical stress, this reorientation will generate charges on the surface of the material [54]

To calculate the resulting polarization (P) that is dependent on the magnitude of the stress (σ) applied to the material and the material dielectric constant, this relationship of dependence is presented in **Equation 1**. It is also possible to calculate the strain (x) in the converse piezoelectric effect since it is related to the strength of the applied electrical field (E), **Equation 2**. These parameters are also dependent on the piezoelectric constant of the material (d_{ij})[55]

$$P = d_{ij} * \sigma \quad (1) \quad \text{Eq.1}$$

$$x = d_{ij}E \quad (2) \quad \text{Eq.2}$$

The piezoelectric constant represented by d_{ij} is a ratio of the strain in the j axis when the external stresses are constant, i and j represent a coordinate system that can take values between 1 and 6 with 1,2 and 3 representing the x , y and z axis respectively and 4,5 and 6 representing shear around the x , y and z axis respectively (**Figure 5**)[56].

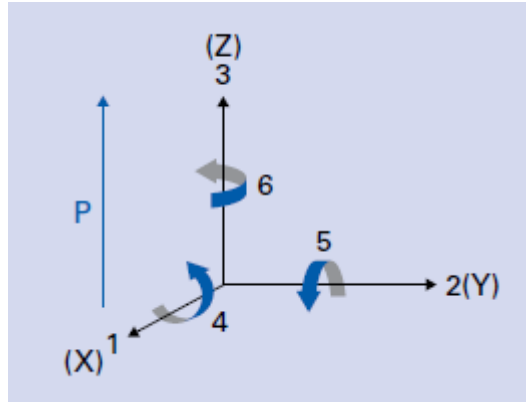


Figure 5. Representation of the axis system used to describe the piezoelectric constant where 1,2 and 3 correspond to the x, y and z axis respectively and 4,5 and 6 representing shear around the x, y and z axis respectively[57].

The human bone also displays piezoelectric properties as it was discovered by Fukada et al. in 1957[6]. It was posteriorly found that the piezoelectric properties of the bone are conferred by collagen, which is a major constituent of the organic part of the ECM[14], [58]. It is thought that the bone piezoelectricity plays a vital role in the regulation of bone remodeling, as the signals generated by the collagen will then be transmitted through the ECM to the voltage-gated channels in the cell membrane of osteocytes. The activation of these channels will act as a signal and trigger events like matrix production, cell growth, and tissue repair[8,14]. This property of the bone can be exploited to improve osteogenesis in implants[8].

Besides the bone, piezoelectricity can be found in other biological materials such as wood and fibrous proteins like collagen, chitin, and elastin, there are several piezoelectric materials with potential applications in hard tissue engineering, which include ceramics and polymers[14].

Even though there are a lot of piezoelectric ceramic materials and many of them cannot be considered for biomedical applications due to potential cytotoxicity, such as ceramics containing lead, there are some ceramics that are adequate for use in hard tissue engineering. The examples are barium titanate, which is a biocompatible ceramic with a d_{33} coefficient of about 191pC/N and when in nano particles form it supports cell attachment and proliferation of osteoblasts and osteocytes. Potassium sodium niobate has a piezoelectric coefficient of 63 pC/N and it has been reported to improve bone and cartilage regeneration.[14]

Biopolymers are also becoming more prominent in tissue engineering due to their biodegradability and low toxicity. In addition to that, the polymers also show good

biocompatibility, biological signaling, cell adhesion, and biodegradability. However polymers suffer from low piezoelectric coefficients with values ranging between 0.2 and 2 pC/N and do not provide adequate physical and mechanical properties.[14] .The processing of polymer can also present a problem since it is possible to lose biological properties during the process.[14]

There are piezoelectric biopolymers with strong potential use for hard tissue engineering: poly (vinylidene fluoride) (PVDF), poly-3-hydroxybutyrate-3-hydroxy valerate (PHBV) and poly-L-lactic acid (PLLA).

PVDF shows a piezoelectric coefficient of about 20 pC/N and is non-toxic. It can also be used in a copolymer of vinylidene fluoride (VDF) with trifluoroethylene (TrFE), which presents the highest piezoelectric coefficient found in polymers of 30 pC/N. PVDF can promote osteogenic differentiation, and P(VDF-TrFE) has shown the ability to regenerate bone, cartilage, and tendon. However, these polymers show high chemical and physical resistance, which cause a low degradation rate that is not adequate to biological environments. The fact that PVDF family polymers are non-biodegradable can present a barrier to its use in hard tissue engineering.[12,14,59]

PHBV has a piezoelectric coefficient of 1.3pc/N, which is similar to that of the bone and is both biocompatible and biodegradable. However, even though it has been used for bone and cartilage tissue engineering, the effect of its piezoelectric properties in the regeneration of hard tissues has not been shown yet.[14,60]

PLLA is a bioactive and biodegradable polymer with a piezoelectric constant d_{14} of about 30pC/N, and it has been shown to promote bone tissue growth[14].

2.5. Poly (L-Lactic Acid)

Poly(lactic acid (PLA) is an aliphatic polyester that has thermoplastic behavior. PLA is obtained from lactic acid or lactide and this is the reason why PLA is biodegradable and non-toxic, since its hydrolysis originates lactic acid which is naturally present in the body [61]. Since lactic acid and lactide are both chiral they exist in different enantiomers, shown in **Figure 4**, this allows PLA to exist in 3 stereoisomers: poly (L-lactic acid) (PLLA) and poly (D-lactic acid) (PDLA) which are both optically active and semi-crystalline and poly (D,L-lactic acid) (PDLLA) which is optically inactive and amorphous. PLA is a versatile polymer since its properties may vary with its molecular weight and degree of crystallinity

which allows to tune its properties to a specific use. The degradation of the PLA chain by hydrolysis is also influenced by its molecular weight, crystallinity, morphology, and hydrophilicity. Amorphous PLA such as PDLA has a faster degradation rate while PLLA and PDLA are semi-crystalline which causes them to have a slower degradation rate where PDLA degrades faster than PLLA[62-64].

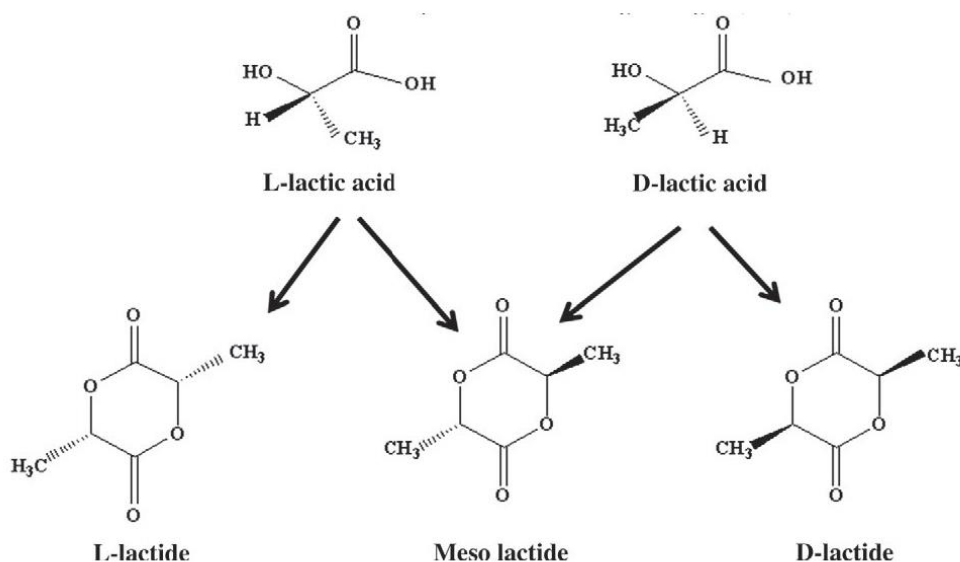


Figure 6. Possible enantiomer for lactic acid and lactide[63]

PLLA has been widely used in the biomedical field due to its biocompatibility, biodegradability, thermal plasticity, and mechanical properties [9,65]. The interest in PLLA also comes from the fact that it is approved by the U.S. Food and Drug Administration (FDA) for use in bone implants screws, fixation pins, and sutures[6,13]. Another attractive property of PLLA with potential application in tissue engineering is its piezoelectric activity. A piezoelectric implant would be advantageous since it could act as a charge generator inside the bone, using the mechanical stress generated during the body movement (direct piezoelectric effect) and subsequently improving the bone tissue regeneration[7].

The origin of the piezoelectricity in PLLA comes from its C=O dipoles, which are able to rotate when shear stress is applied, thus causing electrical polarization and the appearance of surface charges [10]. The piezoelectric effect in PLLA comes from the crystalline and highly oriented regions of PLLA, however its magnitude is dependent on many factors such as degree of crystallinity, degree of orientation and glass transition temperature of the amorphous zones[66,67]. PLLA has a piezoelectric coefficient (d_{14}) of

about 30 pC/N[68].

In 1996, Fukada et al[68] studied the use of PLLA as a material in bone implants and the effect of piezoelectricity in the bone regeneration by inserting a PLLA rod with 5 mm of diameter as an intramedullary pin into several cats' tibias. It was possible to observe that PLLA has a significant effect on the promotion of callus formation and those of PLLA rods with better piezoelectric properties demonstrated increased the amount of formed callus.

2.5.1. Poly (L-Lactic Acid) Crystallinity

One factor of significant impact to the properties of PLLA is the degree of crystallinity since it determines mechanical and physical properties such as electromechanical (piezoelectric) response, biological response and hydrolytic degradation(the amorphous regions degrade faster)[69,70]. PLLA is a polymer with low crystallization kinetics, which makes it easy to prepare with different degrees of crystallinity. However it is hard to achieve a crystallinity degree of over 60% that means the amorphous phase will also play a significant role in the final properties of the polymer. This factor is especially important in biomedical application since PLLA has a glass transition temperature of 60-65°C, which is not that much higher than physiological temperatures[69].

PLLA shows crystal polymorphism with three main crystal forms α , β and γ [71]. The α form usually comes from melt or cold crystallization or solutions. The α form has two antiparallel chains in a helix conformation packed in an orthorhombic unit cell (**Figure 7.**) [71,72]. The β form usually forms when hot drawing melt or solution spun PLLA fibers at a high temperature and a high draw ratio [71,72] . This form consists of three helix chains packed in a trigonal unit cell (**Figure 7.**). The γ form occurs via epitaxial crystallization of the PLLA on a hexamethylbenzene substrate [71,72] . It is composed of two antiparallel helices packed in an orthorhombic unit cell

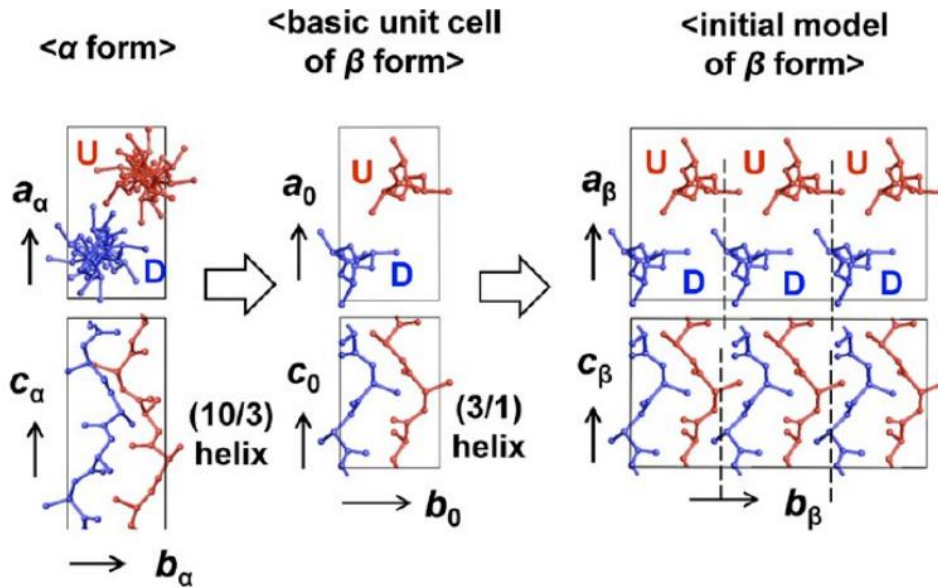


Figure 7. Proposed model to the α and β forms of PLLA[73].

Besides those three main forms, there is also the α' form which consists of a modification of the α form [68]. Both of these forms have a similar packing sharing the helix conformation, which in the α' is disordered and has slightly larger lattice dimensions. The α' form is usually favored at lower temperatures and since the α' is less stable than the α form, it usually transforms to α form when heated at high temperatures. Besides the conversion from α form to α' form, the interconversion between the various other crystal forms of PLLA is also possible.[70-72,74]

As it was demonstrated previously in work devoted to the same scientific direction [23], in FTIR data of alpha PLLA, the C=O stretching region can be split into four peaks due to intramolecular and intermolecular interactions within the four possible conformations of PLLA chains. These conformations depend on the rotation angle between PLLA's skeletal bonds and are gg, tg, gt, and tt which correspond to 41, 51, 103 and 21 helices, where t and g stand for trans and gauche respectively. The peak at 1755 cm^{-1} corresponds to the gt conformation. It can be deduced that in solvent cast PLLA films, the gt conformation is the one preferred to constitute the crystal structure. This conformation has the lowest energy among the four conformations and is thermodynamically the one forming in solvent cast films. The other prominent peak is relative to the tt conformation (1745.5 cm^{-1}) that does not contribute to the crystallization

When crystallized from high viscous solutions or melt, PLLA can form spherulites

which are spherical symmetric crystal colonies[75]. Spherulites are composed by both the crystalline, amorphous, and rigid amorphous phases of PLLA[75]. When looking at spherulites with magnification, it is possible to observe that they are composed of radially directed fibrils composed by one or more lathlike or ribbonlike crystals elongated in the growth direction [75,76]. When observed under polarized light, it is possible to detect a dark Maltese cross pattern on the spherulite ⁷¹, this can be seen in **Figure 8**.

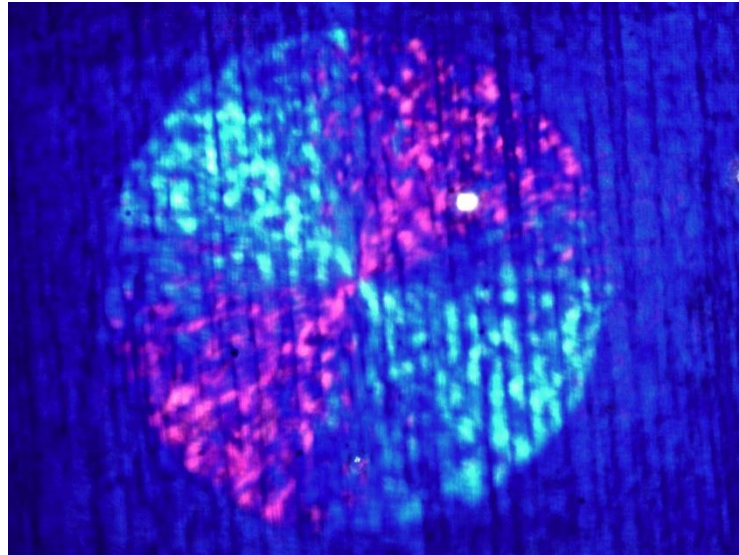


Figure 8. Maltese cross pattern observed in a spherulite viewed under polarized light using a optical microscope.

The formation of spherulites starts with the primary nucleation that occurs via homogeneous nucleation in which in a PLLA melt or solution where small crystal embryos will spontaneously form and disappear[70] . Until an embryo of different shaped or large enough (critical nucleus) will appear to which the addition of a single molecule that can cause a decrease in the free energy of the structure that will allow the positive energy of the crystal to outweigh the negative driving force of crystallization, thus allowing spherulites to grow [70,75]. Homogeneous crystallization, however, is very rare so the most common form of primary nucleation is by heterogeneous nucleation in which the crystal stars forming in solid impurities[67], This will provide a surface on which nucleation can occur faster since the impurity will lower the surface energy and result in a reduced size for critical nucleus. The spherulites will then start to grow by secondary nucleation in which PLLA strands will deposit on the crystals created during primary nucleation, causing them to grow. The strands will bond to the crystals and start to branch. Since it is more energy efficient to create an isolated strand than creating secondary branches, most of the molecules will create

secondary intermolecular bonds with the substrate [71]. The main strands will then bond laterally. The spherulites can then grow until they collide with another spherulite. The crystallization kinetics and morphology of the spherulites can be affected by several factors such as molecular mass of the PLLA, thickness of the film, method of casting the film, crystallization temperature and time [70,75,76].

The thickness of the film is an essential parameter since PLLA usually shows a different morphology of crystals and spherulites when crystallized in a nanoscale confined system compared to when crystallized in bulk. Usually, when the thickness is much larger than 100 nm there will be the formation of regular spherulites similar to the ones formed in bulk. In films with a thickness smaller than 100 nm it is possible to observe different crystalline morphologies. In polymers like poly(3-hydroxybutyrate) (PHB) having a substrate on top can also influence crystallization since PHB exposed to air would promote to grow non-banded spherulites, while when covered with a glass slide or removed moisture, the spherulites would become banded [75] with similar effect observed in PLLA/Polyethylene Oxide (PEO) blends [77]. Molecular weight can also be a factor that leads to cracks on the spherulites [75,76,78].

Overall crystallization of PLLA is a very variable process in which a lot of parameters can interfere in the final result. Some factors that have not been mentioned include the crystallization temperature, crystallization time and the cooling rate [75,79-81]. Besides those factors, it is also possible to improve the crystallization process by utilizing nucleating agents such as graphene oxide[81] or talc[82].

2.6. Polymer-Metal Interface

While metals may sometimes present the desired biocompatibility many times, they lack the ability to stimulate bone growth. This can be improved by coating the metal using a polymeric coating. In order to have success in biomedical applications, it is essential for the adhesion between metal and polymeric layers to be strong and reliable[83,84].

ASTM standard ASTM D907- Standard Terminology of Adhesives[85] defines adhesion as “the state in which two surfaces are held together by interfacial forces which may consist of valence forces or interlocking forces or both”. Adhesion can occur through different mechanisms, which may be mechanical, chemical, or physical in nature.

Mechanical adhesion occurs through mechanical interlocking in which the adhesion

is the keying of the adhesive in the pores and irregularities of the surface. The adhesion by mechanical interlocking can be improved by increasing the roughness of the surfaces to allow for more anchoring points[83,86]. According to Venables[87] mechanical interlocking is of great importance to have a strong and lasting bond between metal and polymer.

Chemical adhesion is when two surfaces that are in close contact and form a chemical bond between their compatible chemical groups. Those bonds can be either primary bonds such as covalent, metallic, or ionic bonds which should be the leading force in joining the materials[79,82] . However, secondary bonds such as dipole-dipole interactions or van der Waals forces should also contribute to the overall strength of the adhesion.[83,86]

Physical adhesion can occur through either adsorption or electrical attraction. The thermodynamic model of the adsorption adhesion is based on the fact that in a neutral environment like air, the thermodynamics of the polymer system will have the tendency to minimize the surface free energy by orienting the surface into the polymer's non-polar region and that when the polymer is in contact with a polar substance, the interfacial tension should be minimized in order to achieve strong adhesion [83,86]. According to the adsorption theory, an adhesive must be able to wet the surface of the material to which it will adhere. The adhesion should occur due to interatomic and intermolecular forces, which will form at the interface if an intimate contact is achieved. This contact requires that the adhesive spreads over the surface of the adherent, which will happen when the substrate has a high enough surface energy, and the liquid has a low enough surface energy. In the electrostatic theory, adhesion occurs because an electrostatically charged double layer of ions will form in the interface generating Coulomb attraction forces between net charges[83,86].

To have a successful adhesion, the surface energy of the surfaces should be similar. However, most synthetic polymers have low surface energy while metals have a high surface energy[88]. For this reason, the coating of metals with polymers presents a challenge since there are significant differences not only in the surface difference but also in physicochemical and structural properties between polymers and metals [16,17] . These include differences in thermal expansions coefficient and wettability. The interaction between polymer and metal will also be highly dependent of the chemical groups present in either the metal or the polymer. Adhesion between the polymer and metal can happen through chemical bonding and mechanical bonding such as anchoring or interlocking. However, the difference in properties causes the binding between metals to constitute of

weak Van der Waals force, which finally can lead to peeling[16,17,88]. This can be overcome by modifying the metallic substrate surface by adding chemical groups or changes in the surface topography[15]. Some of these methods include UV irradiation of the metallic substrate[21], corona treatment[78], plasma functionalization, and etching[16], oxidation of the metal[88] or by the use of coupling agents, such as silanes[86] or polydopamine[20].

Chapter 3 – Materials and Methods

Chapter 3 – MATERIALS AND METHODS

In this chapter the experimental procedures, materials and characterization methods used in this work are described. First the stainless-steel substrates were subjected to one of two pre-treatments before silanization, those pre-treatments consisted of either thermal treatment in which the substrate was thermally treated at 500°C for 2 hours, or UV treatment in which the sample was submitted to UV irradiation for 2 hours. Some of the substrates were then subjected to the process of silanization using a 1% APTES solution in toluene. Substrates both pristine, pre-treated and silanized were characterized using different methods, which include, Fourier Transformed Infrared Spectroscopy (FTIR), Optical Microscopy, Scanning Electron Microscopy (SEM), Atomic Force Microscopy (AFM) and Contact Angle analysis.

After the treatment of the substrates a PLLA film was deposited on them via spin coating of a PLLA solution in 1,4 dioxane, with concentration of 2.5 wight percentage (wt.%) or 5.0 wt.%. PLLA films of both concentrations were analysed using Differential Scanning Calorimetry (DSC). The PLLA films on the different substrates were subjected to crystallization treatments done either on a thermal plate or in a Linkam stage, varying parameters such as the cooling rate, solution concentration or crystallization temperature. The samples with crystalline PLLA films were characterized using different methods, FTIR, Optical Microscopy, SEM, AFM; X-Ray Diffraction (XRD). The adhesion of these films to the substrate was tested using the crosshatch tape-test methods.

The effect of polarization in these films was also tested to use in future cellular tests.

In order to verify the bioactivity of the PLLA films Simulated Body Fluid (SBF) tests were performed for a period of 3,7, 14 and 28 days.

A scheme of the processes is represented in **Figure 9**. below

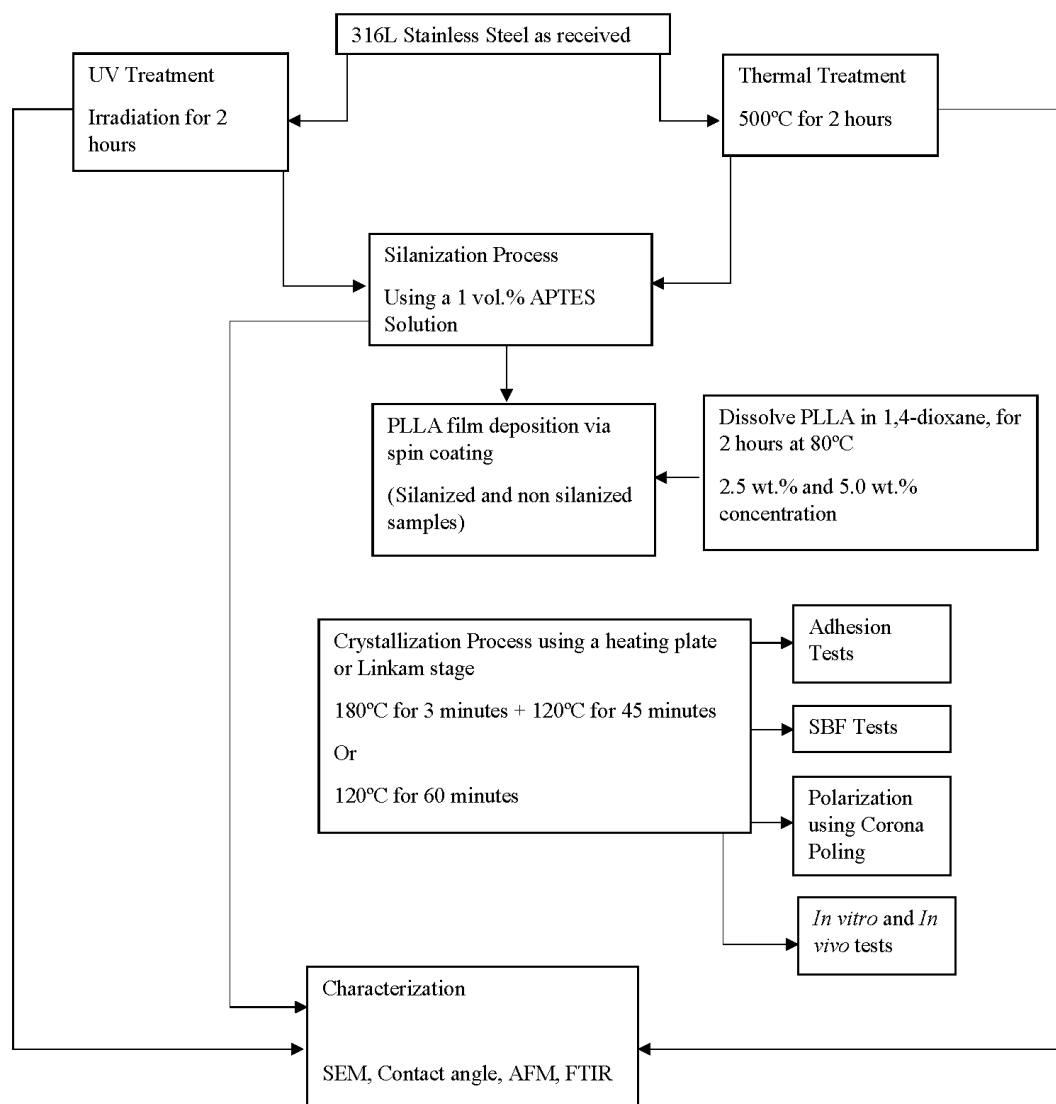


Figure 9. Schematic representation of the work done during this thesis.

3.1. Materials

To prepare the platforms that were studied during this work the following materials were used i) the substrates FE240310 Stainless Steel – AISI 316 Fe/Cr18/Ni10/Mo3 (Goodfellow Cambridge Limited); ii) the films of Poly (L-lactic acid) from Purasorb® PL 38, Purac, The Netherlands and iii) to functionalize the substrate surface (3-Aminopropyl)trimethoxysilane 97% (APTES, Aldrich) was used.

1,4-Dioxane anhydrous 99.8% (Sigma-Aldrich) and Toluol zur analyse C₇H₈ (Merck) were used to dissolve the PLLA pellets and the APTES, respectively. The tape tests were performed with an Elcometer 99 adhesive tape.

To prepare the SBF the following reagents were used: Sodium Chloride 99.5% (Pronalab), Sodium Hydrogen Carbonate 99.5% (Merck), Potassium Chloride 99.0% (Sigma Aldrich), Potassium Dihydrogen Phosphate 97% (May & Baker), Magnesium Chloride 99% (Riedel-de Haën), Calcium Chloride Hexahydrate 99% (Fluka Analytical), Tris(hydroxymethyl) aminomethane 99.5% (Merck) and Hydrochloric Acid 12M (Sigma Aldrich).

3.2.Methods

3.2.1. Preparation of Stainless Steel

To prepare the SS316L substrates, the Stainless Steel AISI 316 Fe/Cr18/Ni10/Mo3 from Goodfellow Cambridge Limited was used. This stainless steel comes in (100 x 100 x 0.38) mm³ plates that were then submitted to laser cutting to obtain squares with the dimension of (10 x 10 x 0.38) mm³. The cut substrates will be from now on referred to as 316L SS. To prepare the 316L SS substrates those are first cleaned by sonication in acetone for 3 periods of 5 minutes, replacing the acetone after each time.

3.2.2. Surface Functionalization

Since the adhesion between the 316L SS substrate and the PLLA is weak, due to the differences in physicochemical properties[16], there is the need to improve it. This can be done by functionalizing the surface of the metal[15]. In this thesis work, the method chosen to functionalize the surface was silanization, which consists of using organosilanes as a coupling agent between the 316L SS substrates and the PLLA.

In this work, the silanization process was done using 3-Aminopropyltriethoxysilane (APTES) that is an alkoxy silane with the chemical formula C₉H₂₃NO₃Si. These molecules have three ethoxy groups which have the ability of binding to steel and on terminal amine group that can bind to PLLA[89-91].

The process of silanization starts with using a solvent to hydrolyse the ethoxy groups which will form reactive silanol groups that can bind to the hydroxyl groups (-OH) present on the metal surface forming the chemical bond Si-O-M between the silane and the metal and Si-O-Si bonds between the APTES molecules[92,93] as seen in **Figure 10**.

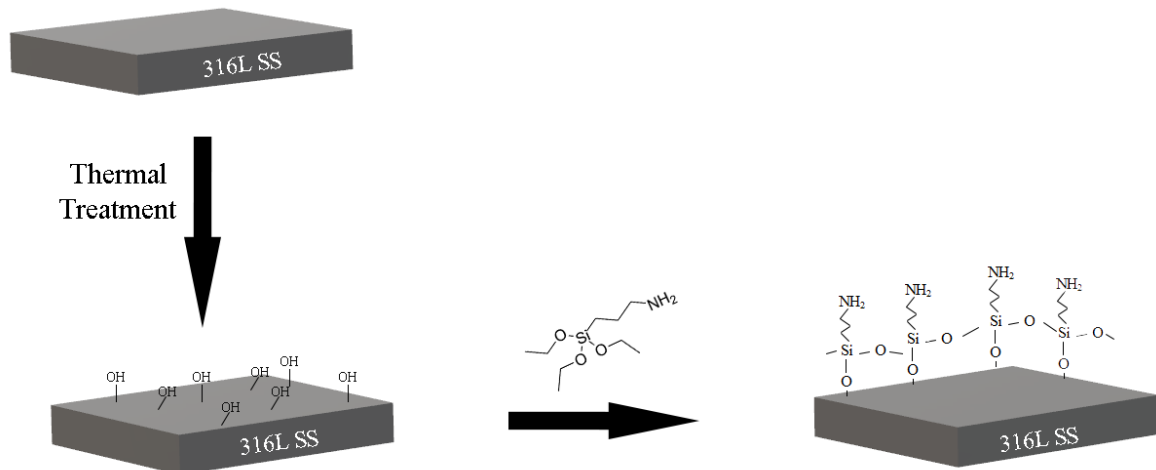


Figure 10. Schematic representation of the silanization process.

For this reason, the concentration of OH groups on the surface of the metal is of crucial importance for the success of the silanization. The low concentrations of OH groups on the surface lead to weakly bound clusters of silanes, while the high concentration of OH groups leads to a monolayer of silanes with a high degree of bonding[93]. It is possible to increase the concentration of OH groups by subjecting the 316SS substrates to thermal treatments[94] or UV irradiation[95].

In order to increase the concentration of hydroxyl groups and to maximize the adhesion strength between substrates and PLLA the substrates were pre-treated with 2 different processes.

3.2.2.1. Thermal treatment

The cleaned substrates were placed in ceramic boats and subjected to a thermal treatment in an oven (Termolab, Fornos Elétricos) for 500°C for two hours, using a heating rate of 5° C/min and a cooling rate of 10° C/min. A representation of the thermal schedule used can be seen in **Figure 11**.

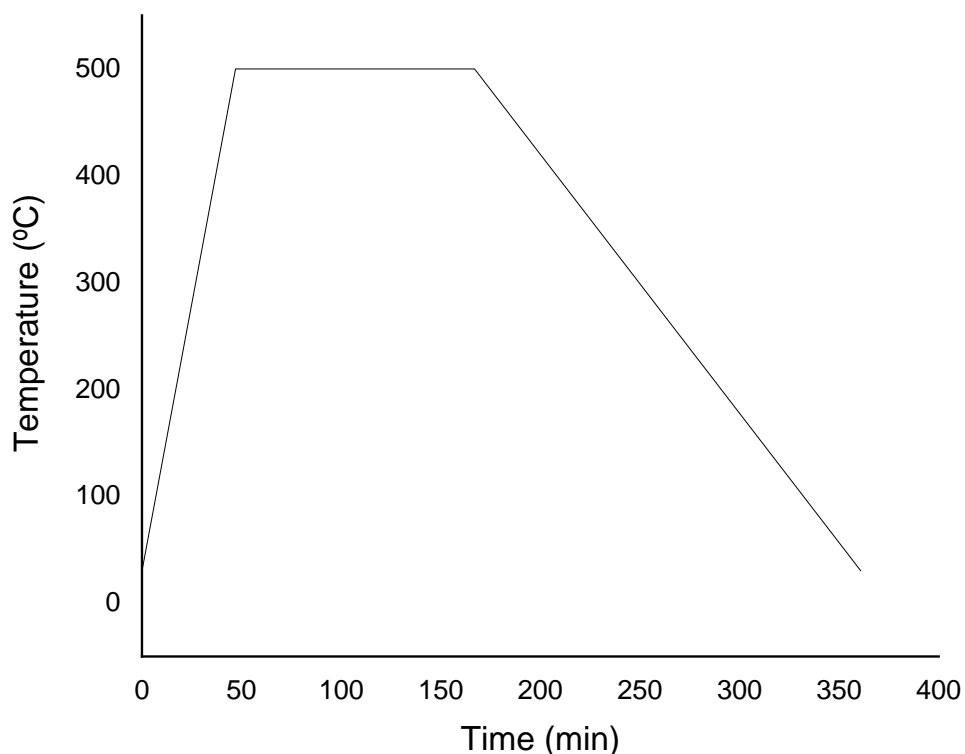


Figure 11. Thermal schedule used in the thermal treatment of the 316L SS substrates.

3.2.2.2. UV irradiation

The cleaned substrates were placed in a UV cleaner (Novascan PSD-UV 4, Novascan Technologies inc.) and were irradiated with UV light at wavelengths of 185 and 254 nm for two hours. The wavelength of 185 nm produces ozone in the presence of oxygen while the 254 nm wavelength excites organic molecules on the surface[96].

3.2.3. Silanization process

For the silanization process, a 1 vol% solution of APTES was prepared using toluene as the solvent. The pre-treated samples were then left to soak in the solution for one hour in a covered petri dish with the hood fumes turned on. After one hour, the samples were rinsed one time with toluene and then one time with ethanol. Following this, the samples were dried with an air gun followed by 10 minutes in the oven at 100°C.

3.3. PLLA solution preparation

PLLA solutions of concentration 2.5 wt% and 5.0 wt% were prepared. These concentrations were used in order to match the ones used in previous work and developed in the work of group [22]. The solutions were prepared by dissolving the PLLA pellets with a molecular weight of 650000 g/mol in 1,4-dioxane, in a round bottom flask. The solution was prepared using a thermal stirrer plate (IKA C-MAG HS 7, IKA-Werke), with the solution under constant stirring in a silicone bath at 80°C. The temperature was controlled using a thermocouple (IKA ETS-D5, IKA Werke). The setup used to prepare the solution can be seen in **Figure 12**



Figure 12. Setup of the equipment used in preparation of the PLLA solution.

The temperature of 80° C was chosen to be above the glass transition temperature of PLLA[23] to improve the crosslinking between PLLA and dioxane[22]. The solution was then stored in a desiccator at room temperature in dark condition.

3.4. PLLA film deposition

PLLA films were obtained by spin coating, which is a method that allows the production of uniform thin films. However the final film thickness can be affected by several parameters, including the dispensed volume, the solution viscosity, and concentration, and the duration and speed of the spin [97].

The process of spin coating can be divided in 4 main phases.

First, there is the fluid deposition, in which the solution will be deposited on the substrate surface. In this work static dispense was used in which a drop of the solution is deposited in the centre of a static substrate (**Figure 13. i.**). The volume used will depend on the fluid's viscosity and substrate volume. It is also possible to do a dynamic deposition in which the substrate is rotating at low speeds.

The second step is substrate acceleration or spin up in which the substrate will be accelerated to the desired rotation speed. During this phase, a heavy expulsion of solution will occur until the fluid is thin enough that it co-rotates with the substrate, has uniform thickness and has covered the whole substrate (**Figure 13. ii.**). This process is influenced by the rotation speed that can range from 1500-6000 rpm and the rotation time that can go from 10 seconds to several minutes.

The third phase is the fluid outflow in which gradual fluid thinning occurs dominated by fluid viscous forces. It is possible to observe edge effects due to the fluid flowing outward but needing to form droplets to flung off (**Figure 13 iii.**). For this reason and depending on the surface tension, viscosity and rotation rate, this phenomenon may cause the film thickness to be slightly different around the edges.

Finally, the last phase is the evaporation phase. As the fluid outflow progresses, the fluid will reach a thickness in which the effect of the viscous force will be very small and the evaporation of the solvent starts to be the leading cause of the thinning (**Figure 13. iv.**).[97,98]

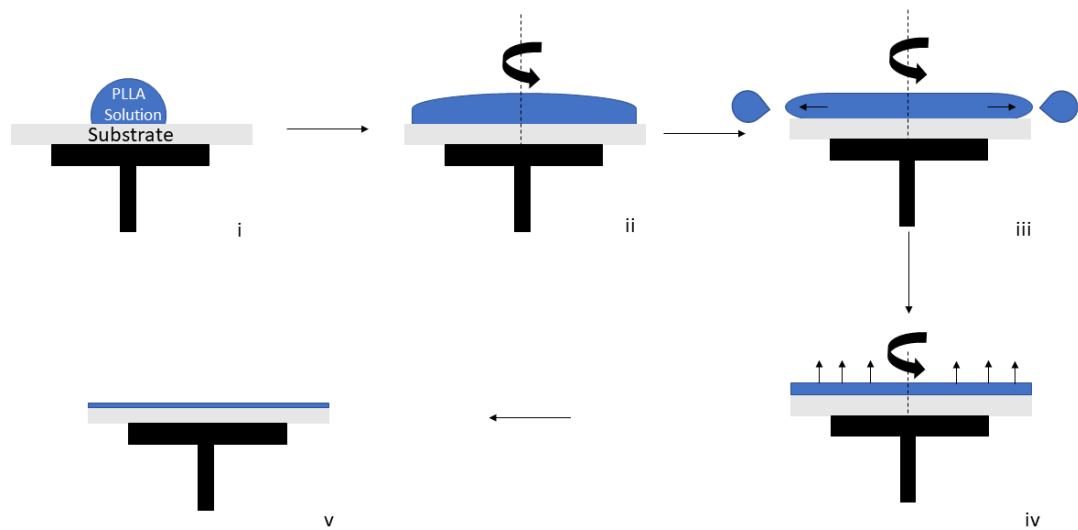


Figure 13. Schematic representation of the spin coating process. i) Fluid deposition; ii). Substrate acceleration; iii) Fluid outflow; iv) Evaporation phase; v) Final film. Based on [99]

In this work, 316L SS substrates were coated using a Chemat Technology, Inc. Spin Coater KW-4^a. The PLLA solution droplets had a volume of approximately 0.5 μl , and the substrate was then spun at 3500 rpm for 30 seconds. This process was repeated until 3 layers of the PLLA solution were deposited. Although the different solution concentrations had different viscosities, the same parameters were used for both of them. In previous works developed within this theme films prepared using this method presented a thickness of 2.0 μm when prepared with the 2.5 wt.% PLLA solution and a thickness of 4.0 μm when prepared with the 5.0 wt.% solution[22].

3.5. PLLA film crystallization

To crystallize the PLLA films two different thermal schedules were used in order to obtain different degrees of crystallinity. To obtain semi-crystalline films, the PLLA films were subjected to a temperature of 120° C for 60 minutes (**Figure 14 i**), the heating rate used was of 5°C/min with different cooling rates (2.5, 5.0 and 10° C/min) in order to achieve different crystallinity degrees and study the cooling rate degree influence on the crystallinity of the films. To obtain crystalline films, the PLLA films were subjected to a 180° C

temperature for 3 minutes followed by 45 minutes at a temperature of 120° C (**Figure 14 ii**), the heating rate used was of 5° C with different cooling rates (0.5, 2.5, 5.0 ,10.0 and 20° C/min).

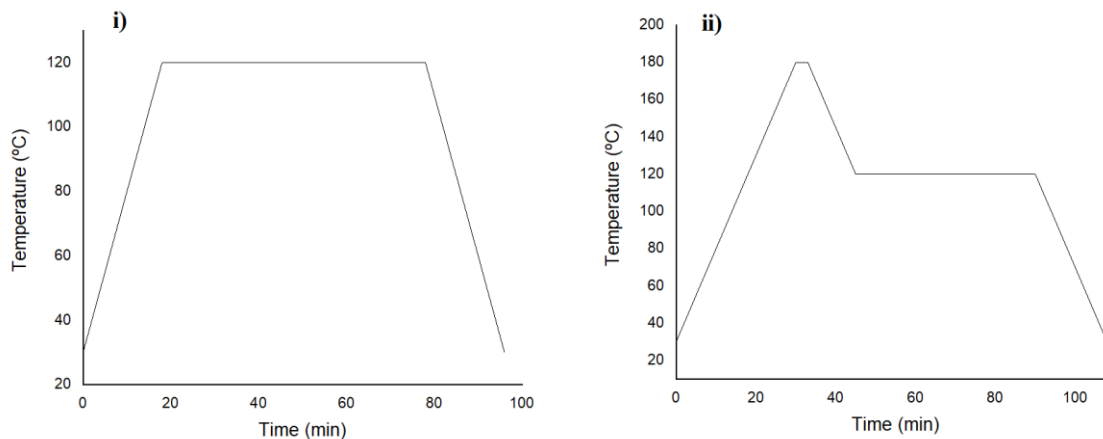


Figure 14. Thermal schedules used in the crystallization of PLLA: 120° C for 60 minutes (i) and 180° C for 3 minutes followed by 45 minutes at 120° C

The temperature of 120° C was chosen since in order to achieve crystallinity the sample must be at above the glass transition temperature[100], and the temperature of 180°C was chosen since it is above the melting temperature, which is around 173 to 178°C[99] , this improves the crystallization of the films since being above T_m promotes the formation of nuclei[100].

The samples were crystallized using two different types of equipment, in order to determine the effect of open and closed environment on the degree of crystallinity. Films were crystallized using open thermal plate (IKA C-MAG HS 7, IKA-Werke) where the control of the heating and cooling rate was done manually and using closed Linkam stage (Linkam Scientific Instruments) which allows for programmed precise control of the cooling and heating rate.

3.6.PLLA film polarization

Each monomer of the PLLA chain has a carbonyl group which originates an electric dipole. Through the process of poling, it is possible to rotate the dipoles reorienting them

and aligning them uniaxially[101]. Corona poling is a technique commonly used to create oriented dipole alignment in thin films[102].

During the process a corona discharge generates ions that bombard the surface thus creating a high surface electric potential and aligning the molecules. The ions do not penetrate into the sample, but they transfer their charge to the surface., During this process the dipoles are oriented along the direction of the electric field[102-104]. This process presents advantages such as being able to be performed without deposited electrodes or only one bottom electrode and allowing application of high voltage poling fields to polarize thin films (despite their defects the destructive breakdown is non-existent or limited to small areas) [103].

Poling the PLLA has been previously shown to improve the adsorption of adhesion-promoting proteins[105]. This can improve the tissue regeneration process since the adsorption of proteins is one of the first phases of the healing process after implantation[105]. The polarization of PLLA is not permanent and the decay depends on the present crystalline forms, α or α' . The α form being able to retain the polarization for longer due to the fact that it has more densely packed chains and less chain mobility [106] . The temperature at which the poling is done also affects the retention time. Temperature above the glass transition temperature allowing for more stable and lasting polarized regions [106] . For example α form PLLA polarized at above glass transition temperature can retain its polarization for up to 10 days[106].

The samples were polarized in a lab-made device which can be seen in **Figure15**. The device consists of a corona chamber made of brass which also doubles as a Faraday cage, a tip to generate the discharge, sample holder, a PT100 temperature sensor, a temperature controller, a high voltage source and a picoamperimeter to measure the current in the sample[107] The samples were first heated to 80°C, which is above the PLLA glass transition, then an electric field of up to -5kV was applied for 30 minutes, the heating was then turned off while the electric field remained on during the cooling process in order to improve the retention of the polarization.

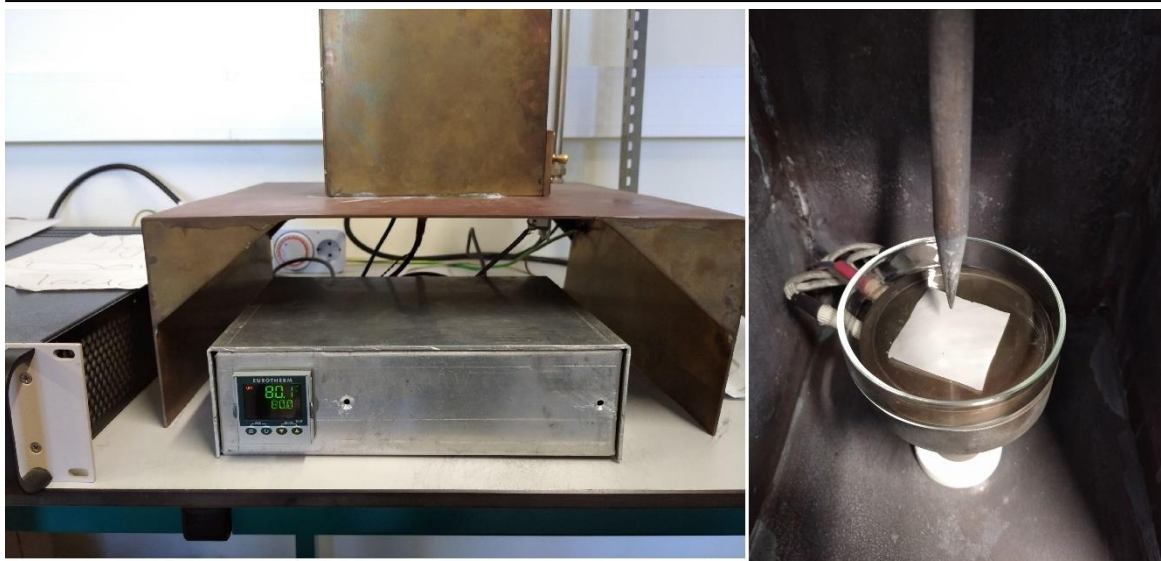


Figure 15. Pictures of the exterior of the lab made corona polling device that was used to polarize the samples (left) and of its interior (right).

3.7.Characterization methods

3.7.1. Fourier Transform Infrared Spectroscopy

Fourier Transform Infrared (FTIR) Spectroscopy is a technique that allows for the determination of the chemical groups present in a sample and can be used for both quantitatively and qualitatively analysis[108]. FTIR is an infrared spectroscopy technique that is based on the fact that the atoms in molecules undergo vibrations such as stretching and bending. When infrared (IR) radiation interacts with those vibrating atoms and molecules they constitute a part of that radiation with the same frequency as the vibration frequency of the atoms while transmitting the rest. This allows to identify of the different chemical groups present in the sample. FTIR takes this process and then uses computer software to apply a Fourier transformation to convert the obtained interferogram into a spectrum. This technique presents advantages such as being able to be performed in real-time and being non-destructive[109,110].

A Tensor 27 IR (Bruker) was used in this work to perform a chemical analysis of the stainless-steel substrates in different phases of the process: pristine, after the different pre-treatments, after silanization, as well as SS316L/PLLA samples.

3.7.2. Optical microscopy

In order to characterize the samples' surface optical microscopy was used. To that purpose two different equipments were used a stereo microscope (Leica EZ4HD) and a optical microscope capable of polarized optical microscopy (Nikon Microphot)

3.7.3. Scanning Electron Microscopy

The surface topography of the substrates at the different phases and PLLA films was analysed by Scanning Electron Microscopy (SEM), which is . the most widely used form of electron microscopy.

The SEM image is obtained by striking the sample with a focused electron beam that scans over the surface of the sample. When the electron beam interacts with the sample, it causes scattering of electrons, which can be either elastic or inelastic. Elastic scattering causes the incident electrons to be scattered by the specimen (backscattered electrons) while inelastic scattering causes electrons to be ejected from the atoms in the sample (secondary electrons). Secondary electrons are the main signal to obtain topographic contrast and backscattered electrons to obtain compositional contrast. The scattered electrons will then be collected by a detector to subsequently generate the final image. Before analysing the samples, non-conductive samples should be coated with a conductive film. This procedure avoids the accumulation of electrons on the surface of the sample that can lead to surface charging and cause image distortion.

SEM equipment is often coupled with X-ray energy dispersive spectroscopy (EDS), which is a semi-quantitative chemical analysis method based on the radiation of samples with high energy electrons, which will cause the sample to emit X-rays, the energy of the emitted X-rays usually varies from element to element which allows for the detection of the elements present in the sample[111,112] .

The samples analysed in this work were first coated with carbon by vacuum evaporation. The samples were then observed using the SEM equipment Hitachi SU70 using an electron acceleration field of 4 kV or 15 kV.

3.7.4. Atomic Force Microscopy

Atomic force microscopy is an imaging technique that works based on a sample's interaction with the tip of a cantilever (probe). When the tip interacts with the sample, the forces between the tip and the sample will cause the cantilever to deflect. It is possible to relate the deflection of the cantilever with the contact force by using Hooke's Law (**Equation 3**).

$$F = -kz \quad \text{Equation 3.}$$

where F is the force between the sample and tip of the cantilever, k is the spring constant, and z is the deflection of the cantilever.

The deflection of the cantilever is measured by using a laser that will reflect from the backside of the cantilever into a photodetector. Imaging of the sample is done by scanning the sample with the probe while tracking its deflection, a schematic representation of this can be seen in **Figure 16**[113,114].

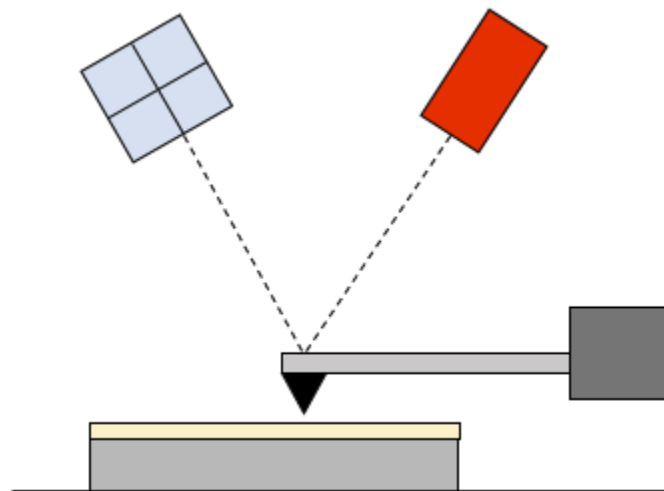


Figure 16. Representation of the AFM technique[23].

Depending on the distance between the probe and the sample, different tip-surface interactions can be measured.. For this reason, different AFM can operate in different imaging modes depending on the distance between the tip and sample, which will influence the type of interactions, where the mainly used imaging modes are contact mode, non-contact, and tapping mode[113,115].

In contact mode the tip is brought to around 0.1 nm of the sample. At this distance the main forces that acts on the tip are repulsive forces which causes the deflection of the cantilever. This mode is mainly used to obtain information about the topography of the

sample; but it may be problematic for delicate samples due to the shear force applied by the cantilever[113,115,116].

In non-contact mode the distance from the tip to the sample is between 10 to 100 nm. At this distance the main forces acting on the tip are attractive forces, which causes the oscillation of the cantilever. When operating in this mode the force gradients are detected by shifts in the cantilever resonance frequency or in amplitude and phase. This mode is also mainly used to obtain information about the sample topography, however, it has the advantage of being away from the samples avoiding possible damages[113,115,116].

Tapping mode works in a similar way to the non-contact mode by detecting the oscillation of the cantilever, however, in this method the amplitude of the oscillation is much larger than in non-contact mode, and the tip is at a smaller distance from the sample. In this mode, both repulsive and attractive forces act over the tip. When the tip touches the sample's surface the oscillation amplitude is reduced by energy loss. This amplitude reduction is then used to measure topographic features, with the amplitude increasing on depressions and decreasing on bumps[115,116].

Piezoresponse force microscopy (PFM) is a functional contact mode technique based on the converse piezoelectric effect. In this technique, a voltage is applied to the tip that causes piezoelectric samples to suffer a strain. The deformation of the sample will then cause the deflection of the cantilever, this is represented in **Figure 17**. When the polarization vector of the piezoelectric sample is perpendicular or parallel to the sample it is possible to measure both vertical electromechanical deformation (out of plane PFM), and lateral electromechanical deformation (in plane PFM).. This allows for the PFM technique to provide information about the polarization orientation of the sample[117,118]

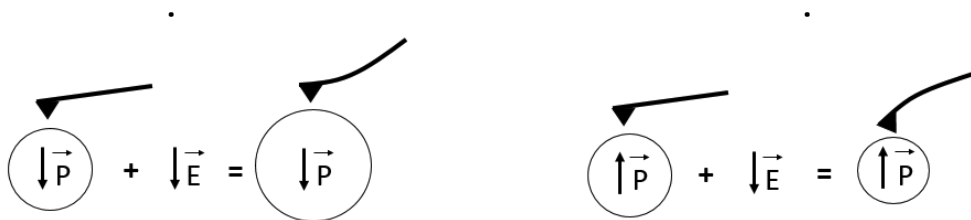


Figure 17. Expansion and contraction of the sample electric domains. Polarization (P) of the piezoelectric domain is (a) parallel and (b) anti-parallel to the applied electric field (E)[23].

In electrostatic force microscopy is a operational mode in which a voltage is applied on the cantilever's tip while the tip oscillates over the surface in two scans, the first scan is

to obtain information about the topography, scanning the sample in non-contact mode while the second scan allows to obtain information about the electric forces gradient, this is done by lifting the tip of the cantilever increasing the tip sample distance until the electrostatic forces are dominant, this allows for the obtention of information about the topography, charge distribution and surface potential of the sample[119].

Kelvin Probe Force Microscopy (KPFM) is a non-contact AFM mode in which similarly to EFM a voltage is applied to the tip of the cantilever. KPFM is performed in two scans over the sample, The first one is performed in tapping mode to obtain information about the topography, during the second scan a alternating current (AC) voltage is applied creating an oscillating electrostatic force between the sample and the tip. Then a direct current (DC) voltage will be applied to nullify the potential and stop the cantilever from oscillating, this current can then be used to calculate the difference in electric potential and as a work function between the tip and the sample. Work function can be defined as the energy needed to remove an electron from the Fermi level in a solid under vacuum[119].

The AFM, PFM and KPFM measurements were done using manufacture AFM microscope (NTMDT NTEGRA Prima). For the piezoresponse mode, the external lock-in system (SR830 Standfort Research) and function generator (FG120 Yokogawa) were used. The piezoresponse signal was measured at frequency of 50 kHz and amplitude range from 1 V to 10 V. The AFM/PFM measurements were acquired by utilizing the Multi75-G AFM probe (Budgetsensors) possessing resonance frequency at 75 kHz and stiffness of 3 N/m.

3.7.5. Contact Angle

By analysing the surface energy and affinity of a liquid towards a solid substrate it is possible to know some of its surface properties, such as its wettability. This can be done by analysing a sample's contact angle of a water drop over the sample. The contact angle allows the understanding of the sample's interaction with the three-phase system (solid/liquid/air) and consists of the angle formed by the intersection of the liquid-vapor and liquid-solid interface (**Figure 18.**).

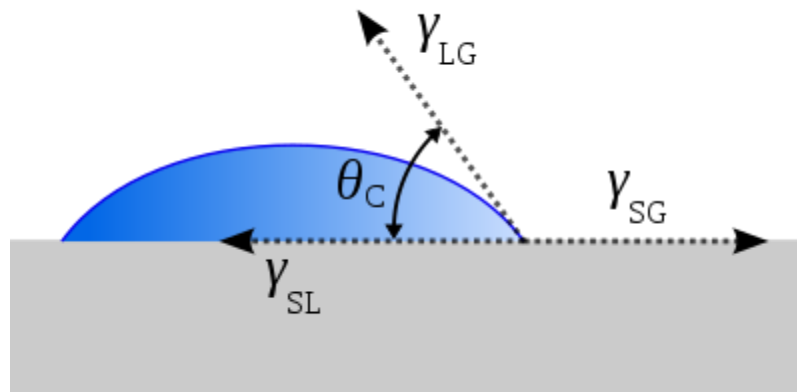


Figure 18. Schematic representation of the three phase-system and the contact angle[120].

Thomas Young described this as an energy balanced approach to three equilibrium interfacial tensions, using **Equation 4**. [121].

$$\cos\theta = \frac{\gamma_{SG} - \gamma_{SL}}{\gamma_{LG}} \quad \text{Equation 4.}$$

In which:

θ is the contact angle.

γ_{LG} is the liquid-vapor interfacial

tension. γ_{LG} is the solid-vapor interfacial tension. and

γ_{SG} is the solid-vapor interfacial tension.

The contact angle of a material is mainly influenced by its composition and surface chemistry, however factors like the morphology of the surface can also influence the contact angle. The lower the contact angle the more hydrophilic the sample is, with higher contact angles indicating that the sample has a hydrophobic nature[121].

In this work the contact angle of pristine 316L SS, 316L SS with UV and thermal treatment with and without silanization was analysed using the equipment Contact Angle System OCA 15 (Dataphysics) using the sessile drop method at room temperature, measuring the contact angle at both sides of the drop. A 3 μ l water drop was dispensed by the integrated micropipette, each measurement recorded by the systems' integrated camera and the obtained data was then processed using the software OneAttention.

3.7.6. Differential Scanning Calorimetry

Calorimetry is a primary technique that allows to relate how a samples physical properties change with temperature over time, as well as being a direct method of measuring the enthalpy of processes of interest.

The differential scanning calorimeter is a tool that measures the heat energy uptake of a sample as its' temperature changes. DSC work by supplying energy simultaneously to a sample cell containing solution and the sample of interest and a sample cell containing only solution, the temperature of both cells will then be raised at the same time. Since the cell with the sample will need more energy to increase its temperature it is possible to calculate the difference in the energy supplied to the two different cells, with the excess energy being the energy absorbed or released by the sample to raise its temperature.

The parameters defined in DSC can then be used to calculate parameters such as the percentage of crystallinity (**equation 5**)[122].

$$X_c(\%) = \frac{\Delta H}{\Delta H_0} * 100 \qquad \text{Equation 5.}$$

In which:

X_c is the percentage of crystallinity

ΔH is the enthalpy of fusion of the sample

And

ΔH_0 is the the enthalpy of fusion of a 100% standard sample.

3.7.7. X-Ray Diffraction

X-ray Diffraction (XRD) is a non-destructive material characterization technique that allows to study the crystal structures and atomic spacing in crystalline samples.

XRD is based on the phenomenon of wave interference that happens when X-rays interact with a crystalline sample. Incident X-rays on the sample will then be diffracted by the crystallographic planes, and when constructive interference occurs it is possible to obtain information about the crystalline phase using Bragg's Law (**equation 6**).

$$n\lambda = 2d\sin\theta \qquad \text{Equation 6.}$$

Where:

n is an integer (otherwise there will not be constructive interference)

λ is the X-rays' wavelength

d is the distance between the parallel crystal planes

and θ is the diffraction angle.

The sample is then irradiated with X-rays from constantly changing incident angles, scanning through a range of 2θ angles, this will then allow for the generation of a spectrum of intensity versus diffraction angle. The X-ray diffractometer consists of 3 main components the X-ray tube, the sample holder and the X-ray detector, the diffractometer also has slits to converge the X-rays and a monochromatic filter to filter the X-rays before being received by the detector[112,123].

To analyse thin films in XRD the thin film should be deposited in a substrate, the incident X-ray beam should have a small angle of incidence, for this reason this technique is called grazing incidence XRD. The parallel X-rays hit the thin film at a small angle, usually 0.5° to 2° , the diffracted X-rays will then be collected by a detector that scans along 2θ of the sample.

The data obtained can then be used to calculate the degree of crystallinity by calculating the area of the crystalline peaks and the total area of the graph. The degree of crystallinity can be calculated using **equation 7**[124].

$$\text{Degree of Crystallinity} = \frac{\sum I_{net}}{\sum I_{tot} - \sum I_{cont.bgr}} * 100 \quad \text{Equation 7}$$

Where:

$\sum I_{net}$ is the integrated area of the crystalline area,

$\sum I_{tot}$ is the total area of the graph

And

$\sum I_{const.bgr}$ is the constant background from the diffractogram.

In this work the thin films of PLLA subjected to different crystallization treatments, and deposited in 316LSS with different treatments was done in a X'Pert PRO³ (Panalytical) using the following parameters: 2θ range 5° - 30° ; step size 0.0260° , time per step 397.29 seconds and grazing angle 2° . The data from the XRD was then processed using the software OriginPro to calculate the area of the peaks and the graph which was then used to assess the degree of crystallinity

3.7.8. Substrate characterization

In order to characterize the different substrates in the different phases of the treatment process several methods were used, those include: FTIR, SEM, AFM, Optical Microscopy and Contact angle measurements

3.8. Film characterization

The PLLA films deposited on top of the substrates were characterized using FTIR, SEM, Optical Microscopy, Contact Angle measurements, DSC and XRD.

3.9. Simulated Body Fluid Tests

Before proceeding to animal testing, it is often advised and useful to predict the *in-vivo* bone bioactivity of the implants. That can be done *in-vitro* through SBF tests. Simulated body fluid (SBF), which is a test liquid designed to have nearly the same concentration of ions as the human body plasma.

SBF tests are based on the principle that the main requirement for a material to bond to living bone is the formation of apatite on its surface, this phenomenon that usually occurs *in vivo* can be replicated *in vitro* using SBF, since the apatite formed in SBF is similar in structure and composition to that of the bone mineral. However, since SBF is a solution that is supersaturated in apatite its preparation should be done carefully according to the formulation and recipe that has been developed over the time to avoid precipitation. Even though SBF tests the apatite formation on the surface of the tested material there are some exceptions of material that can bind directly to the living bone without apatite formation[125].

In this work SBF was prepared in a polyethylene container at 36.5 degrees under constant agitation following the recipe provided by Kokubo[125] et al. respecting the

reagent order, while waiting for the lastly added reagent to be completely dissolved before adding the next one. After the dissolution of all the reagents solution's pH was adjusted to 7.40 using 1.0M HCl. The samples were then placed with SBF in polyethylene containers using 10mL of SBF, this volume was determined according to **Equation 8**.

$$\text{Solution Volume} = \text{Sample surface area}(\text{mm}^2)/10 \quad \text{Equation 8.}$$

Thermally treated and silanized samples subjected to different crystallization procedures (180°C for 3 minutes followed by 120°C for 45 minutes and 120°C for 60 minutes) were tested with thermally treated and silanized 316L SS being used as control. The samples were soaked in SBF for periods of 3, 7, 14 and 28 days at 37°C. Besides the main samples one pristine 316L SS sample and one thermally treated sample without silanization were also left to soak for 14 days. After removing from SBF the samples were rinsed and dried with the air gun. The pH of the solution and mass of the samples before and after immersion in SBF was also monitored. The samples were then analysed under SEM, to analyse the development of apatite on the surface of the samples and gain some insight on how the PLLA film would degrade in the human body environment.

3.10. Adhesion tests

The PLLA film adhesion to the SS substrate was tested using the cross-hatch tape test using pressure sensitive tape. This adhesion tests were performed in accordance to standard ASTM D3359-17 “Standard Test Methods for Rating Adhesion by Tape Test”[126]. In this standard there are two methods referred, after analysing both the method B was deemed as more appropriate for this work.

This method consists of performing 5 cuts with 1 mm distance between them in the film, both vertically and horizontally, with the use of an x-acto knife at an angle between 15 to 30°, in order to form a grid. These cuts were performed using a 3d printed guideline to help maintain the distance between the cuts. Then pressure sensitive tape (Elcometer 99) is applied over the grid and pressure is applied using a rubber band to guarantee and uniform contact of the film with the adhesive of the tape. The tape is then left on the substrate for 60s and removed at an angle of 180°. This process is shown in **Figure 19**.

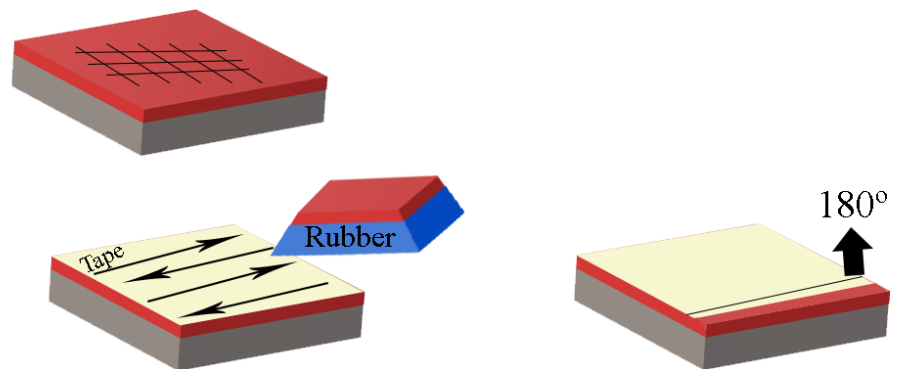
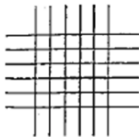
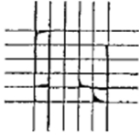
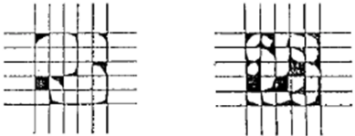
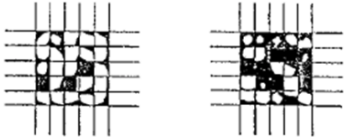
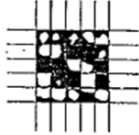


Figure 19. Schematic representation of the cross-hatch tape test process

The samples are then analysed under an optical microscope and a stereo microscope, the sample is then graded qualitatively on scale from 0 to 5 using table X as a guide.

Table 3. Classification of tape test results according to standard ASTM D3359[126].

CLASSIFICATION OF ADHESION TEST RESULTS		
CLASSIFICATION	PERCENT AREA REMOVED	SURFACE OF CROSS-CUT AREA FROM WHICH FLAKING HAS OCCURED FOR SIX PARALLEL CUTS AND ADHESION RANGE BY PERCENT
5B	0 % None	
4B	Less than 5 %	
3B	5 – 15 %	
2B	15 – 35 %	
1B	35 – 65 %	
0B	Greater than 65%	

3.11. Cellular tests

In order to better test the biological response of the samples cellular tests will be performed, these tests will include, Cytocompatibility studies, which will be done by evaluating the interaction of Human Dental Pulp stem cells (hDPSCs) which will be maintained in culture medium at 37°C and a 95% humidified atmosphere with 5% CO₂. A viability will be assessed by performing the PrestoBlue® Viability Assay, which is based on using a resazurin-based solution as a indicator of the cell reducing power to quantitatively measure cell viability. Changes in viability and metabolic rate will be detected by performing absorbance spectroscopy 24h, 72h,120h and 168h after the beginning of the test. And cell adhesion will be qualitatively evaluated by performing SEM imaging of the implants.

3.12. In Vivo tests

In vivo tests will be performed by inserting the implants unilaterally in the animal model. (Merino sheep) The tissue response will be evaluated using X-ray, SEM and μ CT (microcomputed tomography) imaging techniques in addition to histopathological and histomorphometric analysis. All the procedures will be done according to ISO 10993- 6:2016 and ASTM F981 “Standard Practice for Assessment of Compatibility of Biomaterials for Surgical Implants with Respect to Effect of Materials on Muscle and Insertion into Bone”.

Chapter 4 – Results and Discussion

Chapter 4 – RESULTS AND DISCUSSION

4.1. Characterization of 316L SS substrates after pre-treatment

In this section the results of the pre-treatments to which the substrates were subjected to, which include thermal treatment and UV irradiation will be presented and discussed. In order to better understand the effect of the different pre-treatments it is also necessary to characterize the pristine 316L SS substrates.

According to the supplier of the stainless-steel substrates, Goodfellow Cambridge Limited, the 316L stainless steel alloy used is subjected to an annealing treatment following the standard BS EN 10088-2 (1.4404), the heat treatment took place at 1040°C and was held for a short period of time, the alloy was then water-quenched to avoid carbide precipitation.

As mentioned in chapter 3 the 316L SS substrates were subjected to different pre-treatments heat treatment at 500°C for 2 hours or UV irradiation for 2 hours. After heat treatment it was possible to observe a change in the coloration of the 316L SS, the colour changed from a light grey colour to a dark purple or brown colour. This phenomenon has been reported in the literature and it is related with the formation of thermal oxides on 316L stainless steel[127]. While thermal treatment caused visible changes in the colour of the samples the UV treatment does not seem to cause any changes that are visible to the naked eye. Images of both untreated 316L SS substrate and treated (thermal and UV) 316L SS substrates are presented in **Figure 20**.



Figure 20. Picture of Pristine 316L SS (left), thermally treated 316L SS (middle) and UV treated 316L SS (right)

To further analyse the effect that the different pre-treatments had on the 316L SS substrates, FTIR analysis was performed to identify possible molecules or chemical compounds that may have formed on the surface during the treatments. The FTIR spectre

was recorded using the absorbance percentage as a function of the wavenumber varying from 500 cm^{-1} to 4000 cm^{-1} . The obtained spectra are presented in **Figure 21**.

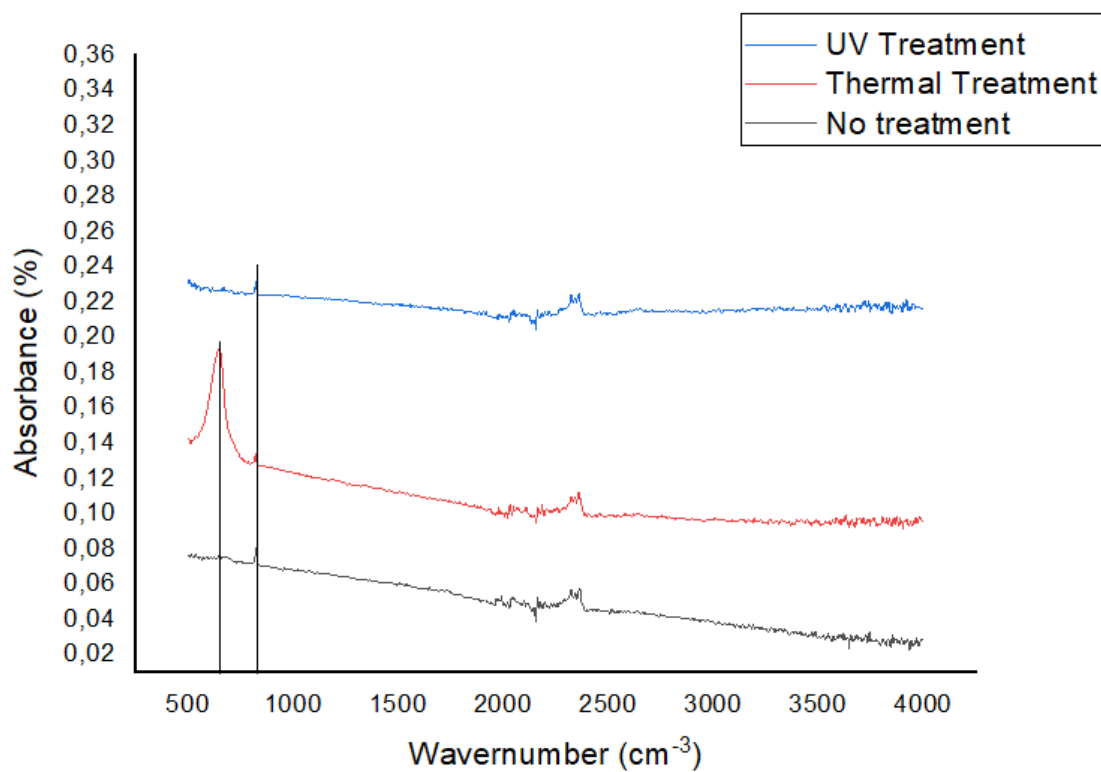


Figure 21. FTIR spectrum of a pristine 316L SS substrate (black line) and 316L SS substrates after thermal (red line) and UV treatment (blue line).

By observing the spectrum, it is possible to detect a fluctuation in the base line from the wavenumber 2000 cm^{-1} until around 2500 cm^{-1} this is caused due to effect of the atmospheric CO_2 [128] and should be disregarded. A peak at around the wavenumber of 910 cm^{-1} can be observed in all the samples, this peak corresponds to O-H bending/N-H wagging[129].

In the thermally treated sample it is possible to observe a peak at the wavenumber of 659 cm^{-1} , this peak corresponds to chromium oxide (Cr_2O_3)[130], since this peak is exclusive to the thermally treated sample so it can be concluded that during the formation of Cr_2O_3 happens during thermal treatment, this goes in accordance to what was previously discussed, allowing the conclusion that the formation of Cr_2O_3 is responsible for the change in colour of the 316L SS substrates. The chromium oxide layer has been shown to increase the steel resistance to corrosion[130,131]. The FTIR peaks found are shown in **Table 4**.

Table 4 FTIR peak assignment for 316L SS before and after thermal or UV treatment.

Wavenumber (cm ⁻¹)	Peak assignment
659	Chromium Oxide (Cr ₂ O ₃)
910	δ(O-H)/ ω(N-H)

To better understand the effect of each treatment had, the 316L SS substrates were subjected to SEM analysis in order to obtain information about its' microstructure. The obtained SEM micrographs are displayed in **Figure 22**.

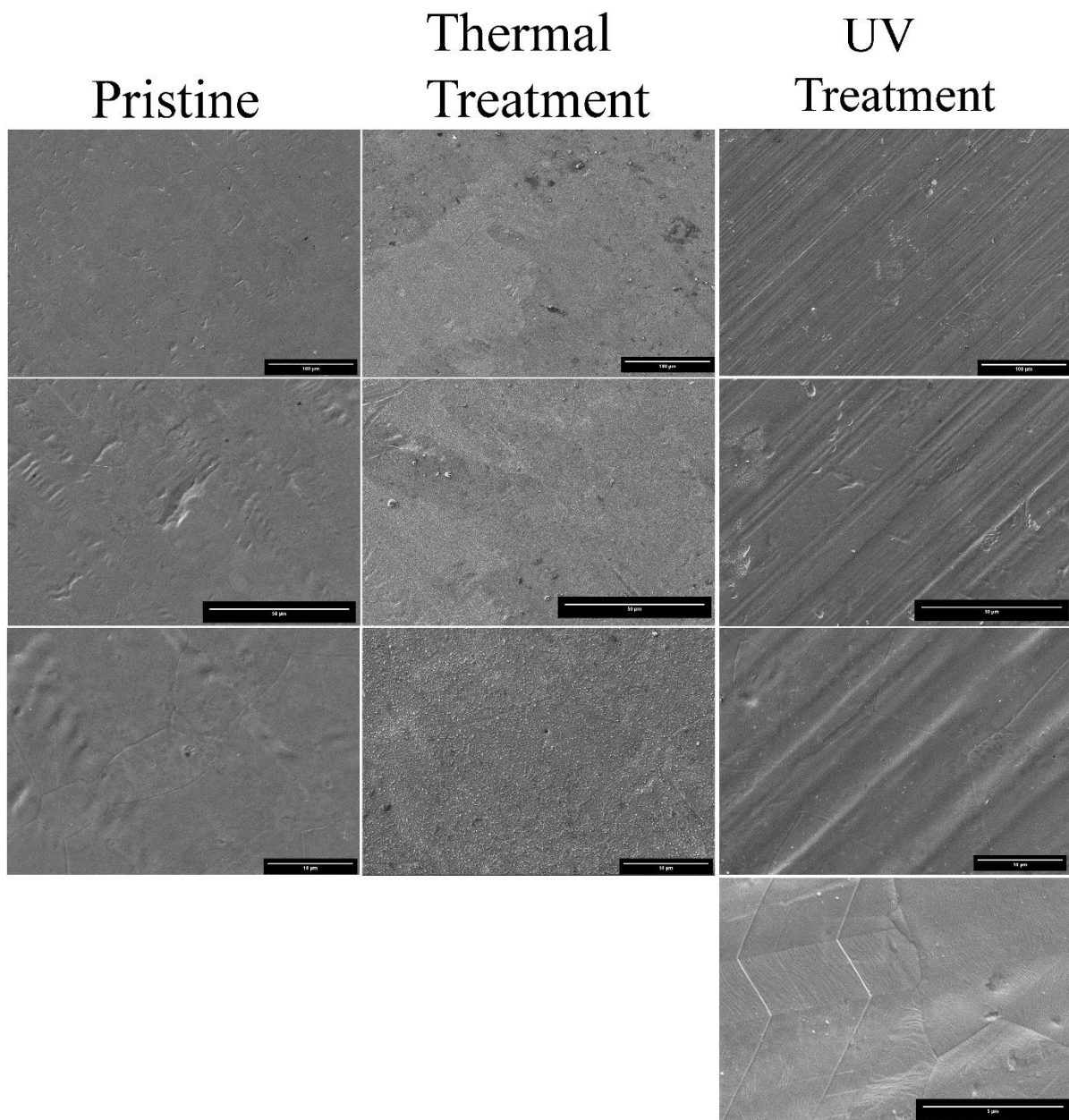


Figure 22. SEM micrographs of pristine 316L SS and UV treated 316L SS with different ampliations

In the pristine 316L SS it is possible to observe a relatively smooth surface with some indentation marks. In higher ampliations it is possible to observe the steel grain and grain boundaries.

When observing the thermally treated 316L SS there are some noticeably lighter and some darker areas, this is probably due to the formation of the chromium oxide, which might be uneven across the surface. In lower magnification micrographs the thermally treated substrates seem to have a smooth surface with some particles showing, however when the

ampliation is increased it is possible to see that the surface is considerably rough, with textured spots evenly distributed across the sample. According to the literature the thermal treatment should cause the growth of the stainless steel grain [127]. With higher ampliation it is also possible to notice some grain boundaries, although they are barely noticeable, the lack of visibility of the grain boundaries might be caused by them being obscured by the chromium oxide layer formed on top of the substrate.

In the UV treated 316L SS substrates the main change from the untreated substrate is its' highly textured surface with diagonally oriented grooves. In these samples it is possible to observe the grain and grain boundaries but only at high magnifications, similarly to what happened in the untreated substrates.

Substrates were then subjected to AFM analysis to complement the SEM results; the results are shown in **Figure 23.** and **Table 5.** below.

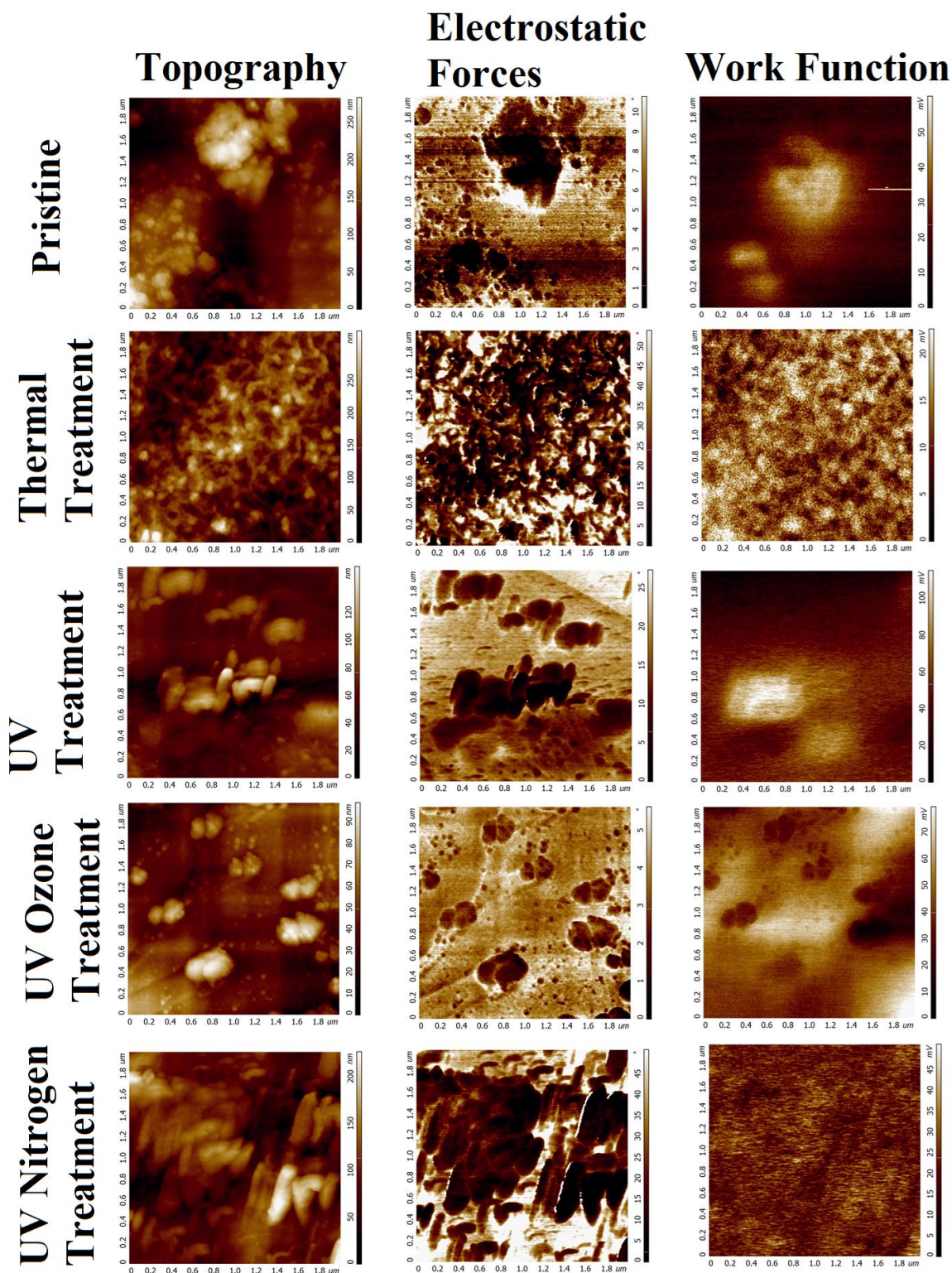


Figure 23. AFM topography, electrostatic forces and work function scans acquired on 316L SS before and after treatments, including thermal, UV, UV/Ozone and UV/Nitrogen.

Table 5. Work function of the 316L SS substrates after the different treatments as determined by AFM.

Substrate Treatment	Work Function (eV)
Pristine	4.80
Thermal Treatment	5.15
UV Treatment	4.20
UV Ozone Treatment	4.65
UV Nitrogen Treatment	4.90

In the topography analysis of the pristine substrate, it was possible to observe some features which are related to the roughness of the stainless steel, which can be originated in the manufacturing process of the steel. Those features seem to have an impact on the electrostatic forces of the sample with the higher points causing them to decrease. The surface roughness also seems to impact the work function of the substrate since it is possible to observe a higher work function in the area of the surface artifact.

Thermal treatment generated a mesh like structure on the substrates as is observable in the topography analysis. This treatment also has caused a decrease in the electrostatic forces of the substrate comparatively with the pristine one, this is caused by the layer of chromium oxide formed on top of the sample which can act as a trap to charges. In this sample there seems to be an increase on the work function of the sample which can be attributed to the chromium oxide layer.

All the samples treated with UV irradiation seem to have similar topographies, being possible to observe the formation of oval shaped features on top of the surfaces. These features seem to affect the electrostatic forces of the substrate causing them to decrease. While in the sample treated with UV irradiation in a nitrogen atmosphere these features don't seem to have an influence on the work function, in the samples treated with UV irradiation and UV irradiation in an ozone atmosphere these features have caused a decrease of the work function, which is beneficial to the adhesion of polymers to the metal.

Since the main purpose of the pre-treatments of the substrate is to generate OH groups in the surface in order to improve the silanization process, the effectiveness of each method to generate OH groups was tested by measuring the samples' contact angle, since

the contact angle is influenced by the presence of OH groups[132]. Pictures of the contact angle of the different substrates during the measuring process are presented in **Figure 24**.

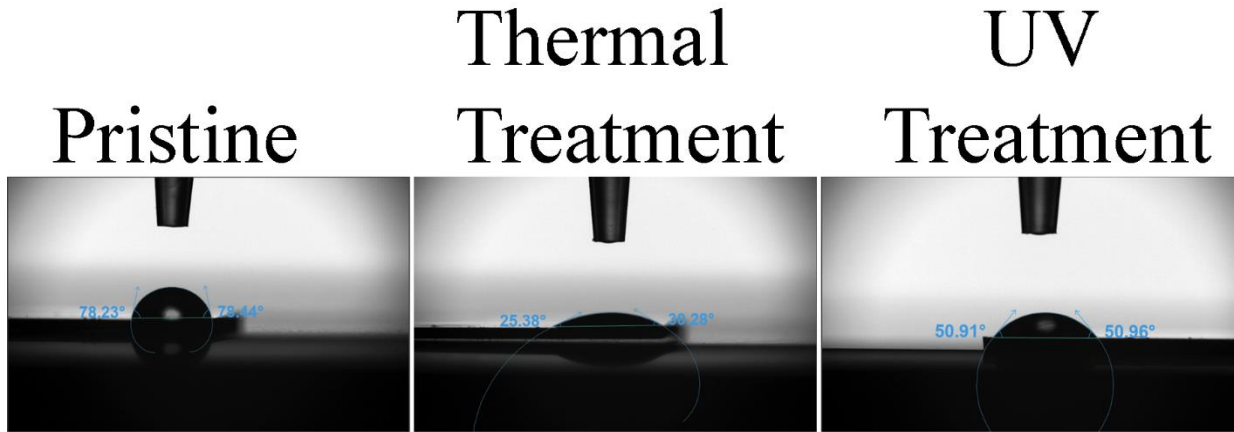


Figure 24. Images of the contact angle on pristine 316L SS (a), thermally treated 316L SS (b) and UV treated 316L SS (c) captured during the measuring process. It is possible to observe different contact angles according to the different treatments.

The obtained contact angle values are presented in **Table 6**.

Table 6. Contact angle values obtained for the 316L SS substrates subjected to the different treatments.

Treatment	Contact angle (°)
Pristine	78.15 ±3.06
Thermal	28.07 ±3.10
UV	49.96 ±4.02

By analysing the obtained values, it is possible to conclude that all the 316L SS samples are hydrophilic, but it is possible to observe drastic changes in the contact angle, this indicates that there was in fact a generation of OH groups in the surface of the samples through the used treatments. While UV treatment showed itself capable of generating OH groups causing a decrease in the contact angle, the thermal treatment seemed to be more effective in the generation of OH groups since it provided an even lower contact angle.

In conclusion it is possible to verify that the chosen treatments were effective in the generation of OH groups to allow the silanization of the substrates and increase the effectiveness of the silanization process. But besides that, there were beneficial side effects

such as the surface changes detected by the SEM analysis which caused an increase in the roughness of the substrates, which can contribute for an improved adhesion between the substrate and the PLLA film, however this increase in the surface's roughness also affects the contact angle, increasing it. Another beneficial side effect was the generation of the chromium oxide layer during the thermal treatment which may increase the resistance to corrosion.

4.2.Characterization of 316L SS substrates after silanization

In this section the results of the silanization process to which the substrates were subjected to, improve the adhesion of the PLLA films will be presented and discussed.

To know if the silanization process was successful FTIR analysis was performed in order to know the chemical groups present on the surface of the substrates, this was done to confirm the presence of the silanes. The FTIR spectrum obtained are present in **Figure 25**.

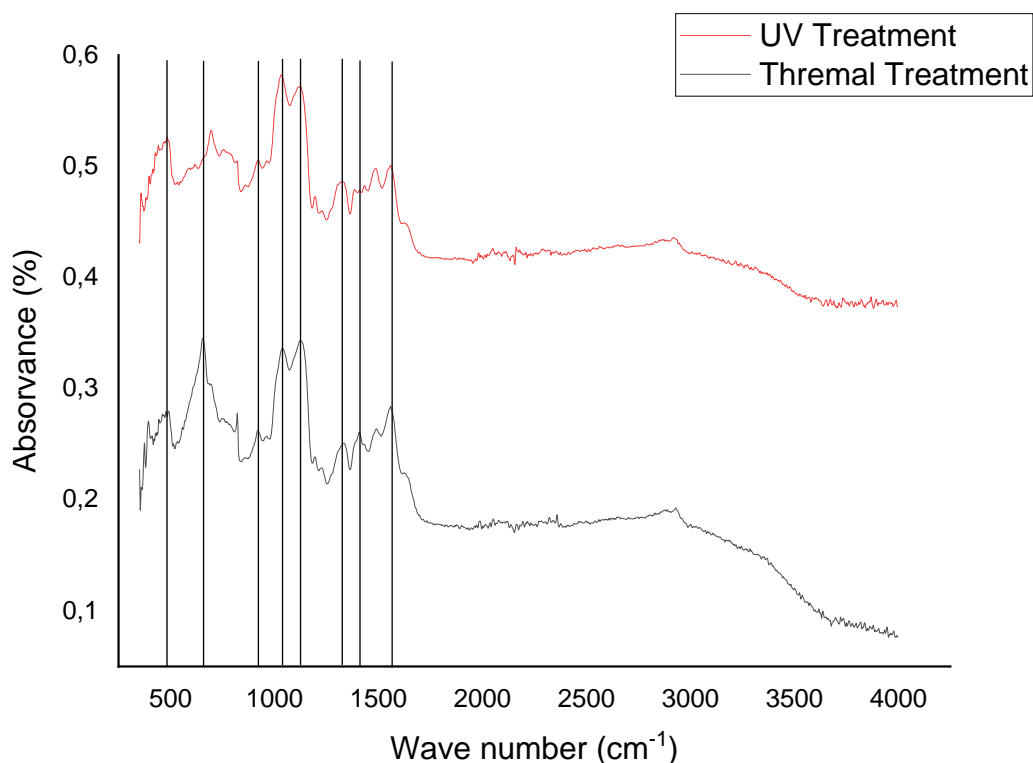


Figure 25. FTIR spectrum of silanized 316L SS substrates. The 316L SS substrates were subjected to different treatments before silanization, which include thermal (red line) and UV treatment (blue line). It is possible to observe the vibrational modes corresponding to the silanes in both the spectra.

By observing the FTIR spectre obtained for both samples it is possible to observe the peaks present in the samples treated with thermal treatment and UV previously analysed, with a baseline caused by the presence of atmospheric CO₂ between the wavenumbers of 2000 to 2500 cm⁻¹. At around the wavenumber of 910 cm⁻¹ there is a peak which corresponds to O-H bending/N-H wagging, and at the wave number of 659 cm⁻¹ there is a peak which corresponds to chromium oxide (Cr₂O₃), however in the previous samples this peak was only found in the thermally treated substrates, after silanization it is possible to find it in both thermal and UV treated substrates, even though the peak intensity in the UV treated sample is much smaller than that on the thermally treated substrate.

At around the wavenumbers of 500, 1040 and 1140 cm⁻¹ it is possible to observe two peaks, these two peaks are correspondent to the asymmetric stretching vibration of the Si-O-Si groups[133,134] which are formed by the crosslinking of the silanes on the surface. These peaks are good indications that there are silanes present in both the substrates and as such that the silanization process was successful.

The peaks at the wavenumbers of 1484 and 1562 cm⁻¹ are assigned to the deformation modes of NH₂ groups from the silanes which form strong hydrogen bonds with the silanol groups to form cyclic structures[134]. This allows for further confirmation that the silanization process was indeed successful. The peak present at wavenumber of 1410 cm⁻¹ is assigned to the deformation mode of Si-CH₂ groups[134].

The found peaks are summarized in **Table 7**.

Table 7. FTIR peak assignment for 316L SS subjected to Thermal or UV treatment and posteriorly silanized.

Wavenumber (cm ⁻¹)	Peak assignment
500	ν_{as} (Si-O-Si)
659	Cr ₂ O ₃
910	δ (O-H)/ ω (N-H)
1040	ν_{as} (Si-O-Si)
1140	ν_{as} (Si-O-Si)
1410	δ (Si-CH ₂)
1484	δ (NH ₂)

Chapter 4 – RESULTS AND DISCUSSION

1562	δ (NH ₂)
------	-----------------------------

To further analyse the effect of the silanization process on the substrates their microstructure was studied using SEM. The obtained SEM micrographs are present in **Figure 26**.

Thermal
Treatment
Silanized

UV
Treatment
Silanized

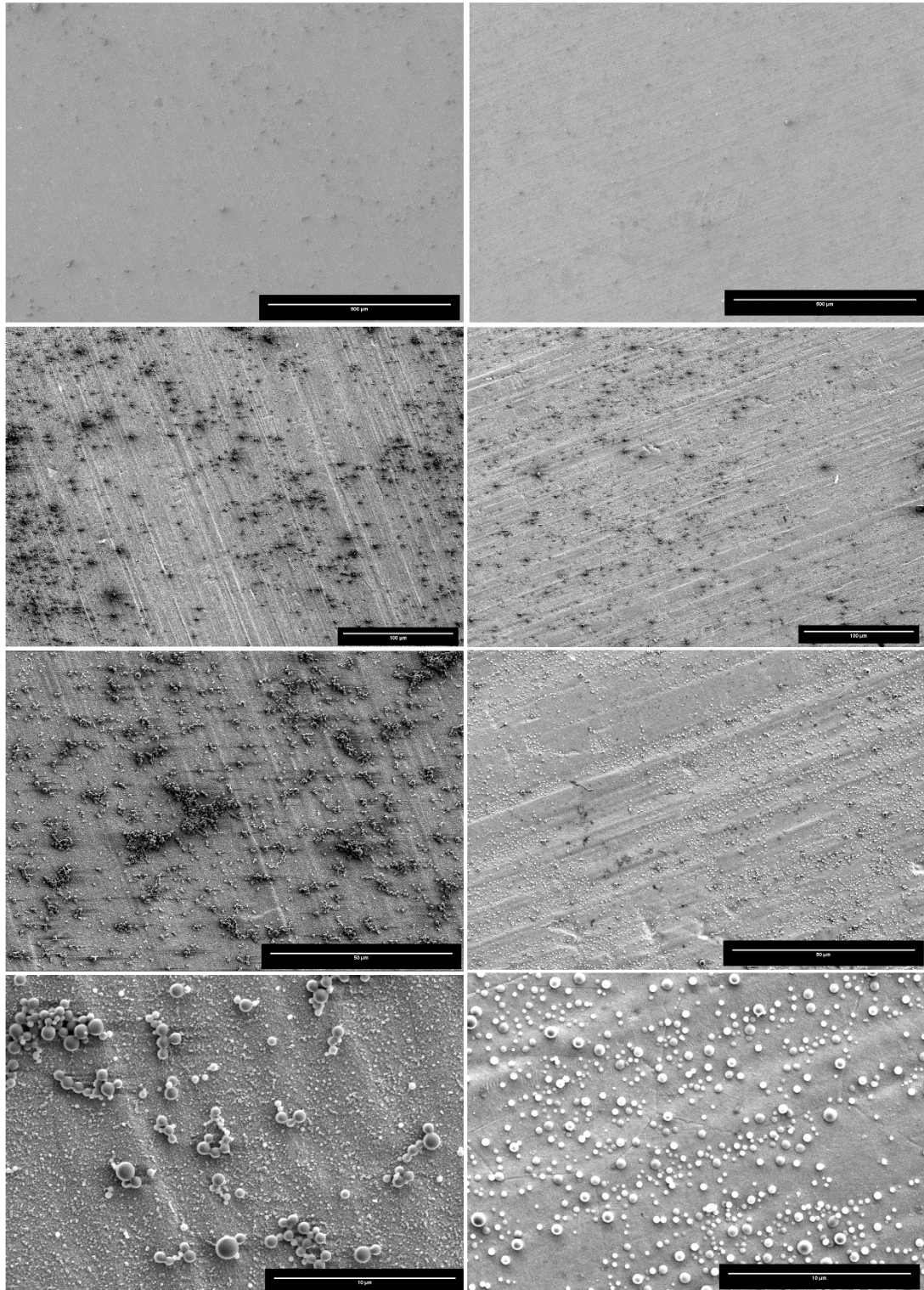


Figure 26. SEM micrographs of silanized thermally treated 316L SS with different ampliations. These micrographs were obtained using an electron acceleration field of 4.0 kV. In the micrographs it is possible to observe the appearance of small spheric structure which are thought to be the silanes.

Similarly to what was observed before the UV samples show a grooved texture with the steel grain and grain boundaries being visible at higher magnifications. However, after silanization is also possible to observe a grooved texture on the thermally treated substrates, although there were changes in the topography of the surface the steel grain and grain boundaries continue to have low to none visibility.

The main change that is verified after silanization is the appearance of spheric structures thought to be the silanes. In order to identify the spherical structures EDS was performed, the obtained images are shown in **Figure 27.** below.

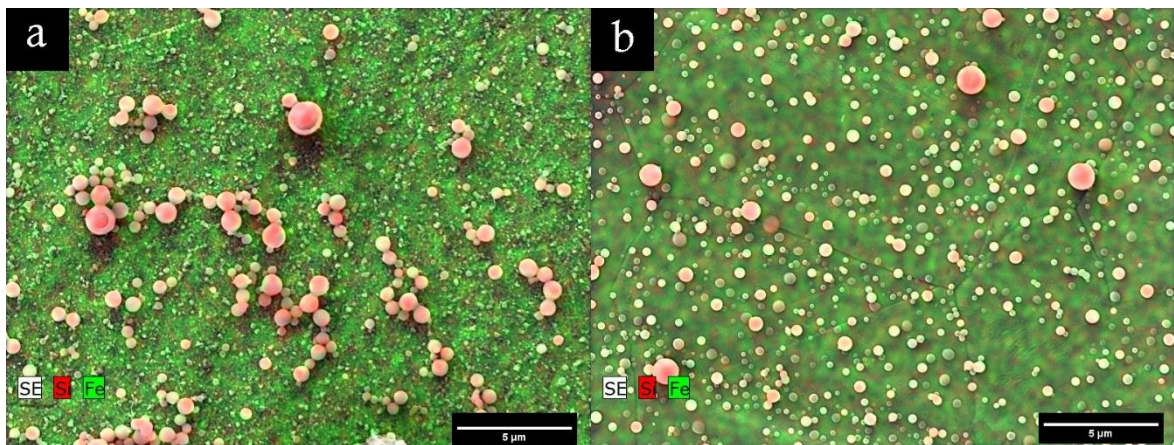


Figure 27. SEM micrographs of silanized thermally treated 316L SS (a) and silanized UV treated 316L SS (b) subjected to EDS analysis. The red represents silicon and the green represent iron.

After EDS analysis it was possible to confirm that the spheric structures are indeed silanes, since they are present silicon in its' composition.

These samples were also subjected to AFM analysis, the data obtained is presented below in **Figure 28.**

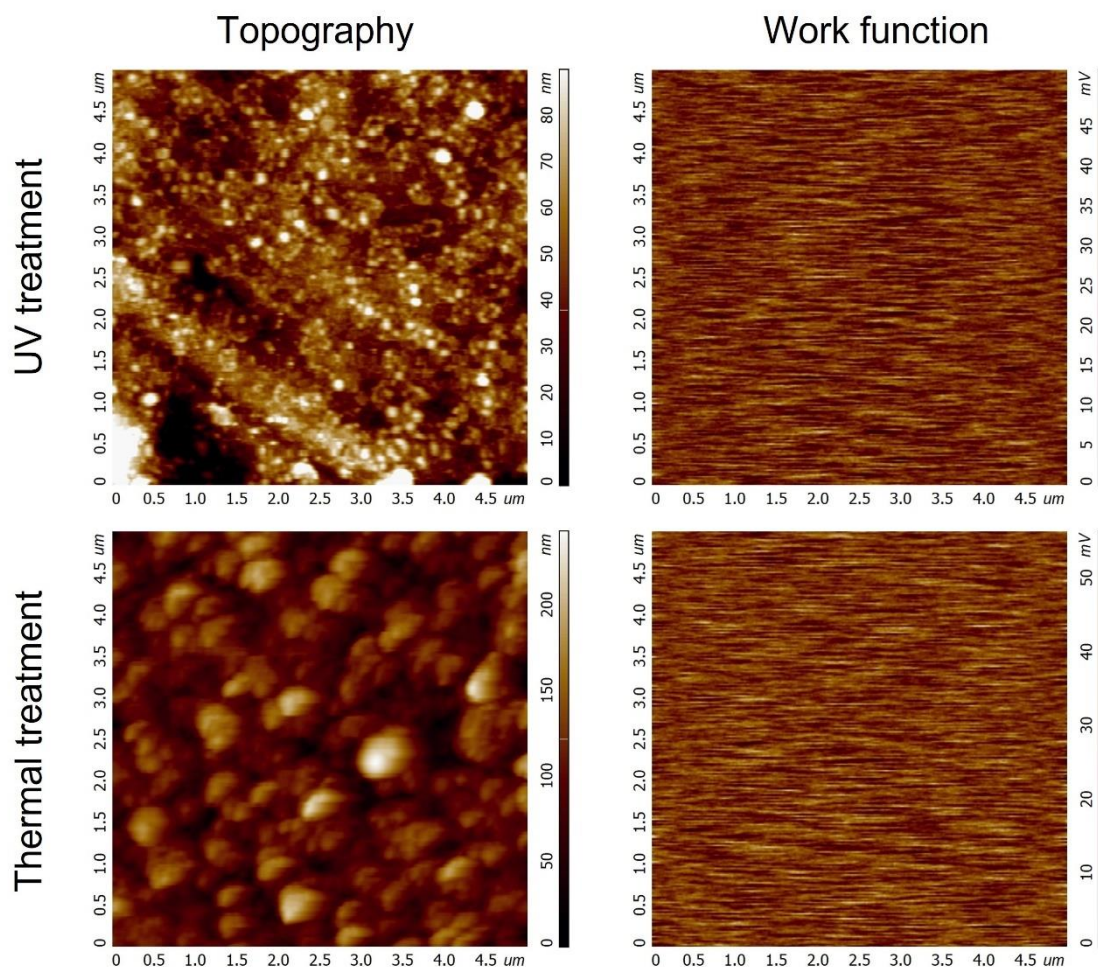


Figure 28. AFM topography and work function scans acquired on 316L SS after thermal or UV pre-treatment followed by silanization.

The results obtained in AFM seem to go in accordance to those obtained in SEM it is possible to observe larger sphere structures, which are more densely packed in the topography of the thermally treated one while in the UV treated there seems to be a more uniform layer formed across the surface. While it is possible to observe differences in the topography there seem to be no difference in work function between the two samples. This indicates that after silanization the pre-treatment seem to have no income in the outcome, since the surface is covered by silanes.

The addition of the silanes contributes to the overall surface roughness in both thermally treated and UV treated samples. It is possible to observe that in the thermally treated samples silanes tend to concentrate in certain areas, which ends up causing the formation of bigger silane clusters. While in the UV treated samples the silanes seem to be more evenly distributed and the formation of clusters looks reduced compared to the thermally treated substrate. Assuming that a lower contact

angle directly relates to a higher concentration of OH groups these results are contradicting with the literature, according to Jussila et al.[93] higher concentrations of OH groups on the surface should lead to silane monolayer while low concentrations of OH groups on the surface should lead to clusters with a weak adhesion to the metal. This is contradictory with the results obtained since the thermally treated substrate presented a lower contact angle than the UV treated substrate, however it is the thermally treated substrate that presents a less uniform silane distribution while having a more prominent formation of clusters.

To further study the effectiveness of the silanization the contact angle of each sample was measured since it can be an important factor in the adhesion between polymers and metals. Pictures obtained during the process of measuring the contact angle are presented in **Figure 29**. while the obtained values as well as the previous obtained values are present in **Table 8**.

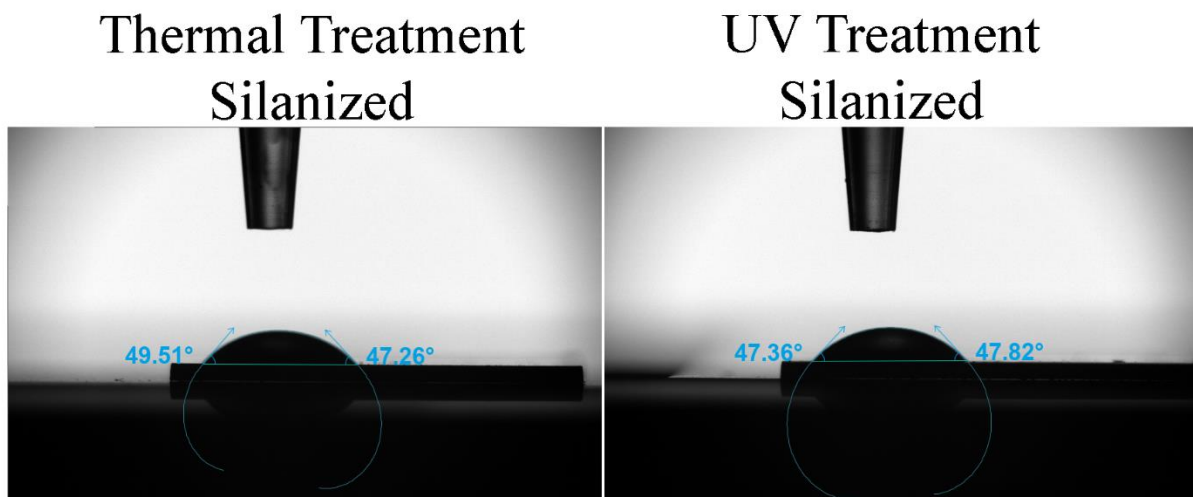


Figure 29. Images of the contact angle on thermally treated and silanized 316L SS and UV treated and silanized 316L SS captured during the measuring process. Even though the samples were subjected to different treatments the contact angle values seem about the same.

Table 8. Contact angle values obtained for the 316L SS substrates subjected to the different treatments.

Treatment	Contact angle (°)
Pristine	78.15 ±3.06
Thermal	28.07 ±3.10
Thermal Silanized	49.53 ±4.32
UV	49.96 ±4.02
UV Silanized	48.15 ±9.02

Although before the silanization process there was a significant difference between the contact angles of the substrates subjected to the thermal and UV treatments After silanization there seem to be no difference in the contact angle this can be due to the formation of a silanes layer on top of the samples which will governate the interactions with the water drops used during the measurement.

It was possible to observe that both thermal and UV treatments were suitable as a preparation of the substrates to use in the silanization process, since it was possible to detect the presence of silanes via FTIR in samples subjected to either one of the treatments. While thermal treatment seemed more promising before the silanization process, UV treated substrates showed a more uniform silane layer after the process. Besides promoting bonding with the applied coating, the process of silanization also causes an increase in surface roughness which can be beneficial to adhesion.

4.3.Characterization of PLLA films through Differential Scanning Calorimetry

Thermal properties of the PLLA films were studied using DSC. For this purpose, PLLA solution of two different concentrations (2.5 and 5.0 wt.%) was deposited on UV treated substrates in order to produce films by spin coating and then peeled off. The peeled of films were the analysed in DSC using a constant heating rate of 5°C/min and cooling rates of 2,5 and 10 °C/min. The samples were heated from room temperature to 200°C and then cooled to room temperature. The obtained results are presented in the Table 9 below, due to complications during the analysis some of the calculations for the film produced with 2.5 wt.% PLLA solution and cooled at 5°C/min were not possible to be performed.

Table 9. Transition temperatures for amorphous PLLA films prepared with solutions with various concentrations (2.5 and 5.0 wt%) determined by DSC using different cooling rates (2 ,5 and 10 °C/min).

PLLA solution Concentration (Wt %)	Cooling rate(°C/min)	Tg (°C)	ΔH (J/g)	Tm(°C)	ΔH (J/g)	Tc (°C)	ΔH (J/g)
2.5	2	75.49	459.4	170.78	43.44	110.78	1244.67
	5	79.44	N/A	172.72	48.86	N/A	N/A
	10	80.76	79.2	171.96	44.94	101.06	216.3
5	2	82	168.75	175.57	37.22	100.66	157.35
	5	80.19	306.16	170.7	46.29	96.69	130.68
	10	79.97	77.32	172.75	40.36	91.18	27.3

After analysing the values mean values were obtained for the different transition temperatures and for the changes in enthalpy. The mean value for T_g was of $79.46 \pm 2.02^\circ\text{C}$ with the mean changes of enthalpy being 218.16 ± 146.64 . The standard deviation of the T_g values shows that there is not much influence of the concentration in the T_g value however there seem to be differences in the enthalpy changes, however, there does not seem to be any apparent relation with the varied parameters. The T_m had a mean value of $172.41 \pm 1.63^\circ\text{C}$ with an enthalpy variation mean of 43.51 ± 1.63 again these values do not seem to be influenced by the concentration of the solution used to prepare the film.

During the cooling process a mean T_c of 100.00 ± 6.43 was observed and a mean enthalpy change of 355 ± 448.89 it seems that for films produced with the PLLA solution of lower concentration (2.5%) the T_c was higher meaning that the process will start earlier in those samples. The samples cooled with a lower cooling rate also seem to have an higher T_c . It is possible to conclude that while the concentration of the solution used to prepare the film does not seem to have influence in the transition temperatures of the polymer during heating. However, during cooling the T_c seem to be influenced by both the solution concentration and the cooling rate.

4.4. Crystallization of PLLA films

In order to test the influence of different parameters on the crystallization process, PLLA films were deposited on two types of substrates and crystallized varying parameters such as crystallization method, PLLA solution concentration and cooling rate, the heating rate was kept constant at $5^\circ\text{C}/\text{min}$. Some samples were crystallized for 3 minutes at 180°C followed by 120°C for 45 minutes or 120°C for 60 minutes.

Samples crystallized on the Linkam stage for 3 minutes at 180°C followed by 120°C for 45 minutes were subjected to different cooling rates, namely 0.5, 2.5, 5, 10 and $20^\circ\text{C}/\text{min}$, while samples crystallized on the heating plate using either 3 minutes at 180°C followed by 120°C for 45 minutes, or 120°C for 60 minutes and samples crystallized on the Linkam stage at 120°C for 60 minutes were subjected to a cooling rate of $5.0^\circ\text{C}/\text{min}$, the cooling rates used can be seen in Table 10 below.

Table 10 List of different cooling rates used on the crystallization of PLLA films.

Crystallization method	Crystallization Temperature	Cooling rates used (°C/min)
Linkam Stage	3' 180°C + 45' 120°C	0.5, 2.5, 5, 10 and 20
Thermal Plate	3' 180°C + 45' 120°C	5
Linkam Stage	60' 120°C	5
Thermal Plate	60' 120°C	5

After crystallization the samples were analysed under XRD, it was possible to observe the crystallographic planes of PLLA α form in the XRD diffractogram. The α form of PLLA is characterized by 4 crystallographic peaks (110)/200, (203)/(113), (011) and (211) that will occur respectively at the scattering angles 2 theta of 19.7, 19.0, 14.6 and 22.3°[135].

The α form of PLLA was found in all the sample except for samples 29, 31 and 32 which correspond to UV treated samples crystallized at 120°C for 60 min, respectively 2.5 wt.% PLLA solution crystallized in Linkam stage, both 2.5 and 5.0 wt.% PLLA solution crystallized on the thermal plate. An example of a diffractogram for both α form PLLA and amorphous PLLA are shown in **Figure 30**. The samples crystallized using the on the Linkam stage were crystallized using the following cooling rates: The crystallinity degree was then calculated from the XRD diffractograms and is shown in **Figure 31** and **Figure 32** below.

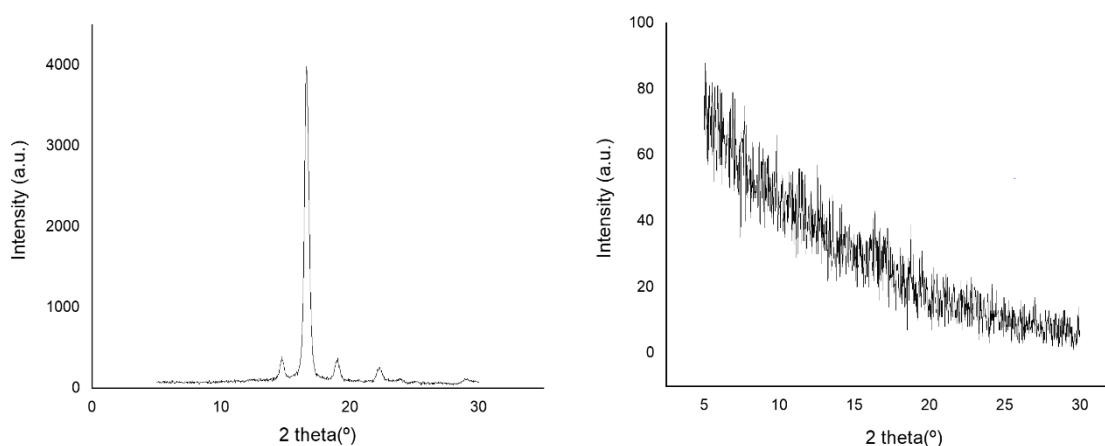


Figure 30. XRD pattern of a sample with the crystalline α form of PLLA present (left) and XRD pattern of a sample with amorphous PLLA (right).

The obtained data about the crystallinity degree of the different samples was organized in graphs in order to be easier to interpret. **Figure 31**. shows the difference between the

Chapter 4 – RESULTS AND DISCUSSION

different samples subjected to thermal treatment while **Figure 32.** show the difference between the different samples with a cooling rate of 5°C/min. The graphs are shown below.

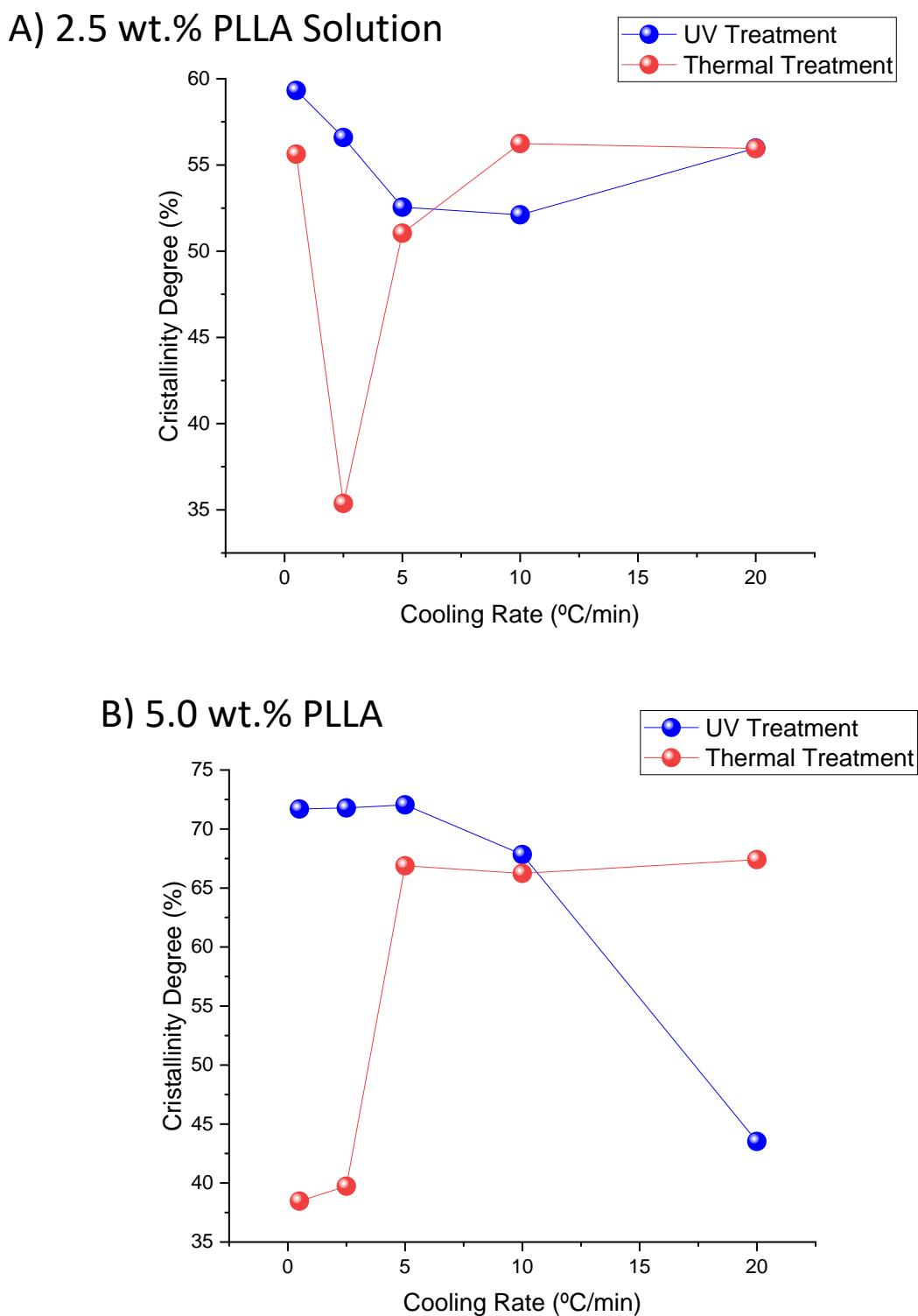


Figure 31. Crystallinity degree of the different samples crystallized in Linkam stage in function of the cooling rate. These samples were subjected to either UV treatment without silanization or Thermal treatment followed by silanization crystallized with a heating rate of 5°C/min with various cooling rates (0.5, 2.5, 5, 10, 20). The samples were prepared using two different concentration of PLLA solution 2.5 wt.% (A) and 5.0 wt.% (B).

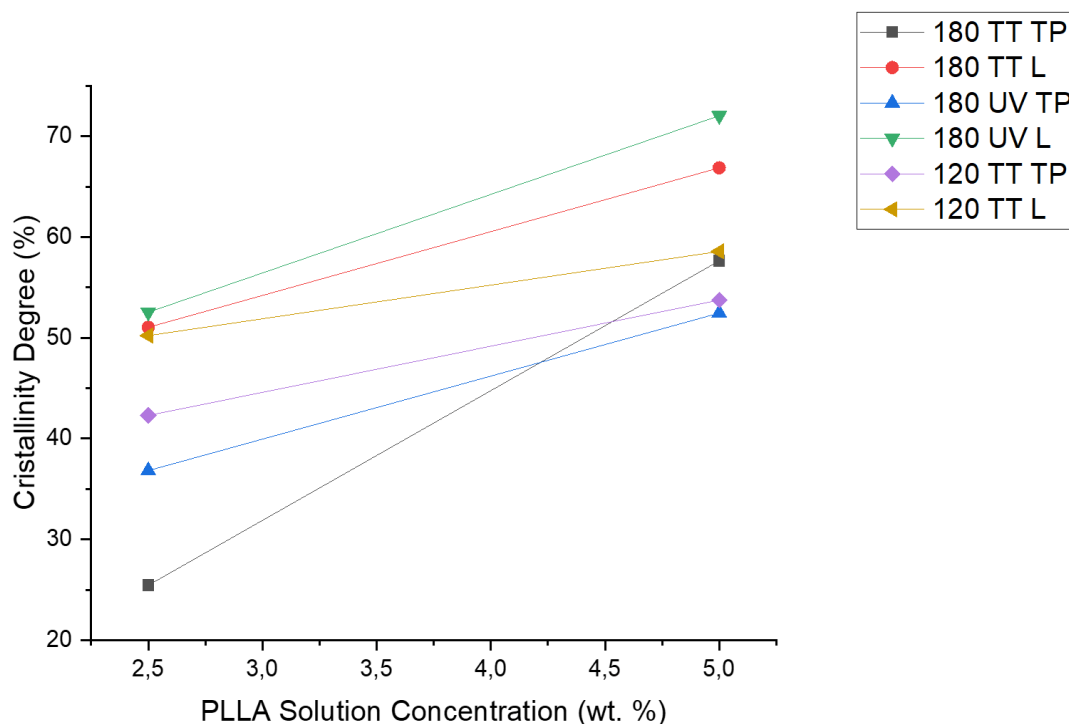


Figure 32. Crystallinity degree of the different samples crystallized in Linkam stage and heating plate in function of the cooling rate. These samples were subjected to either UV treatment without silanization or Thermal treatment followed by silanization crystallized with a heating rate of 5°C/min and a cooling rate of 5°C/min. UV- UV treatment; TT – Thermal Treatment; TP- Crystallized on thermal plate; L- Crystallized on Linkam stage.

By analysing the graphs, it is possible to notice that in UV treated substrates the crystallinity degree of the PLLA films tends to increase with the lower cooling rates, while in thermally treated samples the crystallinity seems to decrease with the lower cooling rates. Overall, the samples crystallized on the Linkam plate present a higher crystallinity degree than those crystallized on the thermal plate, this can be due to the fact that the Linkam plate provides a better temperature control than that of the thermal plate and as so allows for a more precise cooling rate. In general, the samples crystallized on the UV treated substrate also seem to allow for a greater degree of crystallinity.

The concentration of the solution also seems to have a considerable influence in the crystallinity degree of the samples with the films prepared with 5.0 wt.% solution presenting greater crystallinity. However, this crystallinity comes with a trade-off between crystallinity and adhesion, since films prepared with the 5.0 wt.% solution are more prone to peeling and

formation of air bubbles, this can be seen in the pictures obtained in the stereo microscope, as shown in **Figures 33, 34 and 35**.

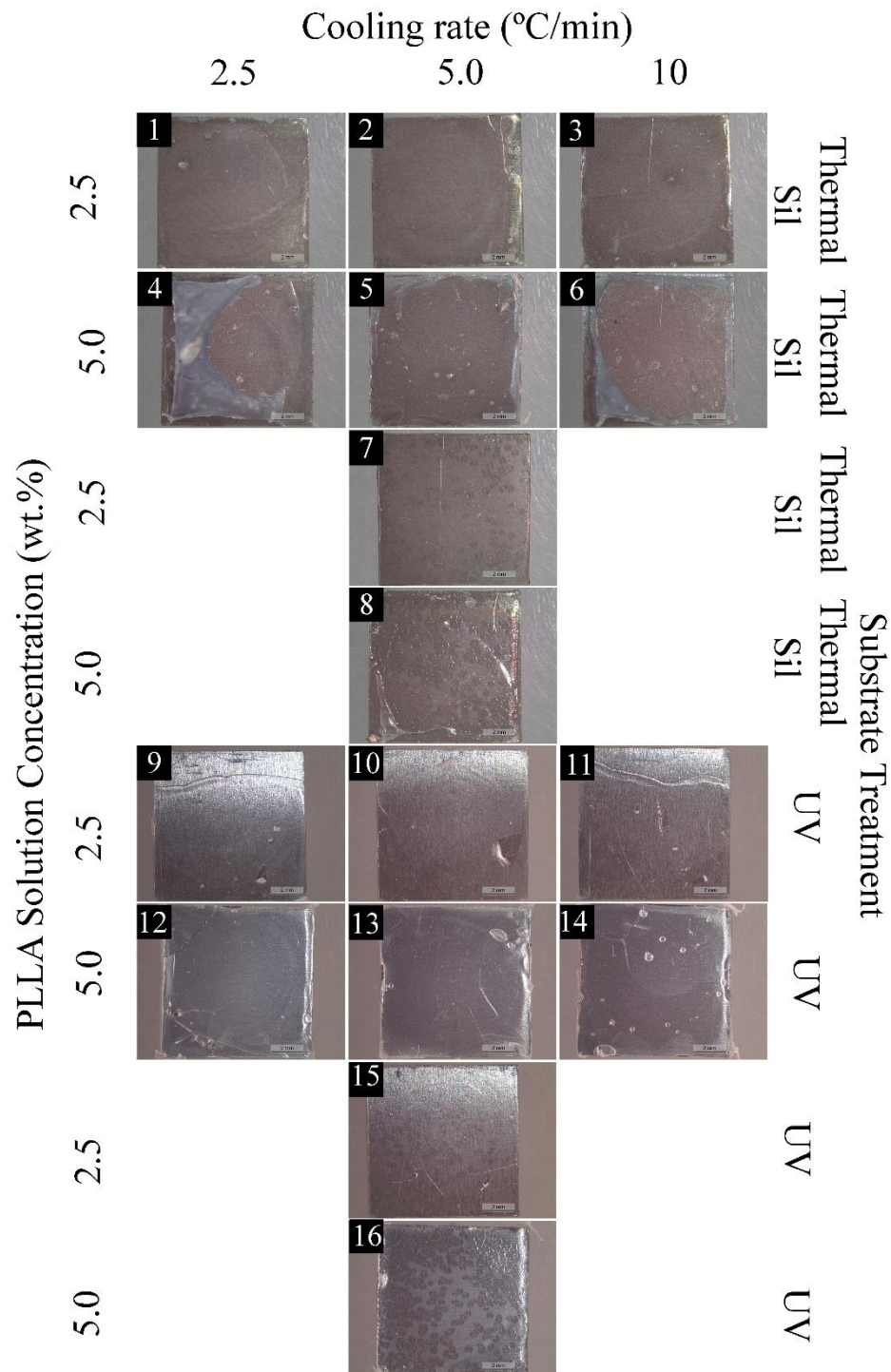


Figure 33. Thermally treated and UV treated substrates with PLLA films crystallized at 180°C for 3 minutes followed by 45 minutes at 120°C under different parameters, with cooling rates of 2.5,5 and 10°C/min observed on the stereo microscope.

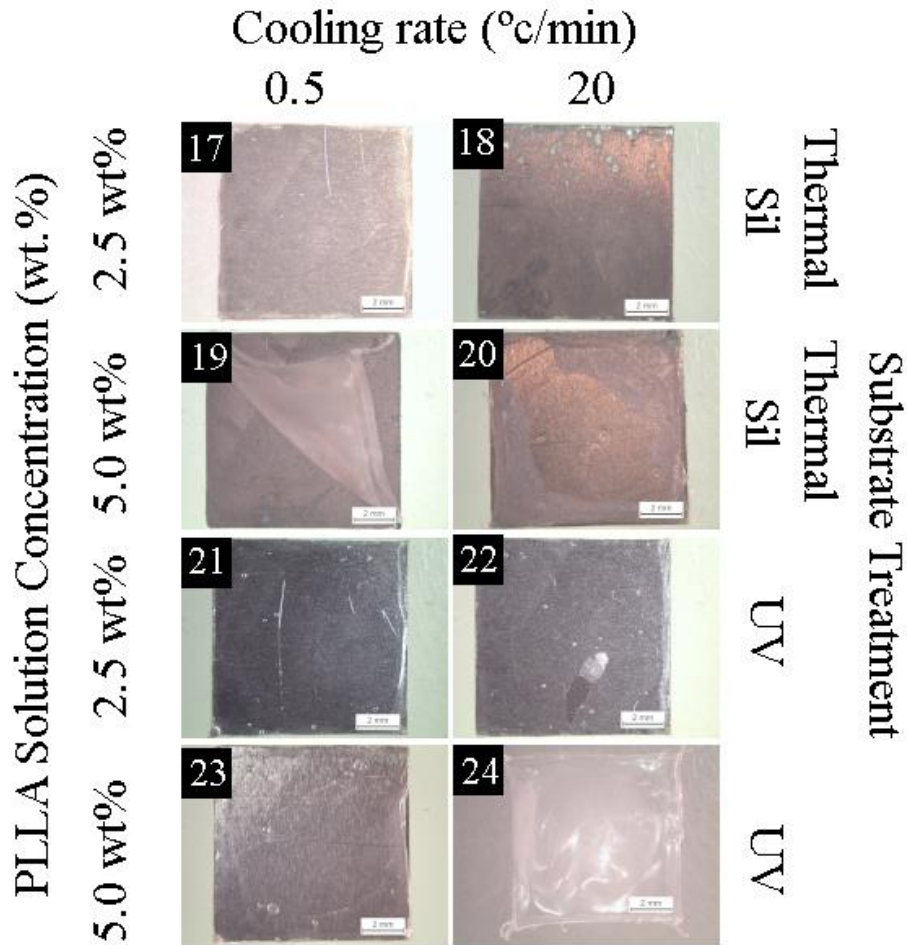


Figure 34. Thermally treated and UV treated substrates with PLLA films crystallized at 180°C for 3 minutes followed by 45 minutes at 120°C under different parameters observed on the stereo microscope. It is possible to see in figure 24 that the film completely peeled of the substrate due to poor adhesion.

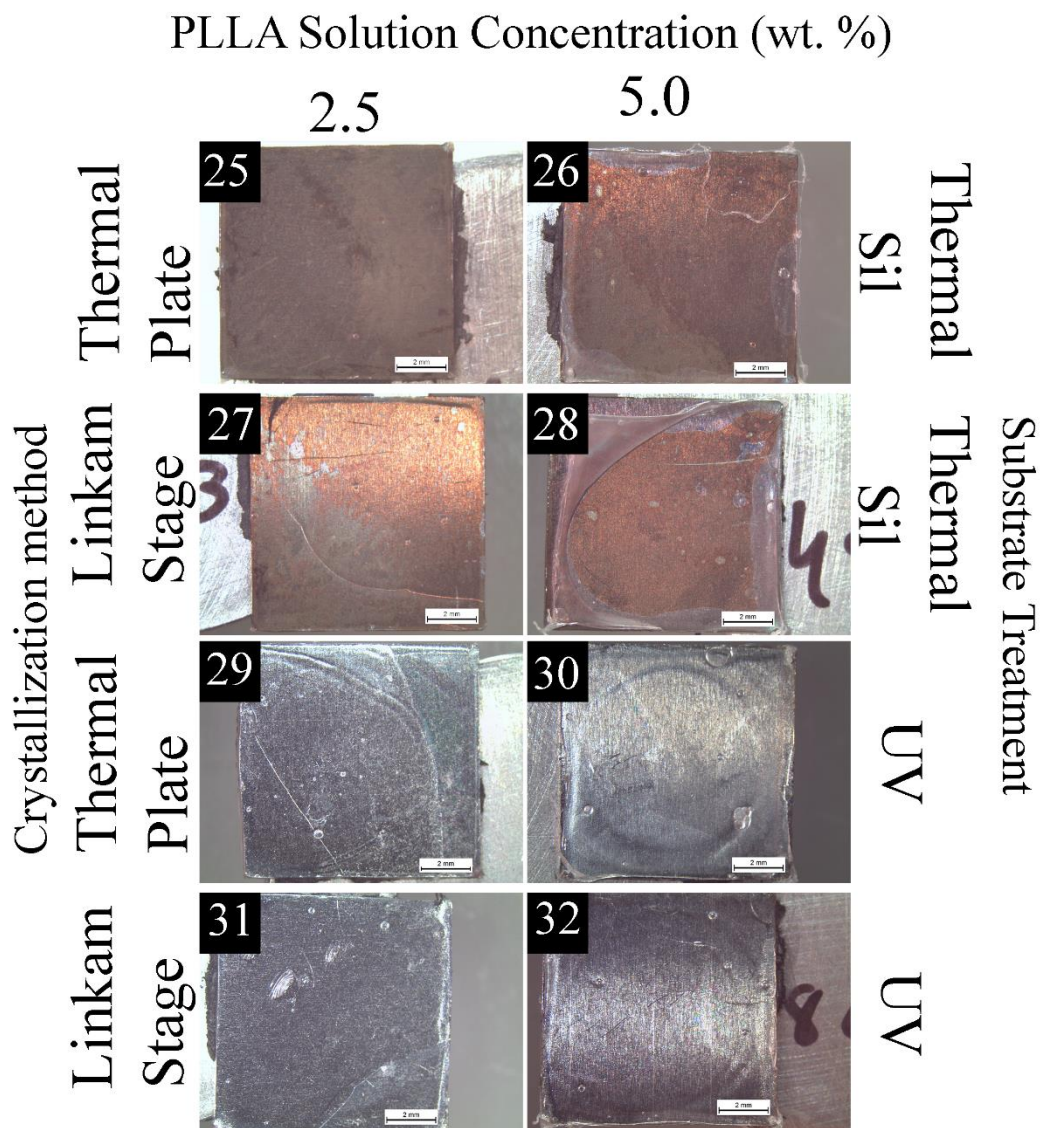


Figure 35. Thermally treated and UV treated substrates with PLLA films crystallized at 120°C for 60 minutes under different parameters observed on the stereo microscope.

The morphology of the different was also analysed by SEM, the obtained micrographs are shown below. The micrographs of the samples crystallized in the thermal plate and Linkam stage for 3 minutes at 180°C followed by 45 minutes at 120°C using cooling rates of 2.5,5.0 or 10°C/min can be seen in **Figures 36 and 37.** below.

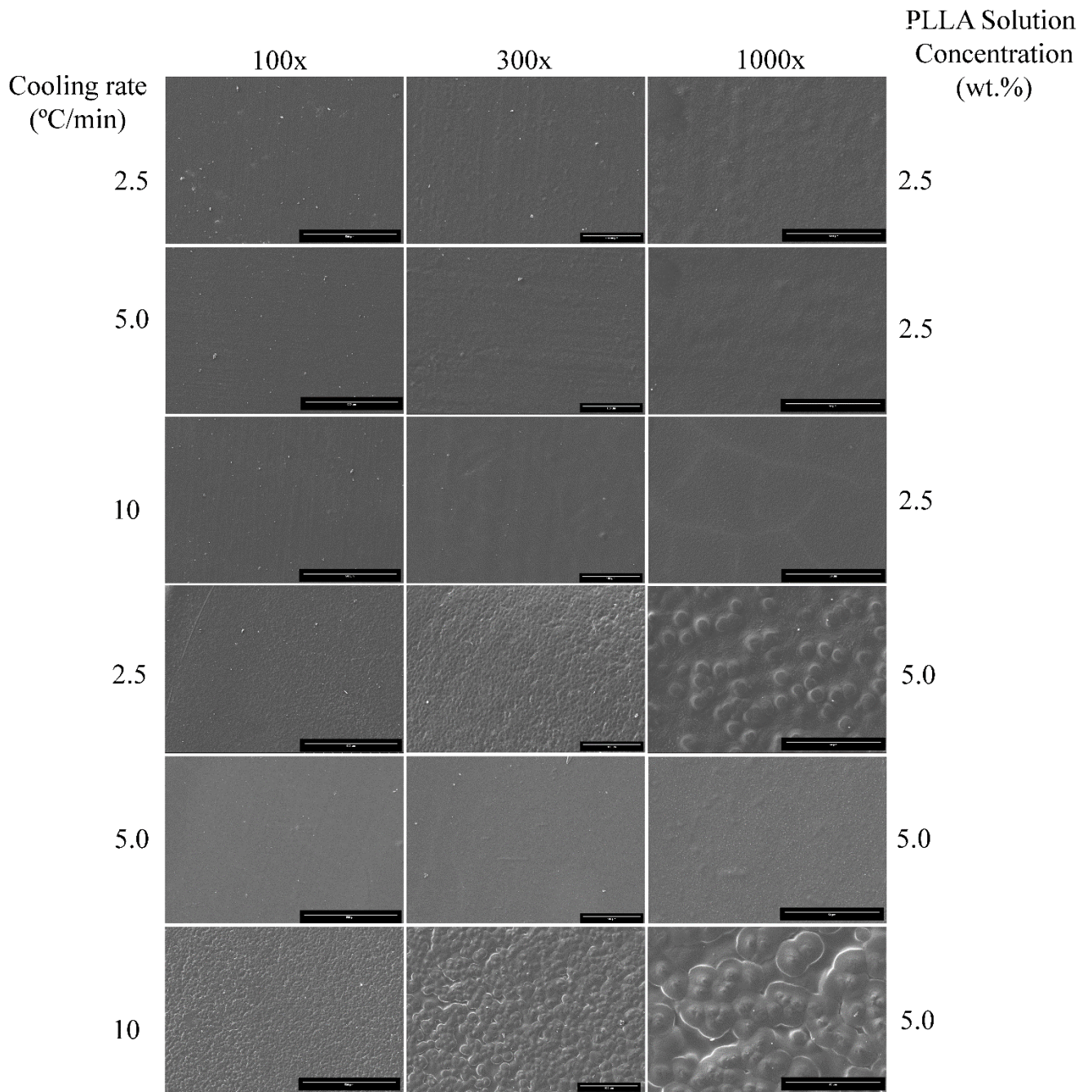


Figure 36 - SEM micrographs with different magnifications of the thermally treated and silanized samples crystallized in the Linkam stage for 3 minutes at 180°C followed by 45 minutes at 120°C with different magnifications, using cooling rates of 2.5,5.0 and 10°C/min.

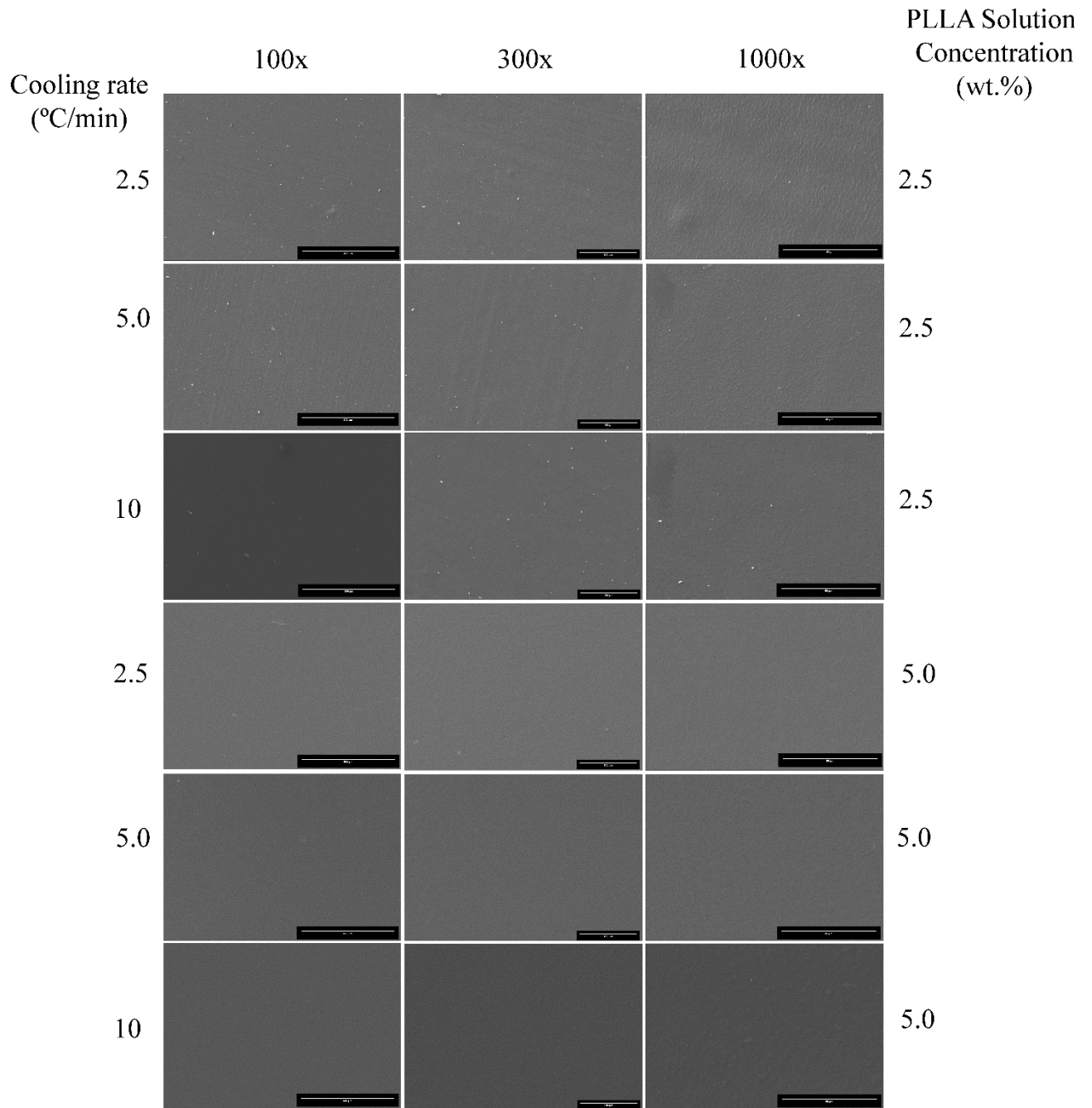


Figure 37. SEM micrographs of the UV treated samples crystallized in the Linkam stage for 3 minutes at 180°C followed by 45 minutes at 120°C with different magnifications, using cooling rates of 2.5,5.0 and 10°C/min

For the samples subjected to thermal treatment crystallized in Linkam using a solution concentration of 2.5 wt.% while the surface appears to be smooth at low magnifications at higher magnifications it is possible to observe small bumps.

However, in the thermally treated samples crystallized in Linkam in which 5.0 wt% solution was used it is possible to observe formation of larger bumps, with swirls around them. The surface looks more textured at lower magnifications, and it is possible to observe the larger bumps at higher magnifications, there does not seem to be a correlation between the size of the bumps and the cooling rate since they are larger in the 10°C/min then 2.5°C/min then 5°C/min

For UV, the morphology seems the same as the thermally treated substrates for 2.5 concentration, however for 5.0 the samples seem to present a smooth surface with some bumps visible at higher magnifications, however they are only present in small quantities when compared to other samples.

The micrographs of the samples crystallized in Linkam using cooling rates of 0.5 and 20°C can be seen in **Figure 38. and 39.**

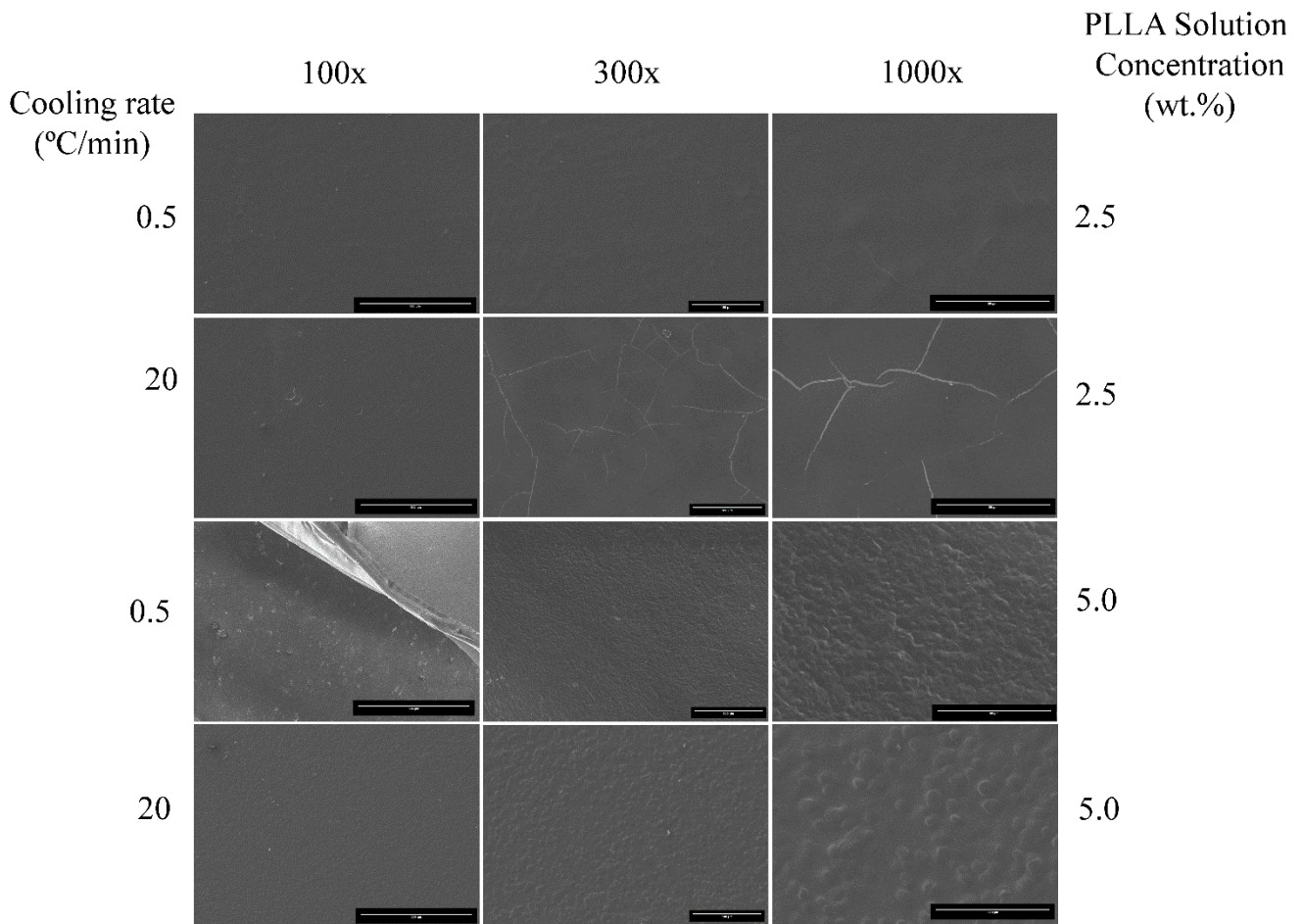


Figure 38. - SEM micrographs of the thermally treated and silanized samples crystallized in the Linkam stage for 3 minutes at 180°C followed by 45 minutes at 120°C with different magnifications, using cooling rates of 0.5 and 20°C/min

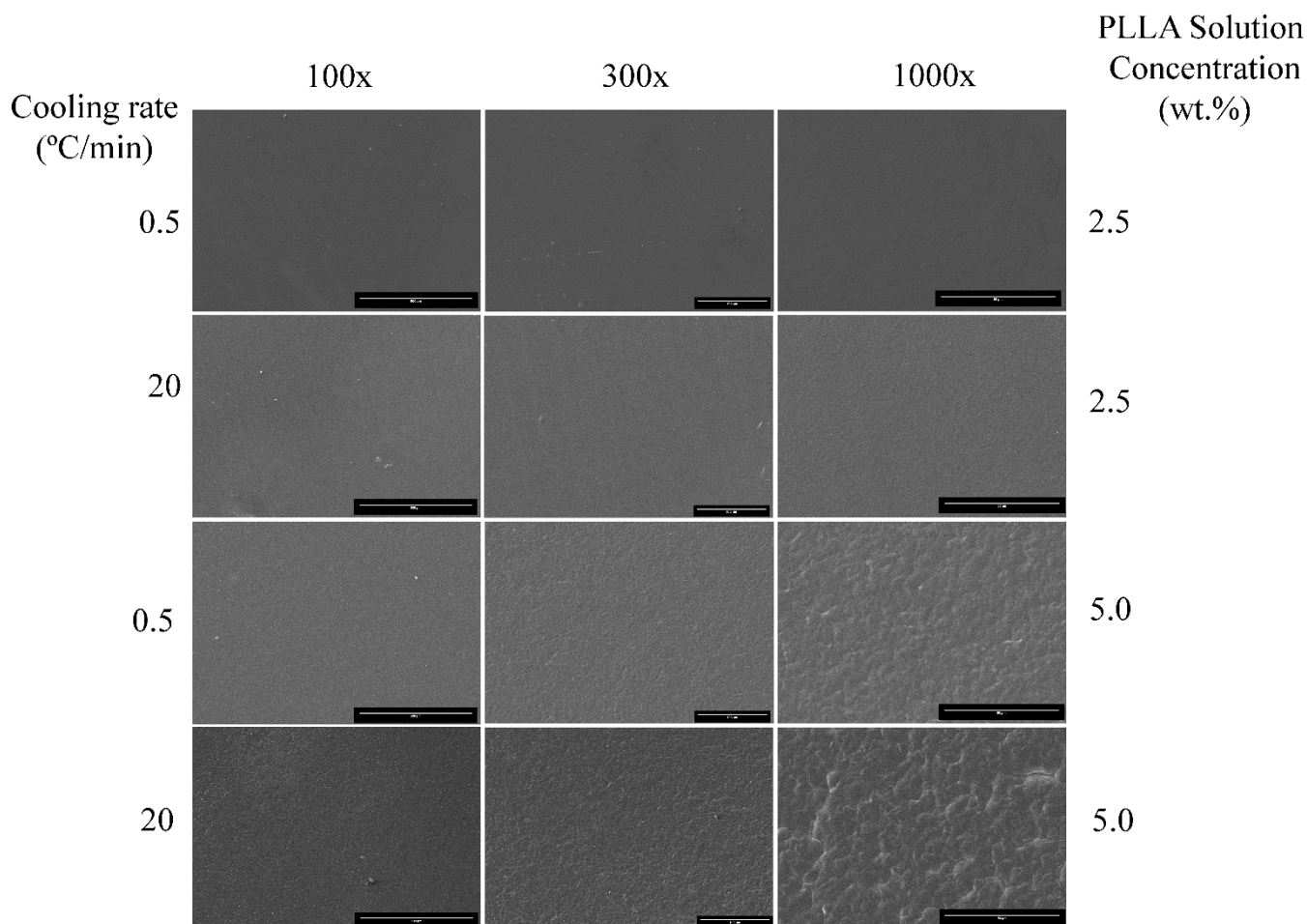


Figure 39. SEM micrographs of the UV treated samples crystallized in the Linkam stage for 3 minutes at 180°C followed by 45 minutes at 120°C with different magnifications, using cooling rates of 0.5 and 20°C/min

For the cooling rates of 0.5 and 20°C/min the thermally treated samples seem to present a smooth surface with some cracks, these cracks are mainly present in the samples cooled at 20°C/min with some being visible in the 0.5°C/min cooling rate, for the samples with films prepared with the solution with 5.0 wt.% the morphology seem to be similar to the other PLLA films with a lot of bumps showing for the 0.5°C cooling rate sample, while bumps are also present in the 20°C/min sample they are much smaller in size not conferring a lot of texture to sample's surface.

The samples treated with UV and cooled at 0.5 and 20 °C do not seem to show any differences in topography compared to other UV 2.5 wt.% samples, showing some small bumps, in the films prepared with 5.0 solution there seem to be an increase with roughness

associated with the appearance of irregular features, these seem to be bigger in the sample cooled at 20°C/min.

All the samples crystallized at 180°C for 3 minutes followed by 120°C for 45 minutes on the heating plate present spherulites, with thermally treated and silanized samples presenting larger spherulites however the samples that were subjected to UV and silanization presented bigger spherulites than the sample that was only UV treated. The size of the spherulites also seem to be influenced by the concentration of the solution used to prepare the film with higher concentration. It also seems that is possible to find a higher number of spherulites on the thermally treated samples this might be due to its surface improving the formation of nucleus. The micrographs of the samples crystallized on the heating plate can be seen in **Figure 40**.

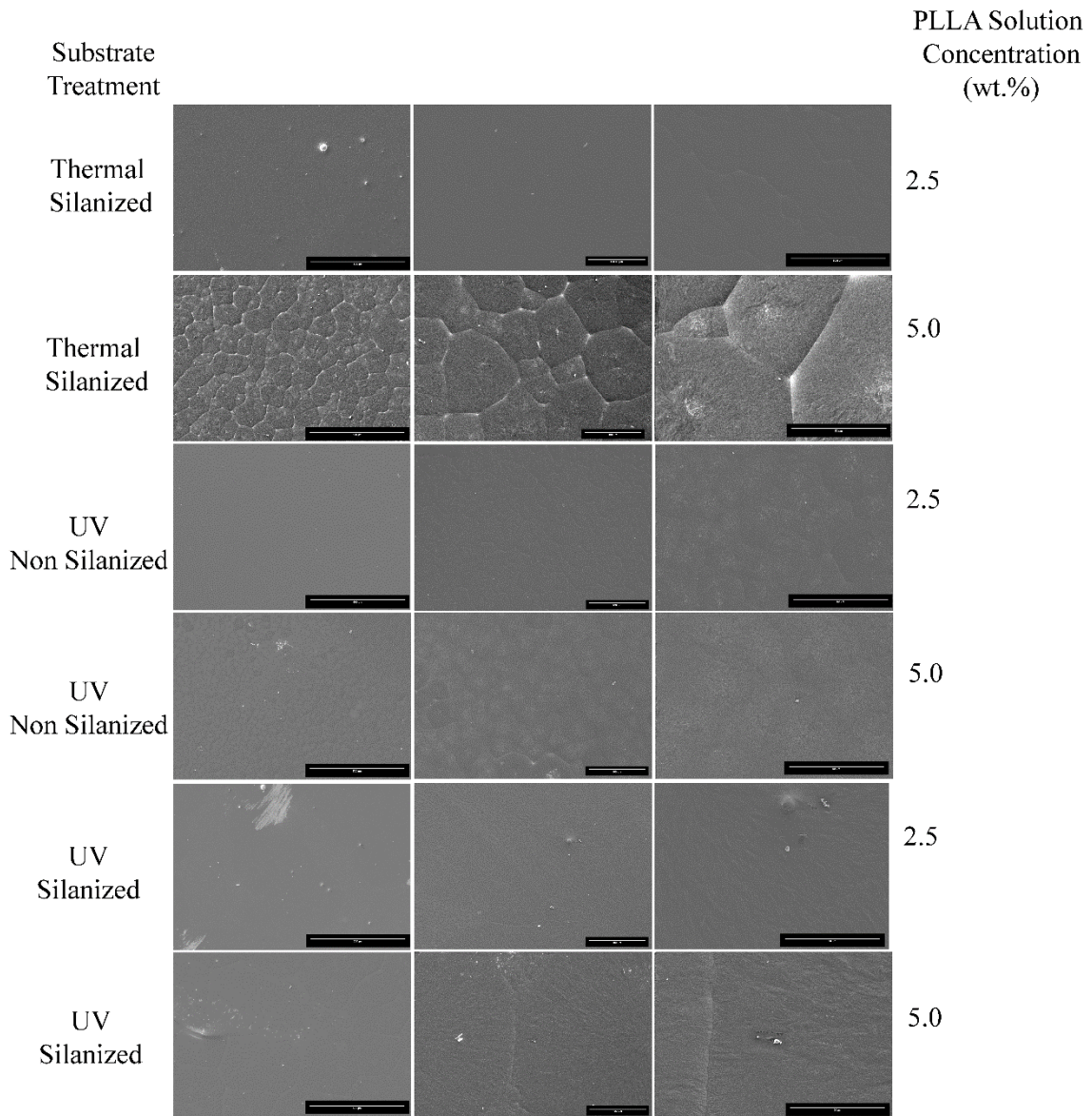


Figure 40. SEM micrographs of the thermally treated and silanized samples and UV treated samples crystallized in the thermal plate for 3 minutes at 180°C followed by 45 minutes at 120°C with different magnifications, using a cooling rate of 5. °C/min

The micrographs of the samples crystallized at 120°C for 60 minutes can be seen in **Figure 41. and 42.**

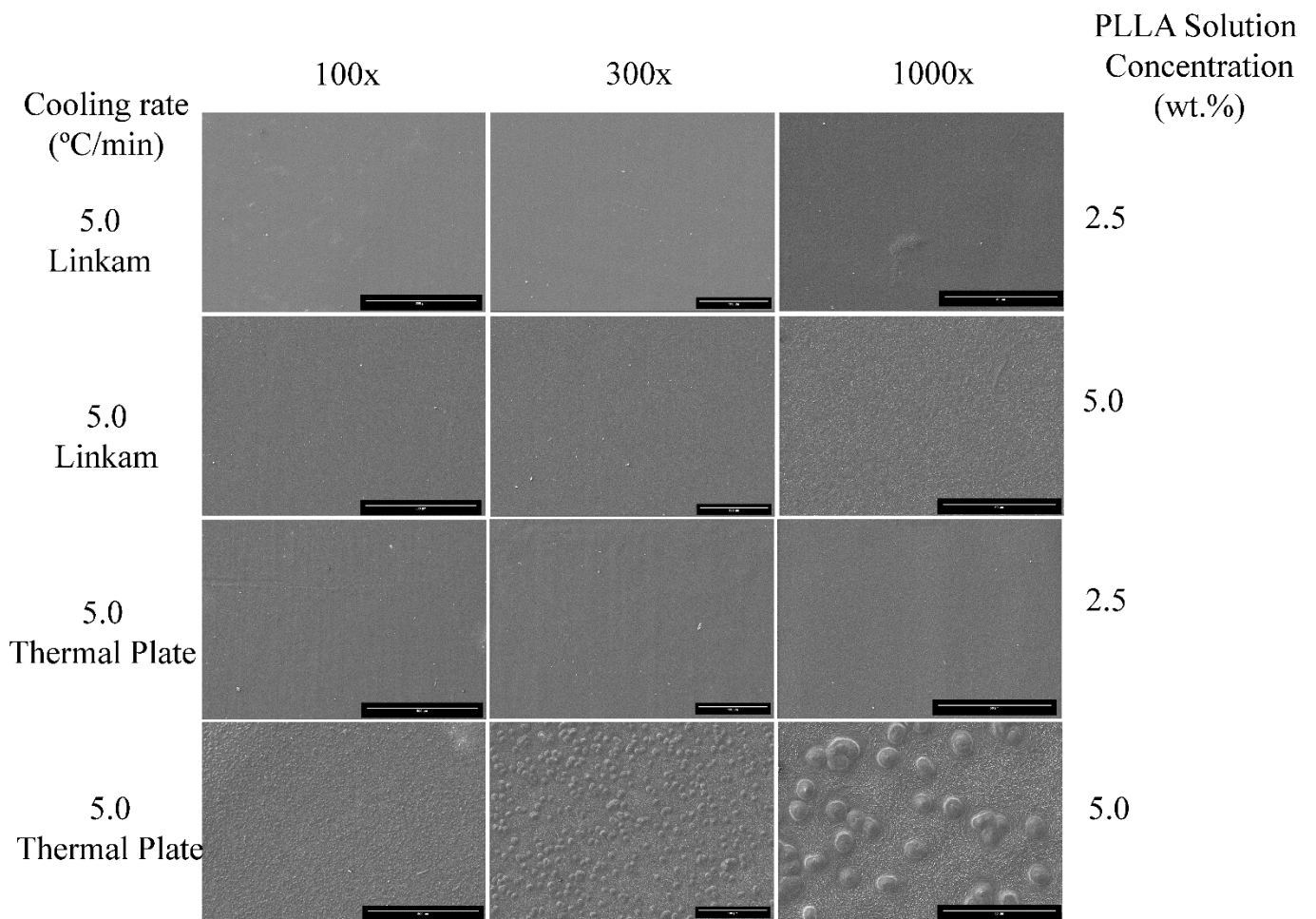


Figure 41. SEM micrographs of the thermally treated and silanized samples crystallized in the Linkam stage for 60 minutes at 120°C with different magnifications, using cooling rates of 5. °C/min

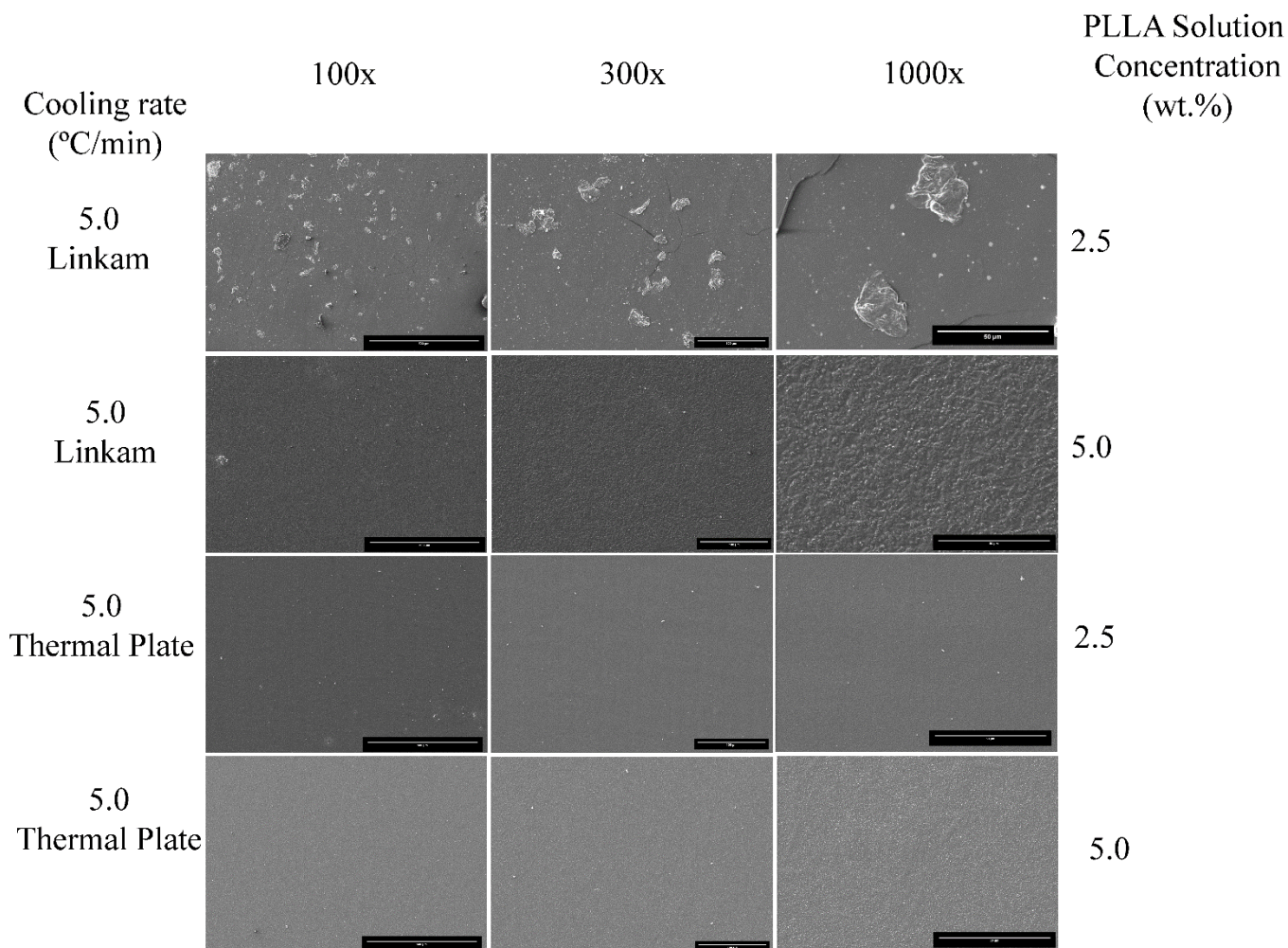


Figure 42. SEM micrographs of the thermally treated and silanized samples crystallized in the Linkam stage for 60 minutes at 120°C with different magnifications, using cooling rates of 5. °C/min

The samples crystallized at 120°C for 60 minutes and subjected to thermal treatment seem to show a smooth surface with the appearance of pore like structures when seen at higher magnifications, this is true for both the samples crystallized in Linkam or in the thermal plate, except for the film prepared with the 5.0% concentration crystallized at the thermal plate which seems to show the bump structure seen before in 5.0 wt.% concentration samples. The samples treated with UV and crystallized in the Linkam stage show cracks in the film for the 2.5 wt.% solution and what seems to be wrinkled film, while the 5.0 film shows small bumps although in here they seem to be more densely packaged.

In the samples crystallized in the thermal plate there seems to be the porous structure seen before for the 2.5% sample while for the 5.0% there seem to be again the appearance of very small bumps.

Overall, there seem to be 4 kinds of morphologies observed, small bumps, large bumps, irregular features and spherulites, while the morphology of the films don't seem to be influenced by the cooling rate it seems to affect the size of the formed features. The main factors influencing the topography of the samples seem to be the crystallization method and the chosen temperatures.

To further analyse the effect of the substrate on crystallization a thermally treated a silanized sample and a UV treated and silanized sample were analysed in AFM, the results are shown in **Figure 43**.

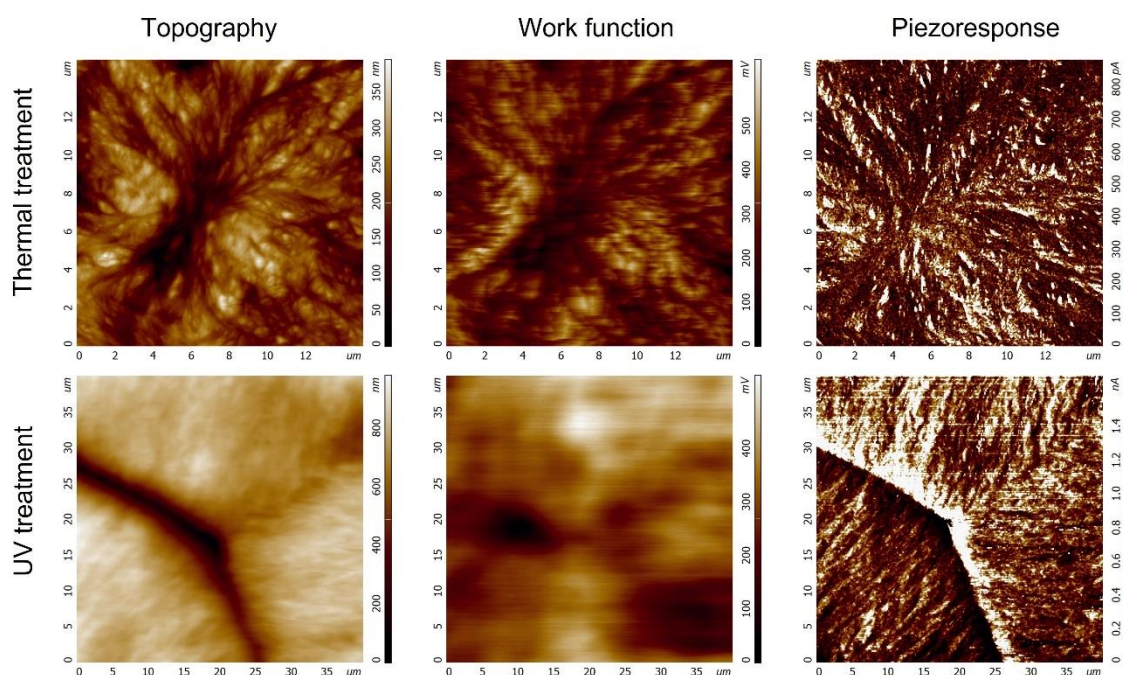


Figure 43. AFM topography, work function scans and piezoelectric response acquired on 316L SS pre-treatment (UV and Thermal) followed by silanization and crystallization on the heating plate using a heating rate of 5°C/min and a cooling rate of 5°C/min.

It is possible to verify a difference in size of the spherulites of the thermally treated and UV treated substrates with the spherulites presenting a bigger size on the UV treated one. The work function of the substrates also seems different with UV presenting a more uniform work function, while in the thermally treated substrate the work function seems to be

influenced by the morphology. The piezoelectric response seems similar in both the samples, looking to be aligned with the spherulite fibres.

4.5.PLLA films adhesion

In order to test the effectiveness of the pre-treatment methods and silanization process the samples were subjected to the crosshatch tape test in order to determine its adhesion. For that a hatch shape was cut into PLLA films crystallized or amorphous in different substrates and then peeled off using tape.

Firstly, tests were performed in both thermally treated and silanized and UV treated and silanized substrates, as well as untreated substrates, with both amorphous PLLA and PLLA films crystallized at 180°C for 3 minutes and 120°C for 45 minutes.

The obtained results are present in **Figure 44**.

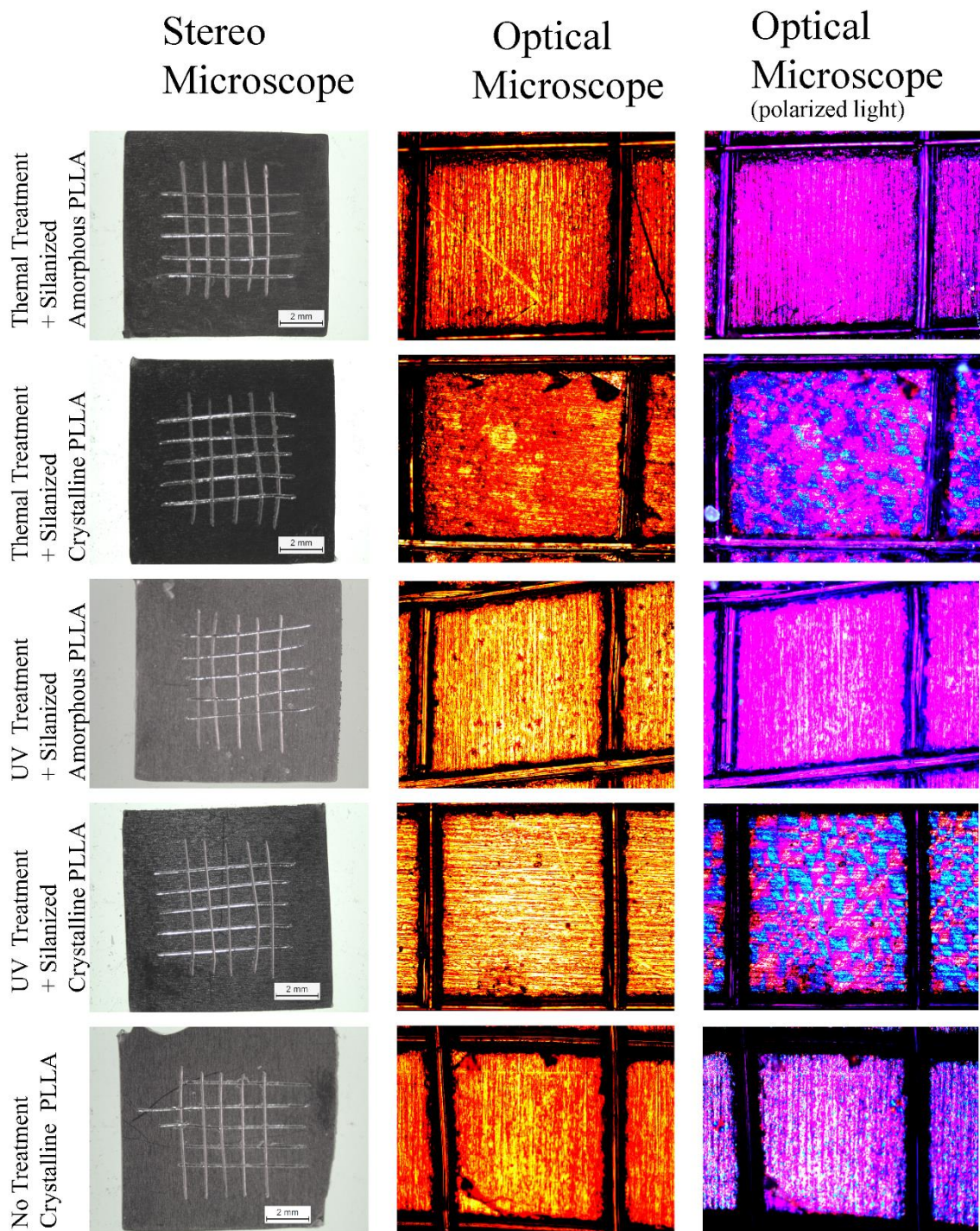


Figure 44 Images of substrates subjected to Thermal and UV treatment followed by silanization and a Pristine 316L SS with PLLA films after being subjected to the cross-hatch tape test, the samples were analysed with a stereo microscope with an ampliation of 8x (left), optical microscope with an ampliation of 20x (middle) and optical microscope with polarized light (right).

In all the cases where amorphous films were used no adhesion was shown. This is possible to observe in the stereo microscope pictures by looking at the edges of the cuts in

the substrates, if observed closely it is possible to observe the clean edges while in the samples with crystalline PLLA it is possible to observe contours around the edges in the spots where the PLLA broke off. Meanwhile it is possible to further confirm this observation by looking at the polarized micrographs in which the samples with amorphous films only show a purple colour corresponding to the metallic substrate, while in the samples with crystalline PLLA it is possible to observe a blue colour along with the purple colour, this occurs due to the fact that spherulites or other crystalline structures that might form during the PLLA crystallization are observable with an optical microscope under polarized light[76].

While amorphous films showed no adhesion in silanized substrates, all of them being 0B, the crystalline films showed good adhesion in general. The adhesion of these films seems significantly better than that of the amorphous films. Overall the treated substrates showing better adhesion than that of the untreated substrate with the Thermal and UV treated and silanized substrates being a 5B, even though the adhesion was slightly better on the UV treated substrate since the thermal displayed more loose corners. In the untreated substrate it was possible to observe that whole edges of the film had come out and that more corners of the film in the squares came off or was starting to peel, with the final result being a 4B.

The results of these tests suggest that the crystallization of the film might play a much bigger role than the surface treatment in the adhesion of the film.

To better determine the effect that the silanization process had on the adhesion thermally treated and silanized samples and UV treated samples both silanized and non-silanized were used in an adhesion test where the adhesion of the film was tested after different periods of time including 0, 2, 7 and 14 days the samples were then analysed under the stereo microscope, the obtained results are displayed in **Figure 45**.

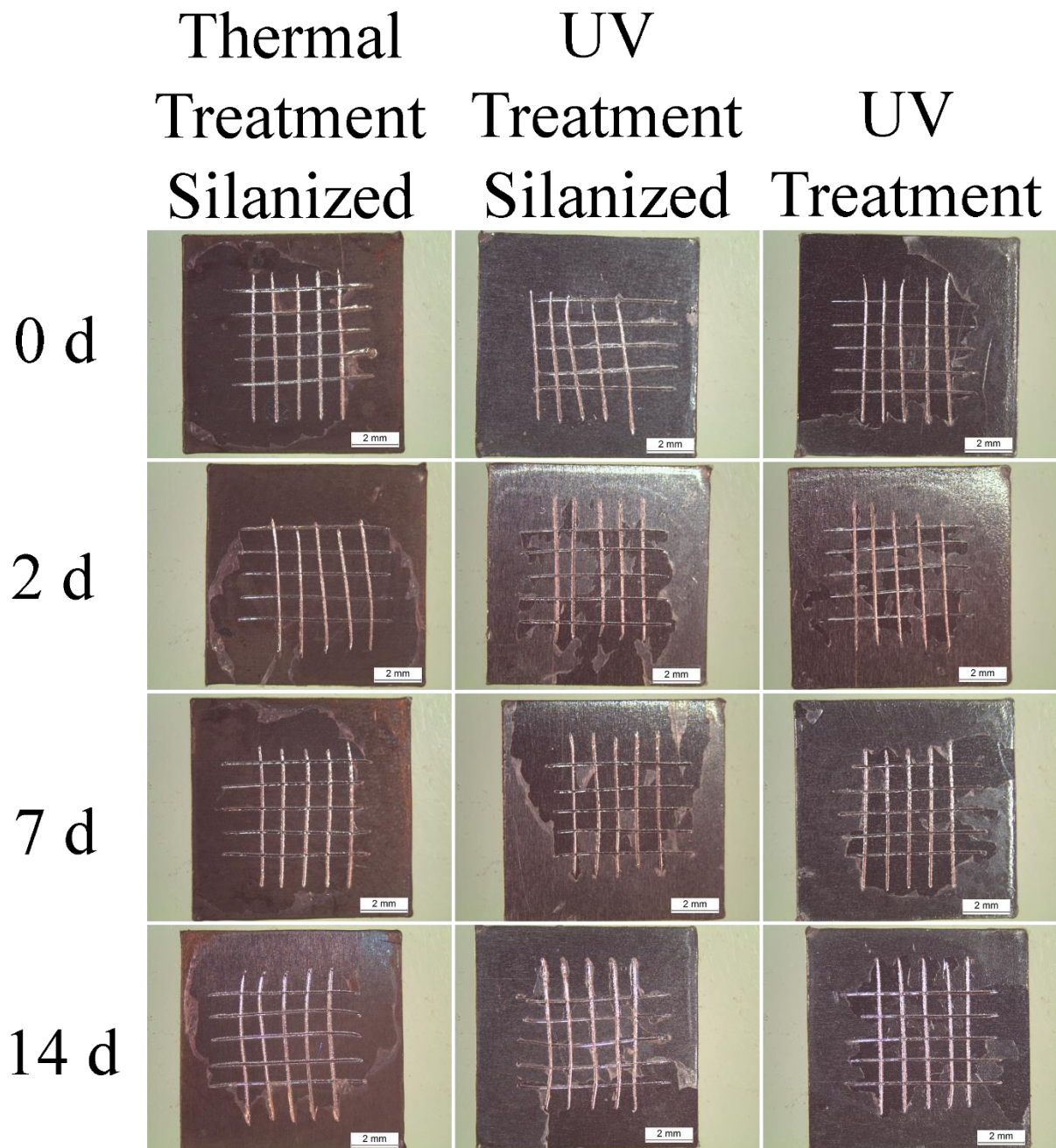


Figure 45. Stereo microscope images of 316L SS substrates with deposited PLLA films and crystallized. The samples were subjected to different pre-treatments: Thermal with silanization, UV with silanization and UV without-silanization. The cross hatch tape test was then performed after 0, 2, 7 or 14 days, in order to evaluate the evolution of the film adhesion with the time.

Looking at these pictures it is possible to observe differences in the adhesion between the different methods of treating the substrate and over time.

At $t = 0d$ it is possible to observe different results from what was obtained in the previous tests, with both the thermal treated and silanized substrate and the UV substrate with no silanization showing a weak adhesion of the film causing almost all of it to come out with both results being 0B, even though more film remained on the substrate on the thermally treated. The UV treated and silanized substrate presented good adhesion with almost all of the film staying on the substrate after the tape test. UV treated and silanized

After two days it was possible to notice a decrease in the film adhesion in both the UV treated substrates while the thermally treated one still showed little to no adhesion. The UV treated and silanized substrates seem to grade at 1B while the non silanized one is graded 2B. By comparing these two results it seems that the adhesion in substrates without silanization is comparable to that of the silanized substrates after two days. The thermally treated substrate continues to show little to no adhesion still being 0B.

One week after the crystallization the thermally treated substrate continues to show no adhesion, still grading at 0B. Meanwhile both the UV treated substrates presented a decrease in adhesion with the silanized one presenting better results grading at 2B while the non-silanized one grades at 1B.

After two weeks the thermally treated substrate still does not present adhesion continuing to grade a 0B. Meanwhile it is possible to observe a great difference between both UV substrates with silanization and without silanization with the silanized one presenting a classification of 3B and the non-silanized one presenting a result of 1B.

The results of the thermally treated substrate seem to go against the results previously obtained in the first adhesion test, however this result can be influenced by differences in the crystallization, since this is a very variable process depending on the conditions it occurs in. This discrepancy in results can also be caused by uneven pressure applied between when performing the cuts for the tape test, or when applying pressure to the tape.

Analysing all the obtained results it is possible to conclude that crystallization seems to be the main factor of adhesion, especially after the first few days after adhesion. After one week has passed the adhesion decays in both silanized and non-silanized samples, however the samples that are silanized seem to have a better adhesion with the passage of time. Although the crosshatch tape test simulates conditions very different from those in the physiological environment, in accordance with this results the better solution seems to be

to use UV treated and silanized substrates in order to have better adhesion over a longer period of time.

4.6.Polarization of PLLA films by Corona discharge

In order to test the effect of polarization in PLLA films PLLA films on a thermally treated and silanized substrate were subjected to polarization using corona discharge varying the electric field from -5kV to -10kV to see the effect of the magnitude of the electric field.

Analysing the substrates, it is possible to notice that there was the formation of spherulites across all the substrates these spherulites had a considerable size being observable with the stereo microscope as shown in **Figure 46**.

The samples were also analysed under the optical microscope with polarised light, which is also shown in **Figure 46**. When looking at the samples the present spherulites in the polarized samples they all seem to present the same orientation, however this was still observed before the polarization of the samples, so the polarization does not seem influence the spherulites orientation. When looking at the samples poled with electric fields of -6kV or less display dark spots on both the spherulites and the amorphous part of the film. The concentration of those spots seems to increase as the voltage increases, with the highest number of dark spots being on the film polarized with -10kV.

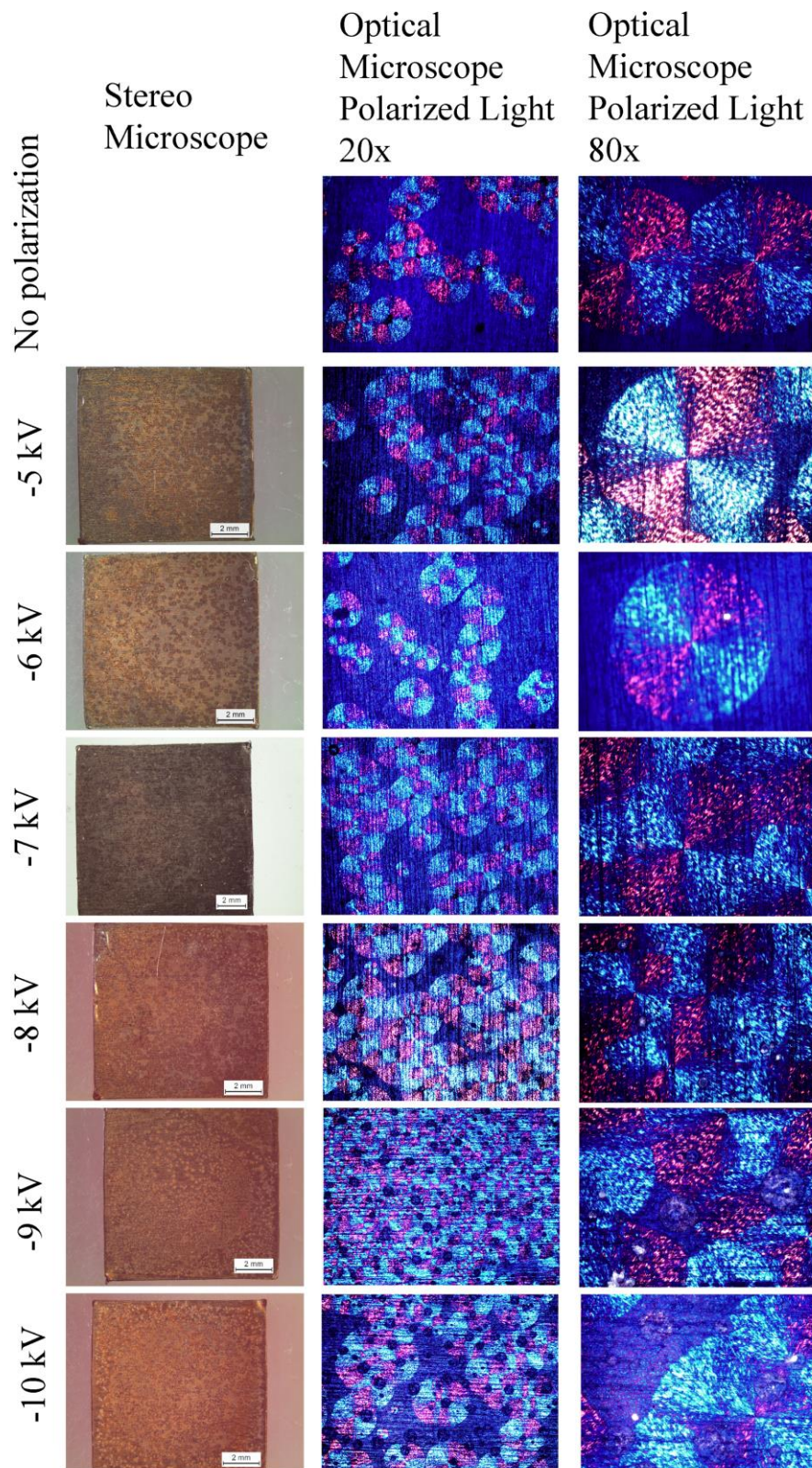


Figure 46. Crystalline PLLA films deposited on thermally treated and silanized 316L SS substrates that were polarized with electrical fields of different voltages. The samples were then observed under the stereo microscope and optical microscope with polarized light.

The polarized samples were then analysed using SEM. The results are shown in **Figure 47**.

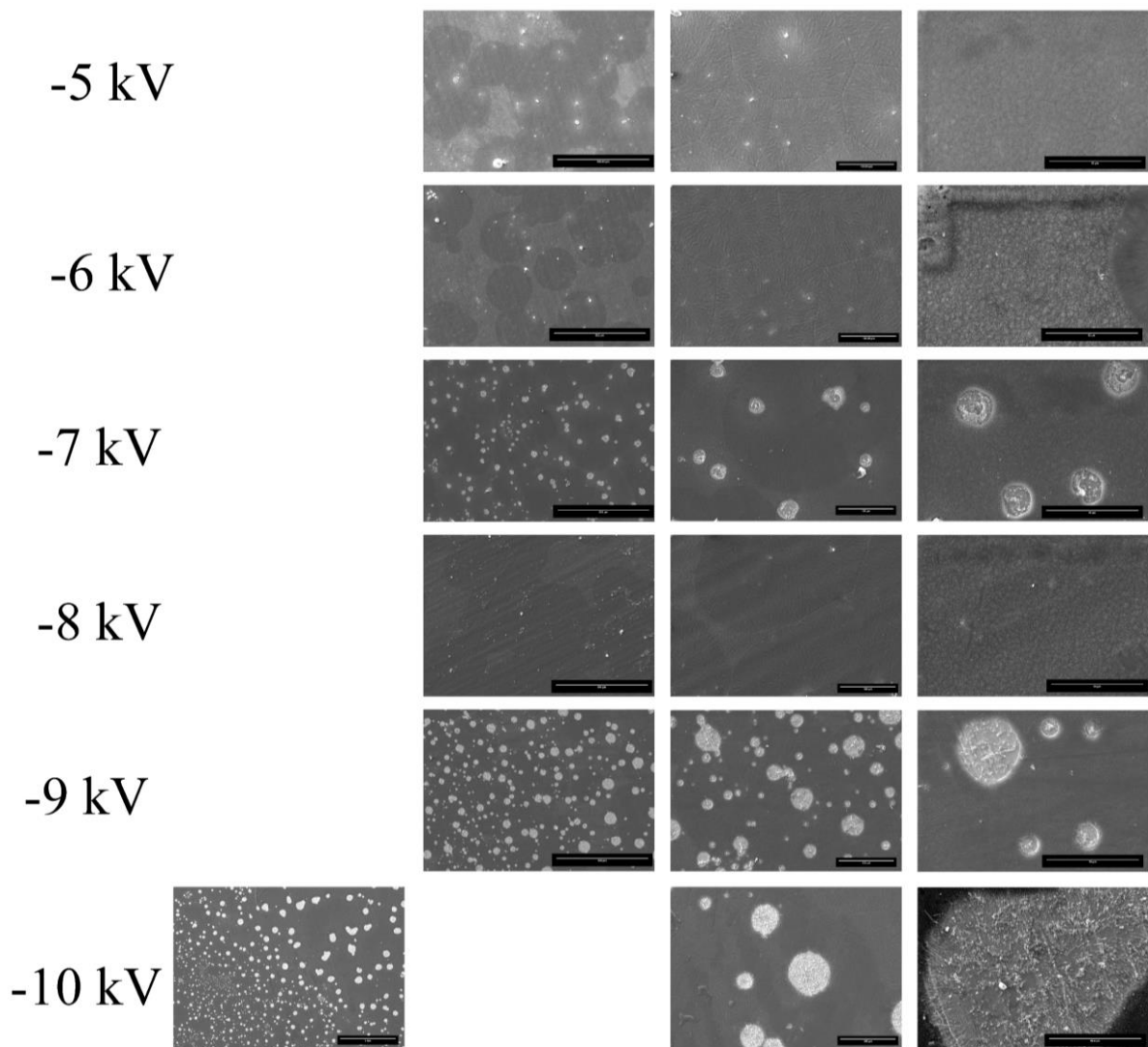


Figure 47. Crystalline PLLA films deposited on thermally treated and silanized 316L SS substrates that were polarized with electrical fields of different voltages. The samples were then observed in SEM under different magnifications.

In the SEM analysis it is possible to verify that those spots correspond to damage caused to the films by the electric field applied. In SEM it is also possible to notice changes in the topography of the films increasing its roughness this effect is especially noticeable in the films polarized with less intense electric fields, being the most visible in the films polarized with the electric fields of -5kV, -6kV and -7 kV.

Overall, the polarization process with electric fields of -8kV or more seem to damage the film significantly, The polarization process also seems to cause changes in the amorphous part of the film, meanwhile changes on the spherulites or its orientation were noticed.

Thermally treated and silanized with PLLA films crystallized at 180°C for 3 minutes followed by 45 minutes at 120°C were polarized with an electric field of -5kV and sent to be used in cellular assays in order to assess the effect of polarization however due to time constraints it was not possible to finish the assays on time.

4.7. Simulated Body Fluid tests

Thermally treated and silanized samples without PLLA films (control), and with PLLA films crystallized at either 180°C for 3 minutes followed by 120°C for 45 minutes or crystallized at 120°C for 60 minutes were subjected to immersion in SBF for periods of 3, 7, 14 and 28 days. A pristine 316L SS substrate along with a thermally treated substrate without silanization were also immersed in SBF for 14 days.

After removing the samples from SBF and drying the solution's pH and the samples mass were measured. The obtained values are shown in Annex A. Analysing the values obtained before and after SBF immersion there does not seem to be any significant changes in either pH or mass values.

To further assess if any apatite structures had formed on the PLLA films the samples immersed to SBF were then analysed under SEM. The results are present below in **Figure 48, 49 and 50**.

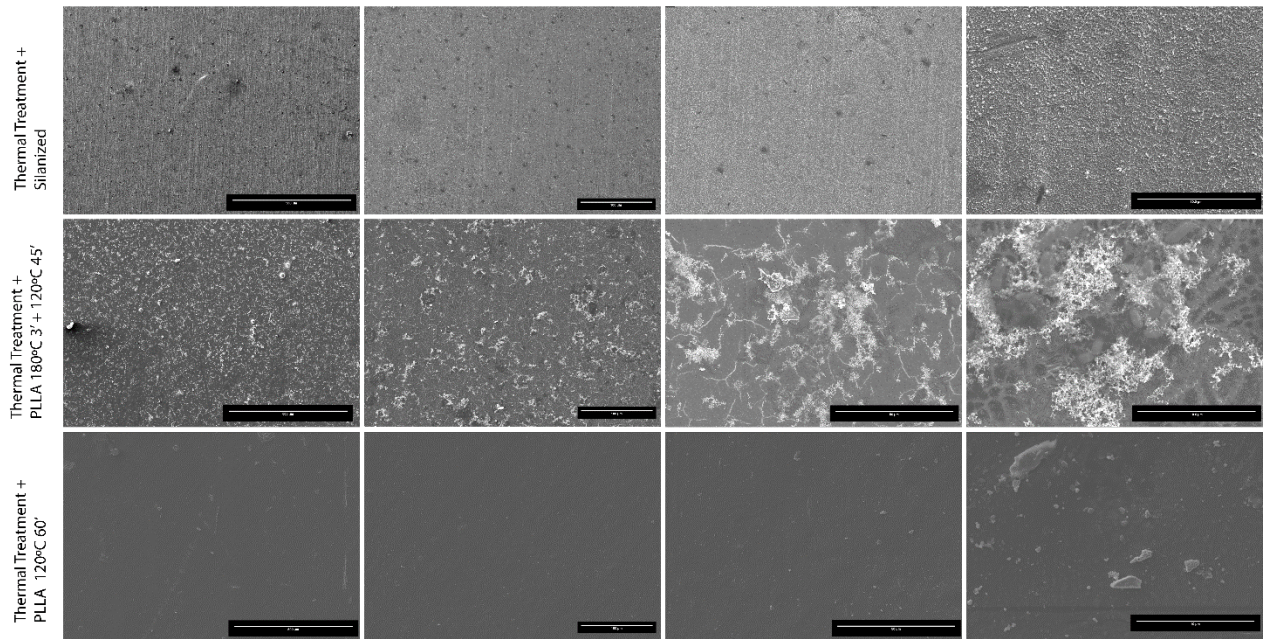


Figure 48. SEM micrographs with different magnifications of 316LSS substrates subjected to thermal treatment and silanized, without PLLA (top) and with PLLA crystallized at 180°C for 3 minutes followed by 45 minutes at 120°C (middle) and crystallized at 120°C for 60 minutes (bottom), after 3 days of immersion in SBF.

The thermally treated sample and silanized samples does not seem to show any apatite formation, when observed with higher magnifications of 1000x and 5000x it is possible to see crystals that formed in the surface of the sample along with the silanes. Through EDS analysis it was possible to confirm that those crystals were not apatite and are probably salts from the SBF solution that deposited in the sample.

In the samples crystallized at 180°C for 3 minutes and 120°C for 45 minutes, when looked at with magnifications of 100 and 300x it is possible to note the appearance of fiber like structures in the samples. When using higher magnifications it is possible to note that those structures are composed of agglomerates of granular structures, this structure seems to be apatite as this morphology has been reported for some apatites in the literature before[136], however it was not possible to confirm this by EDS since calcium and phosphorus were not found. When looking at the higher amplification micrographs it is also possible to note a fibre-like structures under the apatite, this structure is the crystalline PLLA, as it has been observed before on work done by the group previously[23], the reason why different structures of PLLA form during crystallization is still unclear.

The sample crystallized at 120°C for one hour seem to present a smooth surface without any noticeable structures originated from the PLLA crystallization. There do not seem to be the formation of any apatite structures in this film with some crystals being visible at higher magnifications, probably these are also salts that deposited from the solution into the sample as seen on the thermally treated and silanized sample.

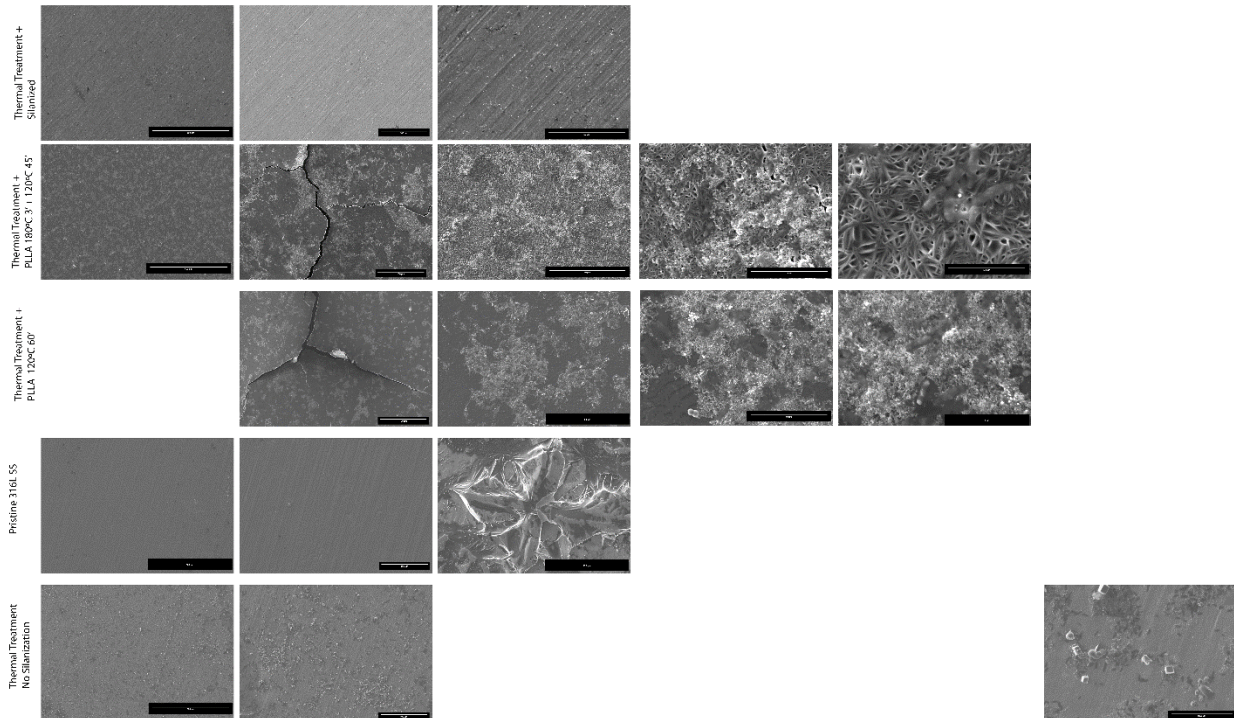


Figure 48. SEM micrographs with different magnifications of 316LSS substrates subjected to thermal treatment and silanized, without PLLA(TTS) and with PLLA crystallized at 180°C for 3 minutes followed by 45 minutes at 120°C (180) and crystallized at 120°C for 60 minutes (120); Pristine 316L SS (Pristine) and thermally treated 316L SS with no silanization (Thermal no Sil) after 14 days of immersion in SBF.

After 14 days there are no noticeable changes in the thermally treated and silanized samples.

In the samples crystallized at 180°C for 3 minutes followed by 120 °C for 45 minutes it is possible to notice a higher quantity of formed apatite, with the PLLA films still having the fibre-like morphology. It is also possible to observe the formation of the cracks on the film, this demonstrates that after 14 days it is possible to notice degradation of the PLLA film.

The sample crystallized at 120°C for 60 minutes continues to show a smooth topography. However, after 14 days it is possible to observe that apatite has started to form, and similarly

to the film crystallized at both 180 and 120°C it is also possible to verify that the film started to develop cracks, which are an indicative of degradation.

In both the pristine and thermally treated substrate only deposited salts were observed, and there were no signs of apatite formed. In the pristine substrate it was possible to observe damages to the surface in the higher magnifications.

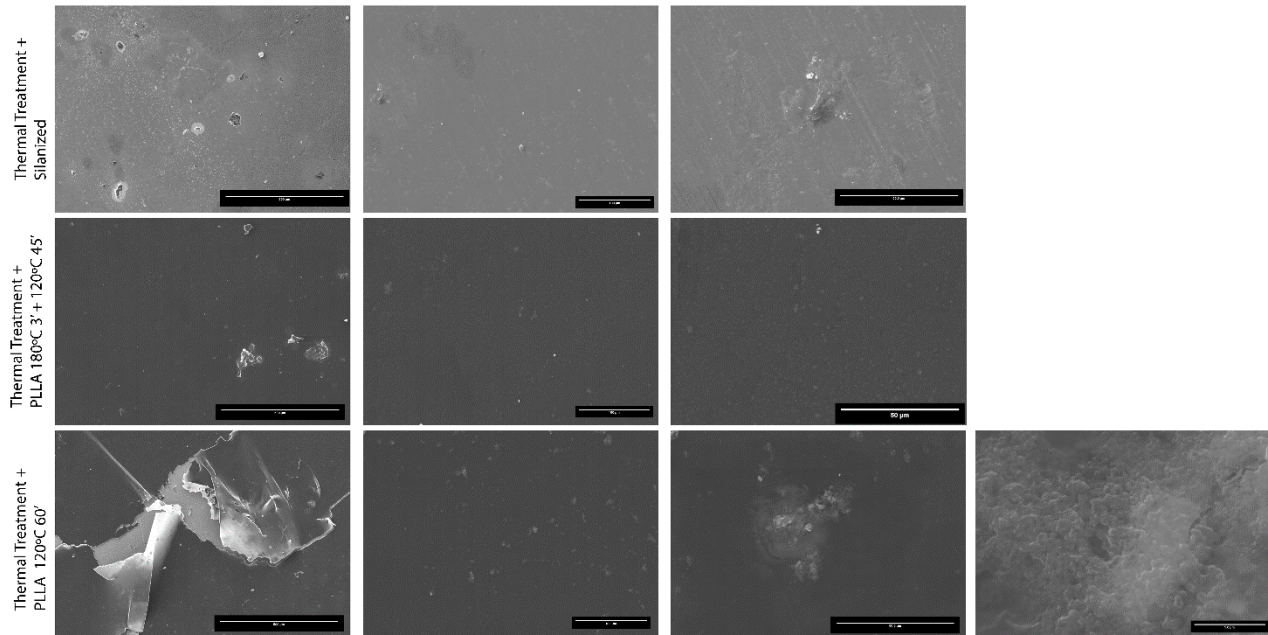


Figure 49. SEM micrographs with different magnifications of 316LSS substrates subjected to thermal treatment and silanized, without PLLA(top) and with PLLA crystallized at 180°C for 3 minutes followed by 45 minutes at 120°C (middle) and crystallized at 120°C for 60 minutes (bottom), after 28 days of immersion in SBF.

After 28 days no changes were observed in the thermally treated and silanized sample.

In the films with the PLLA films it is possible to notice damage to the film crystallized at 120°C for 60 minutes. The apatite structures seem to have mostly disappeared in these samples, however in the crystallized at 120°C for 60 minutes, when looking at it with a magnification of 1000x it was possible to find a structure resembling apatite, the structure was zoomed in using an ampliation of 30000x EDS was performed in the structure allowing to detect the presence of calcium and phosphorus confirming it is apatite.

It is possible to conclude that the produced PLLA films were indeed bioactive, causing the formation of apatite. After 14 days it was possible to observe that the films had started to suffer degradation.

Chapter 5

Conclusion and Future Works

Chapter 5 – CONCLUSION AND FUTURE WORKS

5.1. Conclusion

For this work the main goal was to develop a platform composed by a stainless steel 316L SS substrate and a PLLA thin film presenting piezoelectric properties with the possibility to further develop it into uses for bone implantation. Stainless steel was chosen since it is commonly used and approved to use in bone implants while PLLA was chosen due to its biodegradability, biocompatibility and more important its piezoelectricity which should present beneficial for the final use improving the bone regeneration process.

To continue with the previous work done in the project and as a way to improve the final result obtained the main focus of this work was to study how the different parameters, namely treatment of the substrate, PLLA solution concentration, crystallization method and crystallization temperatures affect the crystallinity and morphology of the PLLA films. This is of great importance since the crystallinity of a PLLA has a plethora of effects on the properties of the final film.

Characterization of the substrates after the different treatments showed differences between the thermal and UV treatment with the main different being the chromium oxide layer formed on top of the substrate after thermal treatment as observed in the FITR analysis. The thermal treatment showed to be more efficient in the formation of OH groups on the surface of the substrate as shown by contact angle however both methods showed themselves suitable for the subsequent silanization of the substrates. The success of the silanization process was confirmed by FTIR, SEM and EDS analysis, however it was shown that the pre-treatment of the substrate had very little effect in the final result.

The PLLA films were synthesized by depositing 3 layers of PLLA solution of concentration 2.5 wt.% or 5.0 wt.% on top of the metallic substrates, this was done via spin coating. The films were then subjected to different crystallization treatments on both thermal plate and Linkam stage.

For samples crystallized on the Linkam stage the samples that were thermally treated mostly show a smooth surface when observed at low magnifications, however at higher magnification is possible to note the formation of bumps that increase the surface roughness, a similar topography is observed in the UV treated samples, however there is not as much presence of bumps in this samples as there are in the thermally treated one. These bumps seem more prominent in films prepared with the 5.0 wt.% solution.

The films crystallized on the thermal plate present spherulites on its surface, with the size of the spherulites seeming bigger on the UV treated samples, silanization also seems to increase the size of the spherulites. In AFM it was possible to verify piezoelectric response in both thermally treated and UV treated samples, however this piezoelectric response seems to align with the spherulite's fibres. It is unclear the effect of other film morphologies in the piezoelectric response since it was not possible to analyse all the films due to time constraints.

Overall the samples crystallized at 120°C for 60 minutes seem to present a smooth topography of the PLLA film, with samples prepared with PLLA 2.5 wt.% solution presenting pore like structures while in samples prepared with 5.0 wt. % solution there seem to be an increase in the surface roughness.

Films prepared with the solution of higher concentration seem to originate more rougher film surfaces after crystallization, this is true for both the substrate pre-treatment methods. The main factors to influence the film morphology seem to be the crystallization method, crystallization temperatures.

The crystallinity degree of the different samples was assessed via XRD, it was possible to obtain crystallinity degrees between 27.16 and 72.05. The crystallinity degree seems to increase when the sample is crystallized on the Linkam stage compared to the thermal plate, with the lower cooling rates allowing for a greater crystallinity degree. The samples crystallized at 180°C for 3 minutes followed by 120 °C for 45 minutes show significantly better crystallinity than those that were crystallized at 120°C for 60 minutes, with UV seemingly allowing for higher degrees of crystallization.

Crystallization also seems to play a significant role in the early stages of the metallic substrate to polymer film adhesion, with amorphous films showing no adhesion to the substrate independently of the treatment. While crystallinity seem to be the main factor to influence adhesion shortly after the film is deposited, silanization however seems to be fundamental for long term adhesion with adhesion after 14 days being significantly better in silanized samples.

The polarization of the samples was also studied where it was concluded that electrical fields lower than 7kV cause damage to the sample.

The samples were subjected to SBF tests where it was possible to observe sign of apatite formation after 3 days with apatite structures being visible after 14 days. The apatite is barely visible after 28 days indicating that it might have dissolved back into the solution.

Overall the prepared PLLA platforms show promising results for applications in bone tissue engineering with the possibility of tailoring the final result by changing the crystallization conditions of the sample.

5.2. Future Works

In vitro studies using samples crystallized at 180°C for 3 minutes followed by 120°C for 45 minutes and samples crystallized at 120°C for 60 minutes, both polarized and non-polarized are undergoing at the University of Porto (UP), in collaboration with the project “Advanced BioMEMs for Tissue Engineering: Applications in Hard Tissues (BioMEMs)”. Upon positive results in the in vitro studies the samples with best results will be chosen to further be used in in-vivo tests.

The influence of the crystallinity degree and crystalline morphologies of the samples in both the piezoelectric and biological response is also an interesting direction to take, since it would allow to tailor the final properties of the implant in accordance to its desired use.

References

- [1] R. Agarwal and A. J. García, “Biomaterial strategies for engineering implants for enhanced osseointegration and bone repair,” *Adv. Drug Deliv. Rev.*, vol. 94, pp. 53–62, 2015.
- [2] H. Qu, H. Fu, Z. Han, and Y. Sun, “Biomaterials for bone tissue engineering scaffolds: A review,” *RSC Adv.*, vol. 9, no. 45, pp. 26252–26262, 2019.
- [3] K. Zhang *et al.*, “Advanced smart biomaterials and constructs for hard tissue engineering and regeneration,” *Bone Res.*, vol. 6, no. 1, 2018.
- [4] B. Priyadarshini, M. Rama, Chetan, and U. Vijayalakshmi, “Bioactive coating as a surface modification technique for biocompatible metallic implants: a review,” *J. Asian Ceram. Soc.*, vol. 7, no. 4, pp. 397–406, 2019.
- [5] R. Quarto and P. Giannoni, “Bone tissue engineering: Past-present-future,” *Methods Mol. Biol.*, vol. 1416, pp. 21–33, 2016.
- [6] I. Fukada, E. y Yasuda, “On the Piezoelectric of Bone,” *Journal of the Physical Society of Japan*, vol. 12, no. 10. 1957.
- [7] F. C. Kao, P. Y. Chiu, T. T. Tsai, and Z. H. Lin, “The application of nanogenerators and piezoelectricity in osteogenesis,” *Sci. Technol. Adv. Mater.*, vol. 20, no. 1, pp. 1103–1117, 2019.
- [8] B. Miara, E. Rohan, M. Zidi, and B. Labat, “Piezomaterials for bone regeneration design - Homogenization approach,” *J. Mech. Phys. Solids*, vol. 53, no. 11, pp. 2529–2556, 2005.
- [9] G. Narayanan, V. N. Vernekar, E. L. Kuyinu, and C. T. Laurencin, “Poly (Lactic Acid)-Based Biomaterials for Orthopaedic Regenerative Engineering Graphical abstract HHS Public Access,” *Adv. Drug Deliv. Rev.*, vol. 107, pp. 247–276, 2016.
- [10] H. J. Oh *et al.*, “Fabrication of piezoelectric poly(l-lactic acid)/BaTiO₃ fibre by the melt-spinning process,” *Sci. Rep.*, vol. 10, no. 1, pp. 1–12, 2020.
- [11] E. Fukada, “Piezoelectricity of biopolymers,” *Biorheology*, vol. 32, no. 6, pp. 593–609, 1995.
- [12] E. Fukada, “Fukada (1998) - New piezoelectric polymers,” *Jpn. J. Appl. Phys.*, vol. 37, no. 5B, pp. 2775–2780, 1998.
- [13] A. H. Rajabi, M. Jaffe, and T. L. Arinzeh, “Piezoelectric materials for tissue regeneration: A review,” *Acta Biomater.*, vol. 24, no. July, pp. 12–23, 2015.
- [14] J. Jacob, N. More, K. Kalia, and G. Kapusetti, “Piezoelectric smart biomaterials for bone and cartilage tissue engineering,” *Inflamm. Regen.*, vol. 38, no. 1, pp. 1–11, 2018.
- [15] C. Ochoa-Putman and U. K. Vaidya, “Mechanisms of interfacial adhesion in metal-polymer composites - Effect of chemical treatment,” *Compos. Part A Appl. Sci. Manuf.*, vol. 42, no. 8, pp. 906–915, 2011.
- [16] C. Lambaré, P. Y. Tessier, F. Poncin-Epaillard, and D. Debarnot, “Plasma functionalization and etching for enhancing metal adhesion onto polymeric substrates,” *RSC Adv.*, vol. 5, no. 77, pp. 62348–62357, 2015.
- [17] J. Friedrich, R. Mix, and S. Wettmarshausen, “A new concept for Adhesion promotion in metal-polymer systems by introduction of covalently bonded spacers at the interface,” *J. Adhes. Sci. Technol.*, vol. 22, no. 10–11, pp. 1123–1143, 2008.
- [18] P. Molitor, V. Barron, and T. Young, “Surface treatment of titanium for adhesive bonding to polymer composites: A review,” *Int. J. Adhes. Adhes.*, vol. 21, no. 2, pp. 129–136, 2001.
- [19] T. M. Bedair, Y. Cho, Y. K. Joung, and D. K. Han, “Biodegradable polymer brush as nanocoupled interface for improving the durability of polymer coating on metal surface,” *Colloids Surfaces B Biointerfaces*, vol. 122, pp. 808–817, 2014.
- [20] Y. H. Ding, M. Floren, and W. Tan, “Mussel-inspired polydopamine for bio-surface functionalization,” *Biosurface and Biotribology*, vol. 2, no. 4, pp. 121–136, 2016.
- [21] J. Liu *et al.*, “Significant Enhancement of the Adhesion between Metal Films and Polymer Substrates by UV-Ozone Surface Modification in Nanoscale,” *ACS Appl. Mater. Interfaces*, vol. 8, no. 44, pp. 30576–30582, 2016.
- [22] A. Magueta, “Biomedical microelectromechanical (BioMEMs) systems to tissue engineering: applications in hard tissues Dissertação,” Universidade de Aveiro, 2018.
- [23] S. O. Ferreira, “Electrical and biological characterization of PLLA-316L stainless steel electromechanical devices for bone tissue engineering.,” 2020.

- [24] M. V. Branquinho *et al.*, “In vitro and in vivo characterization of PLLA-316L stainless steel electromechanical devices for bone tissue engineering—A preliminary study,” *Int. J. Mol. Sci.*, vol. 22, no. 14, 2021.
- [25] N. Su *et al.*, “Bone function, dysfunction and its role in diseases including critical illness,” *Int. J. Biol. Sci.*, vol. 15, no. 4, pp. 776–787, 2019.
- [26] Liliana Polo-Corrales, M. Latorre-Esteves, and J. E. Ramirez-Vick, “Scaffold Design for Bone Regeneration,” *Bone*, vol. 23, no. 1, pp. 1–7, 2014.
- [27] A. Mansour, M. A. Mezour, Z. Badran, and F. Tamimi, “Extracellular matrices for bone regeneration: A literature review,” *Tissue Eng. - Part A*, vol. 23, no. 23–24, pp. 1436–1451, 2017.
- [28] B. Li and T. Webster, “Orthopedic biomaterials progress in biology, manufacturing, and industry perspectives,” *Orthop. Biomater. Prog. Biol. Manuf. Ind. Perspect.*, pp. 1–496, 2018.
- [29] L. Polo-Corrales, M. Latorre-Esteves, and J. E. Ramirez-Vick, “Scaffold design for bone regeneration. Journal of nanoscience and nanotechnology,” vol. 14, no. 1, pp. 15–56, 2014.
- [30] U. Mittwoch, *Human anatomy*, vol. 261, no. 5559, 1976.
- [31] D. J. Hadjidakis and I. I. Androulakis, “Bone remodeling,” *Ann. N. Y. Acad. Sci.*, vol. 1092, pp. 385–396, 2006.
- [32] L. J. Raggatt and N. C. Partridge, “Cellular and molecular mechanisms of bone remodeling,” *J. Biol. Chem.*, vol. 285, no. 33, pp. 25103–25108, 2010.
- [33] J. A. Siddiqui and N. C. Partridge, “Physiological bone remodeling: Systemic regulation and growth factor involvement,” *Physiology*, vol. 31, no. 3, pp. 233–245, 2016.
- [34] A. Oryan, S. Alidadi, A. Moshiri, and N. Maffulli, “Bone regenerative medicine: Classic options, novel strategies, and future directions,” *J. Orthop. Surg. Res.*, vol. 9, no. 1, pp. 1–27, 2014.
- [35] M. Elbadawi, J. Meredith, L. Hopkins, and I. Reaney, “Progress in Bioactive Metal and, Ceramic Implants for Load- Bearing Application,” *Adv. Tech. Bone Regen.*, 2016.
- [36] W. G. Billotte, “Ceramic biomaterials,” *Biomater. Princ. Appl.*, vol. 124, pp. 21–54, 2002.
- [37] M. Roy, A. Bandyopadhyay, and S. Bose, *Ceramics in Bone Grafts and Coated Implants*. Elsevier Inc., 2017.
- [38] M. Niinomi, M. Nakai, and J. Hieda, “Development of new metallic alloys for biomedical applications,” *Acta Biomater.*, vol. 8, no. 11, pp. 3888–3903, 2012.
- [39] Q. Chen and G. A. Thouas, “Metallic implant biomaterials,” *Mater. Sci. Eng. R Reports*, vol. 87, pp. 1–57, 2015.
- [40] N. Shayesteh Moghaddam *et al.*, “Metals for bone implants: safety, design, and efficacy,” *Biomanufacturing Rev.*, vol. 1, no. 1, pp. 1–16, 2016.
- [41] J. R. Davis, *Handbook of Materials for Medical Devices*. 2003.
- [42] B. Love, “Chapter 7 - Metallic biomaterials,” *Biomater. A Syst. Approach to Eng. Concepts*, pp. 159–184, 2017.
- [43] K. Prasad *et al.*, “Metallic biomaterials: Current challenges and opportunities,” *Materials (Basel)*, vol. 10, no. 8, 2017.
- [44] S. Stephen, “Arthroprosthetic cobaltism associated with metal on metal hip implants,” *BMJ*, vol. 344, no. 7840, p. 2847, 2012.
- [45] R. F. Canadas, S. Pina, A. P. Marques, J. M. Oliveira, and R. L. Reis, *Cartilage and Bone Regeneration-How Close Are We to Bedside?* Elsevier Inc., 2016.
- [46] R. D. Rusk, “Science,” *Educ. Forum*, vol. 15, no. 1, pp. 119–120, 1950.
- [47] H. Larry L and P. Julia M, “Third-generation biomedical materials,” *Science (80-.)*, vol. 295, no. February, pp. 1014–1017, 2002.
- [48] C. Gao, S. Peng, P. Feng, and C. Shuai, “Bone biomaterials and interactions with stem cells,” *Bone Res.*, vol. 5, no. October, pp. 1–33, 2017.
- [49] M. M. Stevens, “Biomaterials for bone Materials that enhance bone regeneration have a wealth of potential,” *Bone*, vol. 11, no. 5, pp. 18–25, 2008.
- [50] K. Sharma, M. A. Mujawar, and A. Kaushik, “State-of-Art Functional Biomaterials for Tissue Engineering,” *Front. Mater.*, vol. 6, no. July, pp. 1–10, 2019.

- [51] J. Adhikari, P. Saha, and A. Sinha, *Surface modification of metallic bone implants-Polymer and polymer-assisted coating for bone in-growth*. Elsevier Ltd, 2018.
- [52] A. Mayeen and N. Kalarikkal, *Development of ceramic-controlled piezoelectric devices for biomedical applications*. Elsevier Ltd., 2018.
- [53] A. Jbaily and R. W. Yeung, “Piezoelectric devices for ocean energy: a brief survey,” *J. Ocean Eng. Mar. Energy*, vol. 1, no. 1, pp. 101–118, 2015.
- [54] K. E. Pennywitt, *Robotic Tactile Sensing.*, vol. 11, no. 1. 1986.
- [55] P. M. Vilarinho, Y. Rosenwaks, and A. Kingon, *Scanning Probe Microscopy: Characterization, Nanofabrication and Device Application of Functional Materials*. Kluwer Academic Publishers, 2005.
- [56] S. O. R. Moheimani and a J. Fleming, *Piezoelectric transducers for vibration control and damping (advances in industrial control)*. 2006.
- [57] “Fundamentals of Piezo Technology.” [Online]. Available: <https://www.physikinstrumente.com/en/technology/piezo-technology/fundamentals/>. [Accessed: 27-Oct-2021].
- [58] C. Halperin *et al.*, “Piezoelectric effect in human bones studied in nanometer scale,” *Nano Lett.*, vol. 4, no. 7, pp. 1253–1256, 2004.
- [59] N. Setter *et al.*, “Ferroelectric thin films: Review of materials, properties, and applications,” *J. Appl. Phys.*, vol. 100, no. 5, 2006.
- [60] M. Sharifzadeh Baei and M. Esmaeili, “Fabrication of biodegradable polymer nanocomposite from copolymer synthesized by C. necator for bone tissue engineering,” *World Appl. Sci. J.*, vol. 14, no. SPL ISS 3, pp. 106–111, 2011.
- [61] V. DeStefano, S. Khan, and A. Tabada, “Applications of PLA in modern medicine,” *Eng. Regen.*, vol. 1, no. April, pp. 76–87, 2020.
- [62] V. DeStefano, S. Khan, and A. Tabada, “Applications of PLA in modern medicine,” *Eng. Regen.*, vol. 1, no. April, pp. 76–87, 2020.
- [63] M. Savioli Lopes, A. L. Jardim, and R. Maciel Filho, “Poly (lactic acid) production for tissue engineering applications,” *Procedia Eng.*, vol. 42, pp. 1402–1413, 2012.
- [64] A. C. Vieira, J. C. Vieira, J. M. Ferra, F. D. Magalhães, R. M. Guedes, and A. T. Marques, “Mechanical study of PLA-PCL fibers during in vitro degradation,” *J. Mech. Behav. Biomed. Mater.*, vol. 4, no. 3, pp. 451–460, 2011.
- [65] S. Y. Lee, P. Valtchev, and F. Dehghani, “Synthesis and purification of poly(L-lactic acid) using a one step benign process,” *Green Chem.*, vol. 14, no. 5, pp. 1357–1366, 2012.
- [66] E. Fukada, “Piezoelectricity of biopolymers,” vol. 32, no. 6, pp. 593–609, 1995.
- [67] E. Fukada, “New piezoelectric polymers,” *Japanese J. Appl. Physics, Part 1 Regul. Pap. Short Notes Rev. Pap.*, vol. 37, no. 5 SUPPL. B, pp. 2775–2780, 1998.
- [68] Y. Ikada, Y. Shikinami, Y. Hara, M. Tagawa, and E. Fukada, “Enhancement of bone formation by drawn poly(L-lactide),” *J. Biomed. Mater. Res.*, vol. 30, no. 4, pp. 553–558, 1996.
- [69] J. F. Mano, J. L. Gómez Ribelles, N. M. Alves, and M. Salmerón Sanchez, “Glass transition dynamics and structural relaxation of PLLA studied by DSC: Influence of crystallinity,” *Polymer (Guildf.)*, vol. 46, no. 19 SPEC. ISS., pp. 8258–8265, 2005.
- [70] S. T. Hsu and Y. L. Yao, “Effect of film formation method and annealing on morphology and crystal structure of poly (L-Lactic Acid) films,” *J. Manuf. Sci. Eng. Trans. ASME*, vol. 136, no. 2, pp. 1–38, 2014.
- [71] M. L. Di Lorenzo, M. Cocca, and M. Malinconico, “Crystal polymorphism of poly(l-lactic acid) and its influence on thermal properties,” *Thermochim. Acta*, vol. 522, no. 1–2, pp. 110–117, 2011.
- [72] J. Zhang *et al.*, “Crystal modifications and thermal behavior of poly(L-lactic acid) revealed by infrared spectroscopy,” *Macromolecules*, vol. 38, no. 19, pp. 8012–8021, 2005.
- [73] H. Wang, J. Zhang, and K. Tashiro, “Phase Transition Mechanism of Poly(l-lactic acid) among the α , δ , and β Forms on the Basis of the Reinvestigated Crystal Structure of the β Form,” *Macromolecules*, vol. 50, no. 8, pp. 3285–3300, 2017.
- [74] M. C. Righetti, M. Gazzano, M. L. Di Lorenzo, and R. Androsch, “Enthalpy of melting of α' - and α -

- crystals of poly(L-lactic acid),” *Eur. Polym. J.*, vol. 70, pp. 215–220, 2015.
- [75] B. Crist and J. M. Schultz, “Progress in Polymer Science Polymer spherulites : A critical review,” *Prog. Polym. Sci.*, vol. 56, pp. 1–63, 2016.
- [76] C. Yu, Q. Xie, Y. Bao, G. Shan, and P. Pan, “Crystalline and spherulitic morphology of polymers crystallized in confined systems,” *Crystals*, vol. 7, no. 5, 2017.
- [77] G. Sun, L. T. Weng, J. M. Schultz, and C. M. Chan, “Formation of banded and non-banded poly(l-lactic acid) spherulites during crystallization of films of poly(l-lactic acid)/poly(ethylene oxide) blends,” *Polymer (Guildf.)*, vol. 55, no. 7, pp. 1829–1836, 2014.
- [78] Z. Yang, H. Peng, W. Wang, and T. Liu, “Crystallization behavior of poly(ϵ -caprolactone)/layered double hydroxide nanocomposites,” *J. Appl. Polym. Sci.*, vol. 116, no. 5, pp. 2658–2667, 2010.
- [79] Z. H. Zhou, X. P. Liu, Q. Q. Liu, and L. H. Liu, “Influence of temperature and time on isothermal crystallization of poly-L-lactide,” *Int. J. Polym. Mater. Polym. Biomater.*, vol. 57, no. 9, pp. 878–890, 2008.
- [80] Y. Wang and J. F. Mano, “Influence of melting conditions on the thermal behaviour of poly(l-lactic acid),” *Eur. Polym. J.*, vol. 41, no. 10, pp. 2335–2342, 2005.
- [81] H. M. Chen *et al.*, “Crystallization kinetics and melting behaviors of poly(l-lactide)/graphene oxides composites,” *Thermochim. Acta*, vol. 566, pp. 57–70, 2013.
- [82] Y. Li, C. Han, Y. Yu, L. Xiao, and Y. Shao, “Effect of content and particle size of talc on nonisothermal melt crystallization behavior of poly(l-lactide),” *J. Therm. Anal. Calorim.*, vol. 135, no. 4, pp. 2049–2058, 2019.
- [83] F. Awaja, M. Gilbert, G. Kelly, B. Fox, and P. J. Pigram, “Adhesion of polymers,” *Prog. Polym. Sci.*, vol. 34, no. 9, pp. 948–968, 2009.
- [84] K. B. Buhl, A. H. Agergaard, M. Lillethorup, J. P. Nikolajsen, S. U. Pedersen, and K. Daasbjerg, “Polymer brush coating and adhesion technology at scale,” *Polymers (Basel)*, vol. 12, no. 7, pp. 1–15, 2020.
- [85] ASTM International, “ASTM D907 - 15 - Standard Terminology of Adhesives,” *B. Stand.*, vol. 15.06, 2015.
- [86] E. Bertels, *Nano-Engineered Polymer-Steel Hybrids : Chemical and Physical Compatibilization*, no. December. 2014.
- [87] J. D. Venables, “Adhesion and durability of metal-polymer bonds,” *J. Mater. Sci.*, vol. 19, no. 8, pp. 2431–2453, 1984.
- [88] S. Kisin, *Adhesion Changes at Metal–Polymer Interfaces: Study of the Copper–(Acrylonitrile–Butadiene–Styrene) System*, vol. Philosophy, no. 2007. 2007.
- [89] “3-Aminopropyltriethoxysilane.” [Online]. Available: <https://pubchem.ncbi.nlm.nih.gov/compound/3-Aminopropyltriethoxysilane#section=Computed-Descriptors>.
- [90] M. Hoikkanen, M. Honkanen, M. Vippola, T. Lepistö, and J. Vuorinen, “Effect of silane treatment parameters on the silane layer formation and bonding to thermoplastic urethane,” *Prog. Org. Coatings*, vol. 72, no. 4, pp. 716–723, 2011.
- [91] R. G. Acres *et al.*, “Molecular structure of 3-aminopropyltriethoxysilane layers formed on silanol-terminated silicon surfaces,” *J. Phys. Chem. C*, vol. 116, no. 10, pp. 6289–6297, 2012.
- [92] J. P. Matinlinna, C. Y. K. Lung, and J. K. H. Tsoi, “Silane adhesion mechanism in dental applications and surface treatments: A review,” *Dent. Mater.*, vol. 34, no. 1, pp. 13–28, 2018.
- [93] P. Jussila, H. Ali-L Öytty, K. Lahtonen, M. Hirsimäki, and M. Valden, “Effect of surface hydroxyl concentration on the bonding and morphology of aminopropylsilane thin films on austenitic stainless steel,” *Surf. Interface Anal.*, vol. 42, no. 3, pp. 157–164, 2010.
- [94] T. Yoshioka, K. Tsuru, S. Hayakawa, and A. Osaka, “Preparation of alginic acid layers on stainless-steel substrates for biomedical applications,” *Biomaterials*, vol. 24, no. 17, pp. 2889–2894, 2003.
- [95] M. Inoue, M. Sasaki, Y. Katada, and T. Taguchi, “UV irradiation enhances the bonding strength between citric acid-crosslinked gelatin and stainless steel,” *Colloids Surfaces B Biointerfaces*, vol. 88, no. 1, pp. 260–264, 2011.
- [96] “No Title.” [Online]. Available:

- http://www.novascan.com/products/uv_ozone_cleaners_silicon_glass_wafers.php.
- [97] N. Sahu, B. Parija, and S. Panigrahi, “Fundamental understanding and modeling of spin coating process: A review,” *Indian J. Phys.*, vol. 83, no. 4, pp. 493–502, 2009.
- [98] M. D. Tyona, “A theoretical study on spin coating technique,” *Adv. Mater. Res.*, vol. 2, no. 4, pp. 195–208, 2013.
- [99] C. L. Sungyeap Hong, “An Overview of the Synthesis and Synthetic Mechanism of Poly (Lactic acid),” *Mod. Chem. Appl.*, vol. 02, no. 04, 2014.
- [100] C. P. Buckley, *Introduction to physical polymer science*, vol. 53, no. 2. 1993.
- [101] A. Sugita and S. Tasaka, “Electric-field-induced chain orientation in poly(L-lactic acid),” *J. Polym. Sci. Part B Polym. Phys.*, vol. 42, no. 24, pp. 4433–4439, 2004.
- [102] T. Fukuda, H. Matsuda, T. Kimura, T. Shiraga, M. Kato, and H. Nakanishi, “Improved method of corona poling for highly developed dipolar orientation,” *Polym. Adv. Technol.*, vol. 11, no. 8–12, pp. 583–588, 2000.
- [103] J. A. Giacometti, P. A. Ribeiro, and S. Carlos, “CORONA POLING OF A FERROELECTRIC POLYMER (PVDF),” vol. 4017, pp. 53–58.
- [104] R. N. Jana, A. Kumar, and C. Im, “Molecular orientation of polyurethane based liquid crystal polymers by corona poling,” *J. Macromol. Sci. Part A Pure Appl. Chem.*, vol. 46, no. 10, pp. 1001–1006, 2009.
- [105] N. Barroca, P. M. Vilarinho, A. L. Daniel-Da-Silva, A. Wu, M. H. Fernandes, and A. Gruverman, “Protein adsorption on piezoelectric poly(L-lactic) acid thin films by scanning probe microscopy,” *Appl. Phys. Lett.*, vol. 98, no. 13, 2011.
- [106] N. Barroca, P. M. Vilarinho, M. H. V. Fernandes, P. Sharma, and A. Gruverman, “Stability of electrically induced-polarization in poly (L-lactic) acid for bone regeneration,” *Appl. Phys. Lett.*, vol. 101, no. 2, pp. 1–5, 2012.
- [107] N. Barroca, M. H. V. Fernandes, and P. M. Vilarinho, “Electromechanically active Poly (L-lactic) acid based structures for regenerative medicine,” pp. 1–305, 2014.
- [108] V. Țucureanu, A. Matei, and A. M. Avram, “FTIR Spectroscopy for Carbon Family Study,” *Crit. Rev. Anal. Chem.*, vol. 46, no. 6, pp. 502–520, 2016.
- [109] G. Mani, *Surface properties and characterization of metallic biomaterials*. Elsevier Ltd, 2015.
- [110] S. Magalhães, B. J. Goodfellow, and A. Nunes, “FTIR spectroscopy in biomedical research: how to get the most out of its potential,” *Appl. Spectrosc. Rev.*, vol. 0, no. 0, pp. 1–39, 2021.
- [111] Ž. Mitić *et al.*, “Instrumental methods and techniques for structural and physicochemical characterization of biomaterials and bone tissue: A review,” *Mater. Sci. Eng. C*, vol. 79, pp. 930–949, 2017.
- [112] J. C. Che, *Characterization of Surfaces and Nanostructures Academic and Industrial Applications Characterization of Solid Materials and Heterogeneous Catalysts From Structure to Surface Reactivity Characterization Techniques for Polymer Nanocomposites Basic Concepts*. 2008.
- [113] J. Gomez-Herrero and R. Reifengerger, *Scanning Probe Microscopy*. 2005.
- [114] “Atomic Force Microscopy - Nanoscience Instruments.” [Online]. Available: <https://www.nanoscience.com/techniques/atomic-force-microscopy/#>.
- [115] “Atomic Force Microscopy - Nanoscience Instruments.” .
- [116] K. D. Jandt, “Developments and perspectives of scanning probe microscopy (SPM) on organic materials systems,” *Mater. Sci. Eng. R Reports*, vol. 21, no. 5–6, pp. 221–295, 1998.
- [117] A. Gruverman, “Piezoresponse Force Microscopy : Electromechanical Behavior at the Nanoscale,” vol. 34, no. September 2009, 2017.
- [118] E. Soergel, “Piezoresponse force microscopy (PFM),” *J. Phys. D. Appl. Phys.*, vol. 44, no. 46, 2011.
- [119] “Atomic Force Microscopy Modes & Technique | Park Systems.” [Online]. Available: <https://parksystems.com/park-afm-modes>.
- [120] “Contact Angle -Wikipedia.” [Online]. Available: https://en.wikipedia.org/wiki/Contact_angle. [Accessed: 28-Oct-2021].
- [121] R. S. Hebbar, A. M. Isloor, and A. F. Ismail, *Contact Angle Measurements*. Elsevier B.V., 2017.

- [122] P. Gill, T. T. Moghadam, and B. Ranjbar, "Differential scanning calorimetry techniques: Applications in biology and nanoscience," *J. Biomol. Tech.*, vol. 21, no. 4, pp. 167–193, 2010.
- [123] A. A. Bunaciu, E. gabriela Udriștioiu, and H. Y. Aboul-Enein, "X-Ray Diffraction: Instrumentation and Applications," *Crit. Rev. Anal. Chem.*, vol. 45, no. 4, pp. 289–299, 2015.
- [124] A. Pandey, S. Dalal, S. Dutta, and A. Dixit, "Structural characterization of polycrystalline thin films by X-ray diffraction techniques," *J. Mater. Sci. Mater. Electron.*, vol. 32, no. 2, pp. 1341–1368, 2021.
- [125] T. Kokubo and H. Takadama, "How useful is SBF in predicting in vivo bone bioactivity?," *Biomaterials*, vol. 27, no. 15, pp. 2907–2915, 2006.
- [126] ASTM, "ASTM D3359 - 17 Standard Test Methods for Rating Adhesion by Tape Test," *B. Stand.*, vol. 06.01, 2017.
- [127] I. Esih, V. Alar, and I. Juraga, "Influence of thermal oxides on pitting corrosion of stainless steel in chloride solutions," *Corros. Eng. Sci. Technol.*, vol. 40, no. 2, pp. 110–120, 2005.
- [128] B. M. Giuliano, R. M. Escribano, R. Martín-Doménech, E. Dartois, and G. M. M. Caro, "Interstellar ice analogs: Band strengths of H₂O, CO₂, CH₃OH, and NH₃ in the far-infrared region," *Astron. Astrophys.*, vol. 565, pp. 1–17, 2014.
- [129] G. Da Ponte, A. K. Ghosh, A. Kakaroglou, D. Van Hemelrijck, B. Van Mele, and B. Verheyde, "Adhesion improvement between epoxy and stainless steel using a silane coupling agent in an atmospheric plasma process," *Plasma Process. Polym.*, vol. 12, no. 4, pp. 347–361, 2015.
- [130] A. M. Oje and A. A. Ogwu, "Chromium oxide coatings with the potential for eliminating the risk of chromium ion release in orthopaedic implants," *R. Soc. Open Sci.*, vol. 4, no. 7, 2017.
- [131] T. Ohmi, Y. Nakagawa, M. Nakamura, A. Ohki, and T. Koyama, "Formation of chromium oxide on 316L austenitic stainless steel," *J. Vac. Sci. Technol. A Vacuum, Surfaces, Film.*, vol. 14, no. 4, pp. 2505–2510, 1996.
- [132] N. Eustathopoulos, N. Sobczak, A. Passerone, and K. Nogi, "Measurement of contact angle and work of adhesion at high temperature," *J. Mater. Sci.*, vol. 40, no. 9–10, pp. 2271–2280, 2005.
- [133] N. S. K. Gunda, M. Singh, L. Norman, K. Kaur, and S. K. Mitra, "Optimization and characterization of biomolecule immobilization on silicon substrates using (3-aminopropyl)triethoxysilane (APTES) and glutaraldehyde linker," *Appl. Surf. Sci.*, vol. 305, pp. 522–530, 2014.
- [134] N. Majoul, S. Aouida, and B. Bessaïs, "Progress of porous silicon APTES-functionalization by FTIR investigations," *Appl. Surf. Sci.*, vol. 331, pp. 388–391, 2015.
- [135] M. C. Righetti, M. Gazzano, N. Delpouve, and A. Saiter, "Contribution of the rigid amorphous fraction to physical ageing of semi-crystalline PLLA," *Polymer (Guildf)*, vol. 125, pp. 241–253, 2017.
- [136] D. Bellucci, A. Sola, P. Gentile, G. Ciardelli, and V. Cannillo, "Biomimetic coating on bioactive glass-derived scaffolds mimicking bone tissue," *J. Biomed. Mater. Res. - Part A*, vol. 100 A, no. 12, pp. 3259–3266, 2012.

Annex

Annex A

Table 11. pH and mass values of the samples before and after immersion in SBF.

	Treatment	Replica	SBF pH	Final pH	pH Changes	Initial Mass (g)	Final Mass(g)	Mass Changes (g)		
3 days	Thermal Treatment + Silanization	a	7.42	7.46	0.04	0.3116	0.3118	0.0002		
		b		7.60	0.18	0.3102	0.3102	0		
		c		7.45	0.03	0.3069	0.3068	1E-04		
	Thermal Treatment Crystallization 180 °C 3 + 120°C 45'	a		7.53	0.11	0.3120	0.3101	0.0019		
		b		7.51	0.09	0.3104	0.3094	0.001		
		c		7.60	0.18	0.3069	0.3095	0.0026		
	7 days	Thermal Treatment Crystallization 120°C 60'		a	7.54	7.56	0.14	0.3103	0.3119	0.0016
				b		7.60	0.18	0.3094	0.3112	0.0018
				c		7.54	0.12	0.3095	0.3112	0.0017
		Thermal Treatment + Silanization		a		7.50	0.04	0.3040	0.3123	0.0083
				b		7.57	0.03	0.3081	0.3103	0.0022
				c		7.49	0.05	0.3116	0.3121	0.0005
14 days		Thermal Treatment Crystallization 180 °C 3 + 120°C 45'	a	7.56		7.63	0.09	0.3085	0.3083	0.0002
			b			7.63	0.09	0.3083	0.3082	0.0001
			c			7.65	0.11	0.3087	0.3087	0
		Thermal Treatment Crystallization 120°C 60'	a			7.59	0.05	0.3094	0.3093	1E-04
			b			7.57	0.03	0.3091	0.3093	0.0002
			c			7.63	0.09	0.3072	0.3071	1E-04
	28 days	Thermal Treatment + Silanization	a		7.55	7.55	0.01	0.3129	0.3129	0
			b			7.58	0.02	0.3118	0.3124	0.0006
			c			7.60	0.04	0.3096	0.3100	0.0004
		Thermal Treatment Crystallization 180 °C 3 + 120°C 45'	a			7.62	0.06	0.3094	0.3101	0.0007
			b			7.64	0.08	0.3101	0.3105	0.0004
			c			7.65	0.09	0.3091	0.3094	0.0003
Pristine 316L SS Thermally Treated 316L SS (No Sil)		Thermal Treatment Crystallization 120°C 60'	a	7.55		7.66	0.1	0.3097	0.3107	0.001
			b			7.69	0.13	0.3103	0.3107	0.0004
			c			7.62	0.06	0.3097	0.3099	0.0002
		Pristine 316L SS	a			7.59	0.03	0.3103	0.3094	0.0009
			a			7.6	0.04	0.3121	0.3121	0
			a			7.6	0.05	0.3103	0.3123	0.002
	Thermal Treatment + Silanization	b	7.58		0.03	0.3115	0.3115	0		
		c	7.59		0.04	0.3101	0.3104	0.0003		
		a	7.63		0.08	0.3802	0.3079	0.0723		
Thermal Treatment Crystallization 180 °C 3 + 120°C 45'	b	7.62	0.07	0.3104	0.3105	1E-04				
	c	7.65	0.1	0.3095	0.3094	1E-04				
	a	7.63	0.08	0.3074	0.3071	0.0003				
Thermal Treatment Crystallization 120°C 60'	b	7.69	0.14	0.3091	0.3091	0				
	c	7.64	0.09	0.3109	0.3114	0.0005				